POLYMER BLENDS OF POLY(3-HYDROXYBUTYRATE-CO-3-HYDROXYHEXANOATE) AND EPOXIDIZED NATURAL RUBBER

YOGA SUGAMA SALIM

FACULTY OF SCIENCE
UNIVERSITY OF MALAYA
KUALA LUMPUR

2016

POLYMER BLENDS OF

POLY(3-HYDROXYBUTYRATE-CO-3-HYDROXYHEXANOATE) AND EPOXIDIZED NATURAL RUBBER

YOGA SUGAMA SALIM

**THESIS SUBMITTED IN FULFILMENT OF THE
REQUIREMENTS FOR THE DEGREE OF
DOCTOR OF PHILOSOPHY**

**FACULTY OF SCIENCE
UNIVERSITY OF MALAYA
KUALA LUMPUR**

2016

UNIVERSITI MALAYA

ORIGINAL LITERARY WORK DECLARATION

Name of Candidate: YOGA SUGAMA SALIM

Registration/Matric No: SHC110030

Name of Degree: DOCTOR OF PHILOSOPHY

Title of Project Paper/Research Report/Dissertation/Thesis (“this Work”):

POLYMER BLENDS OF POLY(3-HYDROXYBUTYRATE-CO-3-HYDROXYHEXANOATE) AND EPOXIDIZED NATURAL RUBBER

Field of Study:

I do solemnly and sincerely declare that:

(1) I am the sole author/writer of this Work;
(2) This Work is original;
(3) Any use of any work in which copyright exists was done by way of fair dealing and for permitted purposes and any excerpt or extract from, or reference to or reproduction of any copyright work has been disclosed expressly and sufficiently and the title of the Work and its authorship have been acknowledged in this Work;
(4) I do not have any actual knowledge nor do I ought reasonably to know that the making of this work constitutes an infringement of any copyright work;
(5) I hereby assign all and every rights in the copyright to this Work to the University of Malaya (“UM”), who henceforth shall be owner of the copyright in this Work and that any reproduction or use in any form or by any means whatsoever is prohibited without the written consent of UM having been first had and obtained;
(6) I am fully aware that if in the course of making this Work I have infringed any copyright whether intentionally or otherwise, I may be subject to legal action or any other action as may be determined by UM.

Candidate’s Signature Date 25 JUNE 2016

Subscribed and solemnly declared before,

Date 27 JUNE 2016

ABSTRACT

Poly(3-hydroxybutyrate-*co*-3-hydroxyhexanoate) [P(3HB-*co*-3HHx)] is a biodegradable polyester from the family of polyhydroxyalkanoates. In the first part of this study, the thermal influence on the molecular mass and isothermal crystallization kinetics of P(3HB-*co*-3HHx) were investigated. The molecular mass decreases with increasing isothermal holding temperature and time. Avrami model has been successfully used to describe the isothermal crystallization kinetics of P(3HB-*co*-3HHx). Following the initial outcome, P(3HB-*co*-3HHx) was blended with epoxidized natural rubber (ENR). The blend is expected to yield polymers with combination mechanical or thermal properties. It is shown that ENR promotes the isothermal crystallization rate of P(3HB-*co*-3HHx) despite forming immiscible constituents with P(3HB-*co*-3HHx). The thermal property of P(3HB-*co*-3HHx) is influenced by the presence of ENR after isothermal crystallization. Further experimental result shows that the P(3HB-*co*-3HHx) and ENR can be reacted in-situ using differential scanning calorimeter. The kinetic of melt reaction shows good approximation and similar behavior to that of other melt reaction systems such as poly(3-hydroxybutyrate)/ENR and poly(3-hydroxybutyrate-*co*-3-hydroxyvalerate)/ENR blends.

ABSTRAK

Poli(3-hidroksibutirat-*ko*-3-hidroksiheksanoat) [P(3HB-*co*-3HHx)] merupakan poliester mudah terurai dari keluarga polihidroksialkanoat. Pada bahagian pertama penyelidikan ini, pengaruh termal pada jisim molekul dan isotermal kinetik kristalisasi P(3HB-*ko*-3HHx) telah diselidik. Jisim molekul didapati menurun apabila suhu dan waktu isotermal meningkat. Model Avrami berjaya digunakan untuk menggambarkan isotermal kinetik kristalisasi P(3HB-*ko*-3HHx). Berikutan hasil awal kajian, P(3HB-*ko*-3HHx) telah dicampur dengan getah asli berepoksida (ENR). Campuran ini diharap akan menghasilkan polimer dengan kombinasi ciri-ciri mekanik atau termal. ENR didapati meningkatkan tahap kristalisasi isotermal P(3HB-*ko*-3HHx) walaupun campuran tersebut adalah sistem dua fasa. Sifat termal P(3HB-*ko*-3HHx) dipengaruhi oleh kehadiran ENR setelah kristalisasi isotermal. Kajian terperinci menunjukkan P(3HB-*ko*-3HHx) dan ENR dapat bereaksi secara in-situ dengan menggunakan kalorimetri pengimbas pembezaan. Kinetik reaksi fasa cair menunjukkan anggaran baik dan cir-ciri yang hampir sama dengan sistem reaksi fasa cair yang lain seperti campuran poli(3-hidroksibutirat) / ENR dan poli(3-hidroksibutirat-*ko*-3-hidroksivalerat) / ENR.

ACKNOWLEDGMENTS

A profound sense of honor and gratitude shall first be given (in alphabetical order) to Professor Dr. Gan Seng Neon (acting as Main supervisor in Universiti Malaya/UM, Malaysia), Professor Dr. K. Sudesh Kumar (acting as co-supervisor in Universiti Sains Malaysia/USM, Malaysia), and Associate Professor Dr. Chan Chin Han (acting as co-supervisor in Universiti Teknologi MARA/UiTM, Malaysia) for their caliber supervision, suggestions and great support towards the outcome of this study. Next, a warm thank shall be given to Professor Dr. Hans-Werner Kammer (Universitat Halle, Germany) who has been constantly giving his support to the direction and development of our research group. A part of this work had been successfully completed in Université de Rouen, France under the supervision of Professor Dr. Jean-Marc Saiter. His mind and suggestions had shaped and significantly improved the quality of this work. Also, author would like to acknowledge Mme. M. Bernoit Lefez (Le Groupe de Physique des Matériaux, Université de Rouen, France) for his help in FTIR. All laboratory personnel from USM, UM, UiTM and Université de Rouen are gratefully acknowledged for their technical support, with no exception to Professor Dr. Rauzah Hashim (UM, Malaysia) for the access of POM. Special thank is addressed to my family (Januar Salim, Chang Foong Khian, Dr. Malinda Salim, Dr. Ow Saw Yen, Sumalin Salim), my guardian family (Dr. Koh Yew Ming, Dr. Chan Chin Han, Eugene, Daniel and Dr. Chan's mother) and special friends [(in alphabetical order): Dr. Hanisah Kamilah Abdul Razak, Dr. Oo Chuan Wei, Fatin Harun, R Shanti Rajantharan] for their continual support, dedication, patience and care. Those who were directly or indirectly involved to the accomplishment of this work are also appreciated. Lastly, this work will never be smooth without the financial support from Ministry of Education (Malaysia), Polymer Blends Laboratory (Malaysia), AMME-LECAP (France), and other related research funding. They deserve more than warm applause.

TABLE OF CONTENTS

Page

ORIGINAL LITERARY WORK DECLARATION FORM

ABSTRACT iii

ABSTRAK iv

ACKNOWLEDGMENTS v

TABLE OF CONTENTS vi

LIST OF FIGURES x

LIST OF TABLES xvii

LIST OF SYMBOLS AND ABBREVIATIONS xix

LIST OF APPENDICES xxiii

CHAPTER I – INTRODUCTION 1

1.1 Overview 2

1.2 Aim and Objectives 4

CHAPTER II – LITERATURE REVIEW 6

2.1 PHA 7

  2.1.1 Overview 7

  2.1.2 Thermal properties of PHA 10

  2.1.3 Mechanical properties of PHA 16

2.2 ENR 19

2.3 Polymer blends 22

2.4 Background theories 26

  2.4.1 Glass transition 26

  2.4.2 Crystallinity 26

  2.4.3 Equilibrium melting temperature (T_m^0) 27

2.4.4 Kinetics of isothermal crystallization 29

2.4.5 Temperature dependence of the isothermal crystallization 30

2.4.6 Temperature dependence of the spherulitic growth rates for semi-crystalline polymer 31

2.4.7 Temperature dependence of the rate of thermal degradation 32

2.4.8 Viscosity of dilute P(3HB-*co*-3HHx) solutions 32

CHAPTER III – MATERIALS AND METHODS 35

3.1 Materials 36

3.2 Biosynthesis of PHA 37

3.3 Purification of polymers 38

3.4 Film preparation 38

3.4.1 Neat polymers 38

3.4.2 PHA/ENR blends 39

3.5 Analytical techniques 40

3.5.1 GPC 40

3.5.2 Viscosity measurement of P(3HB-*co*-3HHx) in $CHCl_3$ 40

3.5.3 FTIR 42

3.5.4 Nuclear magnetic resonance (NMR) 42

3.5.5 Thermogravimetry analysis (TGA) 42

3.5.6 DSC 43

3.5.6.1 Thermal stability 43

3.5.6.2 Heat-cool-heat 43

3.5.6.3 Isothermal crystallization and melting behavior 44

3.5.6.4 Reactive blends 45

3.5.7 Polarizing optical microscopy (POM) 45

3.5.8 Dynamic mechanical analysis (DMA) 46

3.5.9 *X*-ray diffraction (XRD) 46

3.5.10 Scanning electron microscope (SEM) 47

CHAPTER IV – RESULTS AND DISCUSSION 48

4.1 P(3HB-*co*-3HHx) 49

4.1.1 Biosynthesis of PHA 49

4.1.2 Structure elucidation (FTIR and NMR) 52

4.1.3 Intrinsic viscosity and viscosity constant 55

4.1.4 Thermal decomposition 57

4.1.4.1 TGA 57

4.1.4.2 Isothermal heat treatment 61

4.1.5 Thermal profile using DSC 74

4.1.5.1 Heat-cool-heat 74

4.1.5.2 Apparent melting temperatures and equilibrium melting temperatures after isothermal crystallization temperature 75

4.1.5.3 Relative crystallinity after isothermal crystallization 80

4.1.6 Kinetics of isothermal crystallization 81

4.1.7 Spherulitic growth rate 90

4.1.8 Temperature dependence of rate of isothermal crystallization 95

4.1.9 Morphology 97

4.2 P(3HB-*co*-8mol% 3HHx)/ENR blends 102

4.2.1 Miscibility 102

4.2.1.1 T_g 102

4.2.1.2 Melting temperature 104

4.2.2 Thermal stability 108

4.2.3 Crystallinity 109

4.2.4 Kinetics of isothermal crystallization and spherulitic growth rate 111

4.2.5 Spherulitic growth rate 113
4.2.6 Activation energy of isothermal crystallization 114
4.2.7 Blend morphology 116
4.2.8 Mechanical properties 122
4.3 Melt reaction between P(3HB-co-8mol% 3HHx) and ENR 125
4.3.1 Glass transition temperature 125
4.3.2 Melt reaction heat 126
4.3.3 Dynamics of reaction 129
4.3.4 Heat-cool-heat 134
4.3.5 Isothermal crystallization and spherulitic growth rate 136
4.3.6 Thermal decomposition 136
4.3.7 FTIR investigation 141
CHAPTER V – CONCLUSIONS & RECOMMENDATION 145
REFERENCES 148

LIST OF PUBLICATIONS AND PAPERS PRESENTED

APPENDIX

LIST OF FIGURES

Figure 2.1	Transmission electron micrograph of PHA granules (left) and the chemical structure of PHA (right) in bacteria cells	7
Figure 2.2	Physical changes of P(3HB), poly(3-hydroxybutyratye-*co*-4-hydroxybutyrate)/P(3HB-*co*-4HB), P(3HB-*co*-3HV-*co*-4HB) films over 8 weeks in soil environment	8
Figure 2.3	Crystallinity as a function of comonomner composition in a series of PHA samples: (a) P(3HB-*co*-3HV), (b) P(3HB-*co*-4HB) and (c) P(3HB-*co*-3HHx)	11
Figure 2.4	Apparent melting temperature as a function of co-monomer composition in a series of PHAs samples: (a) P(3HB-*co*-3HV), (b) P(3HB-*co*-4HB) and (c) P(3HB-*co*-3HHx)	14
Figure 2.5	Mechanism to produce planar zigzag conformation (β-form) in high-strength P(3HB-*co*-3HV) fibers by different drawing methods: (a) one-step-drawing without isothermal crystallization, (b) one-step-drawing after isothermal crystallization, and (c) cold-drawing and two-step-drawing. The vertical arrows indicate the drawing direction.	18
Figure 2.6	NR - From discovery to industrialization	19
Figure 2.7	Milky sap (left) containing poly(*cis*-1,4-isoprene) (right) drips off rubber tree (picture taken from Encyclopedia Britannica)	20
Figure 2.8	Chemical formula of ENR	21
Figure 2.9	Composition-dependence morphologies in immiscible polymer blend (note : particle sizes may vary depending on nature of polymers)	22
Figure 3.1	Ubbelohde suspended viscometer for measuring viscosity of	41

	transparent liquid. The components of this viscometer are: (1) filling tube, (2) venting tube, (3) suction tube, (4) upper filling mark, (5) lower filling mark, (6) solution bulb, (7) suspended level bulb, (8) lower flow bulb, (9) upper flow bulb, (10) lower graduation mark, (11) upper graduation mark.	
Figure 4.1	Phase-contrast micrographs of *C. necator* PHB^{-}4 at (a) 12 h and (b) 72 h (white arrows show bacteria strain containing luminescence PHA granules)	51
Figure 4.2	Plot of [η] and K_H versus 3HHx fraction (x_{HHx}) in the copolymer of P(3HB-*co*-3HHx)	56
Figure 4.3	Coil size against co-monomer content of P(3HB-*co*-3HHx)	56
Figure 4.4	(a) TGA and (b) derivative curves of P(3HB-*co*-3HHx) of different mol% of 3HHx with respect to P(3HB) as a reference	58
Figure 4.5	Expected thermal degradation pathways of P(3HB)	59
Figure 4.6	Plot of ln|deriv. weight| against 1/T for neat P(3HB-*co*-3HHx) [dashed line in P(3HB) sample is for visual aid]	61
Figure 4.7	Reciprocal M_w against t_h for (a) P(3HB-*co*-3mol% 3HHx) at various T_hs, and (b) different molar compositions in P(3HB-*co*-3HHx) at T_h=180 °C	64
Figure 4.8	Rate constant of isothermal degradation of P(3HB-*co*-3HHx) at various T_hs (□: 3 mol% 3HHx, ●: 8 mol% 3HHx, Δ: 12 mol% 3HHx)	66
Figure 4.9	FTIR spectra of neat P(3HB-*co*-8mol% 3HHx) and P(3HB-*co*-8mol% 3HHx) after isothermal heat treatment at T_h = 170 °C, t_h = 30 min (dashed line is for visual aid)	69
Figure 4.10	*X*-ray diffractograms of P(3HB-*co*-8mol% 3HHx) before and after	72

	isothermal degradation (from top to bottom: control or P(3HB-*co*-8mol% 3HHx), and the same polymer after isothermal treatment at 3 min, 10 min, and 30 min). (a) Full spectrum of 2θ from 10° to 40°, and (b) magnified 2θ region from 12° to 19°.	
Figure 4.11	An example of baseline subtraction of P(3HB-*co*-8mol% 3HHx) diffractogram that had been isothermally treated at 170 °C for 3 min	73
Figure 4.12	DSC curve of P(3HB-*co*-8mol% 3HHx) during second heating	75
Figure 4.13	Melting temperature of P(3HB-*co*-3mol% 3HHx) after isothermal crystallization for 5 × $t_{0.5}$ at preselected T_c	76
Figure 4.14	An example of HW plot for P(3HB-*co*-3HHx) [P(3HB) as a reference (H. K. Lee, 2008)]	78
Figure 4.15	Crystallinity of polyhydroxyalkanoates as a function of (a) isothermal crystallization temperature and (b) 3HHx contents [*Note:* X^*_{iso} *in (b) is the average values from (a)*].	80
Figure 4.16	Exothermic crystallization curve of P(3HB-*co*-8mol% 3HHx) for isothermal crystallization at T_c = 111 °C analyzed using horizontal baseline integration	81
Figure 4.17	Fraction of crystallizable component as a function of isothermal crystallization time for P(3HB-*co*-8mol% 3HHx) [T_c = 110 °C (black) to 116 °C (light grey)]	82
Figure 4.18	Half-time of isothermal crystallization as a function of isothermal crystallization temperature (dashed curves represent exponential peak fitting obtained from OriginPro 8.1)	84
Figure 4.19	Avrami plots of P(3HB-*co*-8mol% 3HHx) at isothermal crystallization temperatures (solid curve represents linear peak fitting obtained from OriginPro 8.1)	85

Figure 4.20	Plot of rate constant of isothermal crystallization versus crystallization temperature for P(3HB-*co*-3HHx) (dashed curves represent exponential peak fitting obtained from OriginPro 8.1)	86
Figure 4.21	Micrographs captured after 5 min growing of P(3HB-*co*-8mol% 3HHx) spherulites at T_c = 110 °C at 60 s time interval every micrograph. Magnification 50×	91
Figure 4.22	Radii of growing spherulites of P(3HB-*co*-8mol% 3HHx) isothermally crystallized at T_c 110°C (dotted curve represents linear growth rate fitted using OriginPro 8.1)	92
Figure 4.23	Plot of G as a function of isothermal T_c for P(3HB-*co*-3HHx) with different 3HHx contents (dotted curves represent decreased exponential growth rate fitted using OriginPro 8.1). P(3HB) as a reference polymer (H. K. Lee, 2008).	93
Figure 4.24	Plot of lg($t_{0.5}^{-1}$) *versus* ΔT_c^{-1} of P(3HB-*co*-8mol% 3HHx)	96
Figure 4.25	(a) as prepared and (b) volume-filled spherulites of P(3HB-*co*-3HHx) [(1): 3 mol% 3HHx at T_c = 115 °C, (2): 8 mol% 3HHx at T_c = 118 °C, and (3): 12 mol% 3HHx at T_c = 102 °C]. The micrographs were taken after 120 – 150 min of isothermal crystallization.	100
Figure 4.26	Glass transition temperature of P(3HB-*co*-3HHx)-*blend*-ENR	103
Figure 4.27	Changes in heat capacity of P(3HB-*co*-3HHx)-*blend*-ENR [solid line refers to P(3HB-*co*-8mol% 3HHx) and dashed line refers to ENR]	104
Figure 4.28	Endothermic melting peak of P(3HB-*co*-3HHx) in P(3HB-*co*-3HHx)-*blend*-ENR. From bottom to top: neat P(3HB-*co*-8mol% 3HHx), blends from 10 wt%-90wt%, and ENR.	105

Figure 4.29	Melting profile of P(3HB-*co*-3HHx) in P(3HB-*co*-3HHx)-*blend*-ENR after isothermal crystallization (dashed curve is for visual aid) at T_c = 111 °C	107
Figure 4.30	TGA profile of P(3HB-*co*-8mol% 3HHx)/ENR blends (from top to bottom: w_{ENR} = 0, 0.2, 0.4, 0.6, 0.8, and 1)	108
Figure 4.31	Plot of experimental weight loss fraction of ENR in the blend against nominal weight fraction of ENR	109
Figure 4.32	Average values of crystallinity of P(3HB-*co*-3HHx) in P(3HB-*co*-3HHx)-*blend*-ENR after isothermal crystallization at T_c = 110 – 117 °C	111
Figure 4.33	Plot of $t_{0.5}$ as a function of isothermal T_c for different compositions of P(3HB-*co*-3HHx) in P(3HB-*co*-3HHx)-*blend*-ENR (dashed curves represent exponential peak fitting obtained from OriginPro 8.1)	112
Figure 4.34	Plot of $K^{1/n}$ as a function of (a) isothermal T_c for different compositions of P(3HB-*co*-3HHx)-*blend*-ENR [dashed curves in (a) represent exponential peak fitting obtained from OriginPro 8.1], and (b) ENR weight percent [dashed curves in (b) represent linear peak fitting obtained from OriginPro 8.1]	113
Figure 4.35	Spherulitic growth rate of P(3HB-*co*-3HHx)-*blend*-ENR isothermally crystallized at 116 °C (dashed line is the exponential fitting of the data)	114
Figure 4.36	Activation energy during crystallization of P(3HB-*co*-3HHx) in ENR blends (dashed line is for visual aid)	115
Figure 4.37	Optical micrographs of fully-impinged (a) P(3HB-*co*-8mol% 3HHx) and P(3HB-*co*-8mol% 3HHx)-*blend*-ENR, with ratio of (b)	117

	90/10, (c) 80/20, (d) 70/30, (e) 60/40 and (f) 40/60, isothermally crystallized at T_c = 116 °C for $t_{0.5}$ (magnification 50 ×). Micrographs were taken in between 120 and 150 minutes after isothermal crystallization.	
Figure 4.38	SEM image of neat P(3HB-*co*-3HHx) (or $w_{ENR} = 0$)	118
Figure 4.39	SEM image of P(3HB-*co*-3HHx)-*blend*-ENR containing $w_{ENR} = 0.2$ [Yellow circle indicates large voids in which ENR is rich. White circle could be P(3HB-*co*-3HHx) spherulites. White arrow indicates ENR in inter-spherulitic region of P(3HB-*co*-3HHx)]	119
Figure 4.40	SEM image of P(3HB-*co*-3HHx)-*blend*-ENR containing $w_{ENR} = 0.4$	120
Figure 4.41	Surface morphology of P(3HB-*co*-3HHx)-*blend*-ENR at room temperature (magnification 2.5×)	121
Figure 4.42	Double log plot of (a) elastic and (b) loss moduli of P(3HB-*co*-3HHx)-*blend*-ENR as a function of frequency. ■ - w_{ENR}=0; ○ - w_{ENR}=0.3; ● - w_{ENR}=0.5; ▲- w_{ENR}=0.7; □ - w_{ENR}=1	124
Figure 4.43	(a) Glass transition temperature and (b) its derivative in 50:50 (by weight) P(3HB-*co*-8mol% 3HHx)-*blend*-ENR at different $t_{0.5,rb}$s	126
Figure 4.44	DSC traces when the samples were exposed to T_{rb} = 197 °C until complete melt reaction	127
Figure 4.45	Specific heat of melt reaction as a function of reaction temperature for three blend compositions, w_{ENR} = 0.3, 0.5 and 0.7	128
Figure 4.46	Specific heat of melt reaction versus blend composition at different T_{rb}; ■, 191 °C; ○, 195 °C (dashed curve are for visual aid)	128
Figure 4.47	Reciprocal half time of melt reaction ($t_{0.5,rb}^{-1}$) as a function of weight fraction of ENR for different T_{rb}; ■, 191 °C; □, 194 °C; ●, 197 °C	130

Figure 4.48	Normalized concentration *z* versus time for P(3HB-*co*-3HHx)/ENR 50/50 blends at T_{rb} = 191 °C. The dashed curve is calculated after Eq. (4.8)	132
Figure 4.49	Temperature dependence of parameter *k*′ for P(3HB-*co*-3HHx)-*blend*-ENR of different compositions. w_{ENR} (○) 0.3, (Δ) 0.5, (▲) 0.7	134
Figure 4.50	Crystallization and melting temperatures in 50:50 (by weight) P(3HB-*co*-8mol% 3HHx)-*blend*-ENR at different $t_{0.5,\mathrm{rb}}$ at T_{rb} = 195 °C	135
Figure 4.51	(a) Weight loss as a function of time during the melt reaction of P(3HB-*co*-8mol% 3HHx)-*blend*-ENR containing 10 wt% of ENR at T_{rb} = 195 °C. (b) Changes of mass as a function of ENR weight fraction for different reaction times at T_{rb} = 195 °C. Each marker in (b) represents one experimental run (dashed lines are drawn for visual aid).	138
Figure 4.52	Melt reaction between P(3HB-*co*-3HHx) and ENR (*x* = 92 mol%, *y* = 8 mol%, *a* = 50 mol%, *b* = 50 mol%)	138
Figure 4.53	(a) TGA and (b) its derivative profile of P(3HB-*co*-8mol% 3HHx)-*blend*-ENR after melt reaction (dashed lines are for visual aid)	140
Figure 4.54	Activation energy of P(3HB-*co*-8mol% 3HHx)-*graft*-ENR [(a) P(3HB-*co*-3HHx) and (b) ENR] (straight and dashed lines are for visual aid)	141
Figure 4.55	FTIR spectra of P(3HB-*co*-8mol% 3HHx)-*blend*-ENR at different $t_{0.5,\mathrm{rb}}$ (top: unnormalized spectra; bottom: normalized spectra)	143
Figure 4.56	Normalized intensity peak of P(3HB-*co*-3HHx)-*blend*-ENR as a function of $t_{0.5,\mathrm{rb}}$	144

LIST OF TABLES

Table 1.1	General comparisons between different classes of biodegradable polymers	2
Table 3.1	Characteristics of P(3HB-*co*-3HHx) and ENR samples	36
Table 3.2	Compositions of P(3HB-*co*-8mol% 3HHx)/ENR blends	39
Table 4.1	Biosynthesis of P(3HB-*co*-3HHx)^{a} using different concentrations of CPKO (results presented in CDW, PHA composition and total PHA produced)	50
Table 4.2	Effect of culture volume on the accumulation (CDW and 3HHx content) of P(3HB-*co*-3HHx)§ in *C. necator* PHB^{-}4	51
Table 4.3	Assignment FTIR peaks of P(3HB-*co*-3HHx)	54
Table 4.4	Summary of rate constant of isothermal degradation for P(3HB-*co*-3HHx)s treated at various T_{h}s	67
Table 4.5	Crystallinity indicator of P(3HB-*co*-3HHx) for different thermal treatments	71
Table 4.6	Equilibrium melting point of P(3HB-*co*-3HHx) with different molar fractions of 3HHx	79
Table 4.7	Avrami parameters for the kinetics of crystallization in P(3HB-*co*-3HHx) containing different molar fractions of 3HHx	88
Table 4.8	Quantity *G* for P(3HB-*co*-3HHx) with different mol% of 3HHx	94
Table 4.9	Summary of activation energy during isothermal crystallization of P(3HB-*co*-3HHx)	97
Table 4.10	Equilibrium melting temperature of P(3HB-*co*-3HHx)-*blend*-ENR	107
Table 4.11	Summary of crystallization and melting quantities of P(3HB-*co*-3HHx) in P(3HB-*co*-3HHx)-*blend*-ENR after heat-cool-heat; and T_{g} and ΔC_{p} of the blends	110

Table 4.12	Parameters *k′* and *n* for selected temperatures and blend compositions: *k′* (*n*)	133
Table 4.13	Physical quantities of thermal event in P(3HB-*co*-3HHx) and ENR during melt reaction at T_{rb} = 195 °C	136

LIST OF SYMBOLS AND ABBREVIATIONS

3-hydroxybutyrate	3HB
3-hydroxyhexanoate	3HHx
3-hydroxyvalerate	3HV
4-hydroxybutyrate	4HB
Activation energies	$-E/R$
Activation energy for transport of molecular chains	ΔF^*
Avrami exponent	n
Boltzman constant	k_{B}
Change of specific heat capacity	ΔC_{p}
Coefficient of determination	R^2 or r^2
Cold crystallization temperature	T_{cc}
Concentration	C
Constant that does not depend on temperature	τ
Crude palm kernel oil	CPKO
Crystallinity indicator	*c.i.*
Crystallization enthalpy	ΔH_{cc}
Crystallization temperature	T_{c}
Degree Celcius	°C
Degree of crystallinity / relative crystallinity	X^*
Differential scanning calorimeter	DSC
Dynamic mechanical analysis	DMA
Energy of activation	B^*
Epoxidized natural rubber	ENR
Equilibrium melting temperature	T_{m}^{0}

Fourier transform infrared	FTIR
Fraction of crystallizable component	$X(t)$
Free energy barrier	Δg^*
Free energy of formation of a surface nucleus with critical size	$\Delta\Phi$
Gas chromatography	GC
Gas constant	R
Glass transition temperature	T_g
Gram per litre	$\mathrm{g\ L^{-1}}$
Gram	g
Half-time isothermal crystallization	$t_{0.5}$
Half-time of isothermal melt reaction	$t_{0.5,\mathrm{rb}}$
Holding temperature(s)	T_h
Holding time	t_h
Hour	h
Huggins' constant	K_H
Hydrodynamic volume	V_h
Induction time	t_0
Intrinsic viscosity	η
Isothermal reaction temperature	T_rb
Joule	J
Kilo Dalton	kDa
Kilo Volt	kV
Loss modulus	E''
Mega Hertz	MHz
Melting enthalpy of 100% crystalline reference material	ΔH_ref
Melting enthalpy	ΔH_m

Melting temperature	T_m
Micro	μ
Milli Ampere	mA
Milli litre	mL
Minute	min
Natural rubber	NR
Nuclear magnetic resonance	NMR
Number average molecular weight	M_n
Number-average degrees of polymerization at time 0	$P_{\mathrm{n},0}$
Number-average degrees of polymerization at time t	$P_{\mathrm{n},t}$
Percent	%
Polarizing optical microscopy	POM
Poly(3-hydroxybutyrate)	P(3HB)
Poly(3-hydroxybutyrate-*co*-3-hydroxyhexanoate)	P(3HB-*co*-3HHx)
Poly(3-hydroxybutyrate-*co*-3-hydroxyvalerate)	P(3HB-*co*-3HV)
Poly(3-hydroxybutyrate-*co*-4-hydroxybutyrate)	P(3HB-*co*-4HB)
Polydispersity	D
Polyhydroxyalkanoates	PHA
Pre-exponential constant	G_0
Radial spherulite growth rates	G
Rate constant for generation of reactive product	k'
Rate constant of degradation	k_d
Rate constant of isothermal crystallization	$K^{1/n}$
Relative crystallinity after isothermal crystallization	X_iso
Rounds per minute	rpm
Stability parameter	$1/\gamma$

Storage modulus	E'
Temperature	T
Tetramethylsilane	TMS
Thermogravimetry analysis	TGA
Time	t
Undercooling / supercooling temperature	ΔT_c
Volume per volume	v/v
Weight average molecular weight	M_w
Weight fraction of crystallizable component	w_c
Weight fraction of ENR	w_{ENR}
Weight per weight or weight percent	w/w or wt%
Weight-average molecular weight at time 0	$M_{w,0}$
Weight-average molecular weight at time t	$M_{w,t}$
X-ray diffraction	XRD

LIST OF APPENDICES

Appendix A – NMR of some PHA

Appendix B – FTIR spectra of PHA

Appendix C – Calculation of absolute viscosity (η)

Appendix D – Molecular mass during isothermal holding after DSC analysis

Appendix E – Melting profile of P(3HB-co-3HHx) after isothermal crystallization

Appendix F – Plot of $X(t)$ versus reduced time $\left(\frac{t-t_0}{t_{0.5}}\right)$

Appendix G – Student *t*-test

Appendix H – Radii measurement for growing spherulites of P(3HB-*co*-8mol% 3Hhx) isothermally crystallized at various T_cs

Appendix I – TGA thermograms before and after melt reaction

Appendix J – FTIR after melt reaction

CHAPTER I – INTRODUCTION

1.1 Overview

Much of what we know about the danger of improper disposal of petrochemical-based polymers (Sheavly & Register, 2007), there is a need to use biodegradable and environmentally friendly polymers in daily commodity products. Biodegradable-based polymers can be classified according to their origin (Avérous & Pollet, 2012), such as polymers from agro-resources (e.g. lignin, cellulose, chitin, starch, proteins), from microorganisms [e.g. polyhydroxyalkanoates (PHA)], from biotechnology (e.g. polylactides), and from petrochemical products (e.g. polycaprolactones). Each classification of biopolymers has its advantages and disadvantages over one another summarized in a table below (Table 1):

Table 1.1 General comparisons between different classes of biodegradable polymers

Type of biodegradable polymers	Abundance[1]	Price[2]	Biodegradability
Lignin, cellulose, chitin, starch, etc.	++++	+	+
PHA	++	++++	++++
Polylactides	+++	++	++++
Polycaprolactones	++	+++	++++

[1] production volume/availability

[2] subject to market demand, bulk production and efficiency of recovery

'+' represents frequency of occurrence

The overall production cost of PHA is mainly contributed by the choice of carbon substrates used. It is high compared to the price of other biodegradable polymers, and the yield is relatively low. To overcome these drawbacks, various strategies have been developed. These include: (1) the use of better engineered microorganisms capable of utilizing cheaper carbon sources from industrial wastes, (2) developing an efficient feeding strategies suitable for the growth and accumulation of PHA in the cytoplasm of microorganisms, as well as (3) incorporating another polymers to make polymer blends. For the first time in literature, we report a polymer blend between PHA:poly(3-hydroxybutyrate-*co*-3-hydroxyhexanoate) [P(3HB-*co*-3HHx)] and epoxidized natural rubber (ENR). Unlike other petro-based plastics [e.g. poly(propylene), poly(styrene) etc.] that can be synthesized chemically, production of PHA involves the use of bioreactors and carbon substrates therefore the current price is still not feasible to compete with existing commercial plastics. It is thus sensible to make a polymer blend by incorporating second polymer. Besides, the mechanical properties can be tuned from blend morphologies, properties of parent polymers, phase behavior etc. The second polymers can be any polymers ranging from semi-crystalline to amorphous polymers. In this study, ENR was chosen specifically due to the commercial availability and interesting properties that it possesses. Among the interesting properties aforementioned are good oil resistance and resilience, high elongation at break, high damping properties, low gas permeation, and resistance to organic solvents (Baker, Gelling, & Newell, 1985). Lee and co-workers (2005) reported the melt reaction between homo-polymer poly(3-hydroxybutyrate) [P(3HB)] and ENR-50 ('50' denotes 50mol% epoxidation level) (H. K. Lee, Ismail, Kammer, & Baker, 2005). Both P(3HB) and ENR-50 forms immiscible polymer blends, however after melt reaction, they show a single glass transition temperature (T_g) ranged between the glass transition temperature of P(3HB) and ENR-50 as shown by differential scanning calorimeter (DSC). The influence of longer side chain group of PHA containing 3-hydroxyvalerate (3HV) was also investigated. Chan and co-workers (2004) focused on the thermal properties (Chan & Kammer, 2009) as well as melt reaction (Chan, Ismail, & Kammer, 2004) between poly(3-hydroxybutyrate-*co*-3-hydroxyvalerate) [P(3HB-*co*-3HV)] with 12 mol% of HV content and ENR-50. Both P(3HB)/ENR-50 and P(3HB-*co*-3HV)/ENR-50 form single T_g after melt reaction at preselected reaction (or sometimes called ‘annealing’) temperature. Following these studies, there are several questions in mind of whether the crystallization of P(3HB-*co*-3HHx) in ENR shows similar behavior to that of P(3HB) and P(3HB-*co*-3HV). How does ENR influence the crystallization of P(3HB-*co*-3HHx)? Does the melt reaction between P(3HB-*co*-3HHx) and ENR follow the same kinetics to that of P(3HB)/ENR and P(3HB-*co*-3HV)/ENR blends?

1.2 Aim and Objectives

This research is aimed to understand the thermal behavior of P(3HB-*co*-3HHx) and its blend with ENR-50 (‘50’ denotes the level of epoxidation in mol%). Since the 3-hydroxyhexanoate (3HHx) can range from as low as 3 mol% to approximately 90 mol%, the blend study focuses only at P(3HB-*co*-3HHx) containing 8 mol% of 3HHx. This is established from the following objectives:

1. Production of P(3HB-*co*-3HHx) from *Cupriavidus necator* PHB^{-}4 harboring PHA synthase of *Aeromonas caviae* (pBBREE32d13),
2. Evaluation of the thermal stability of P(3HB-*co*-3HHx) with different mol% of 3HHx,
3. Examination of the kinetics of P(3HB-*co*-3HHx) by isothermal crystallization experiments,
4. Assessment of the influence of ENR-50 to the kinetics of isothermal crystallization of P(3HB-*co*-8mol% 3HHx),
5. Evaluation of the kinetics of melt reaction between P(3HB-*co*-8mol% 3HHx) and ENR-50, and
6. Examination of the thermal behavior (*e.g.* crystallization kinetics, melting behavior, thermal stability) of P(3HB-*co*-8mol% 3HHx)/ENR after melt reaction.

Introduction to this doctorate thesis has been given above. Next, we will discuss the detailed background and research related to PHA and ENR. This chapter elaborates in more detailed notions related to PHA production through microbial production, its recovery processes and relevant past researches. Following this, Chapter 3 summarizes detailed experimental procedures required to achieve our research objectives. Chapter 4 discusses the outcomes of this research. Chapter 5 concludes the findings and elaborates recommendation for future study.

CHAPTER II – LITERATURE REVIEW

2.1 PHA

2.1.1 Overview

PHA, optically active polyesters with (*R*) absolute configuration and chiral centres, can be synthesized by variety of *Gram*-positive and *Gram*-negative bacteria. They serve as energy reserve in the cytoplasmic fluid of bacteria, or as a sink for excess reducing equivalents for microorganisms (Doi & Abe, 1990). The formation of PHA granules and its chemical structure is depicted in Figure 2.1 (Loo, Lee, Tsuge, Doi, & Sudesh, 2005).

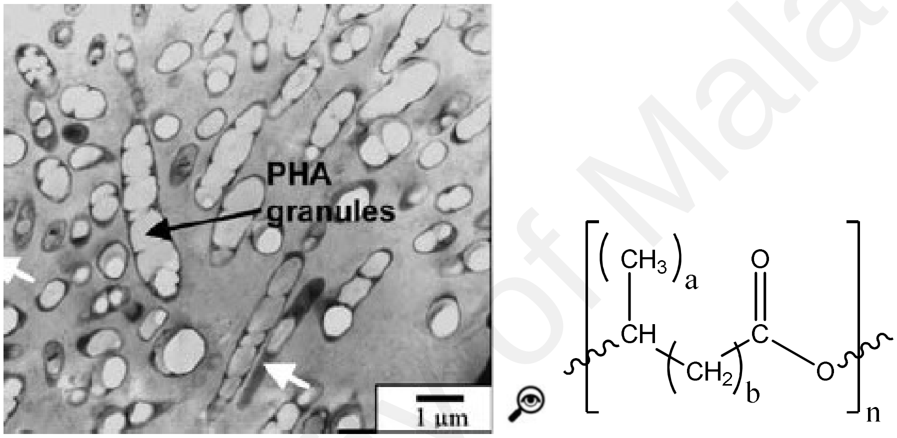

Figure 2.1 Transmission electron micrograph of PHA granules (left) and the chemical structure of PHA (right) in bacteria cells (Loo et al., 2005)

P(3HB) is an example of homo-polymer PHA, which was first isolated by a French microbiologist in 1925 from *Bacillus megaterium* using chloroform extraction (Lemoigne, 1925, 1926). Following the discovery of P(3HB), copolymer containing 3HV (Doi, Tamaki, Kunioka, & Soga, 1988), 4-hydroxybutyrate (Doi, Kunioka, Nakamura, & Soga, 1988) and 3HHx (Doi, Kitamura, & Abe, 1995) have been subsequently discovered. The synthesis of PHA, in general, starts from production of hydroxyacyl-CoAs from carbon substrate and precursors, followed by the polymerization of hydroxyacyl-CoAs by PHA synthases into PHA. To date, there are at least 150 types of PHA monomers successfully identified (Steinbüchel & Valentin, 1995). Depending on the carbon substrates used and biochemical pathways of the microorganisms, the molecular structure and copolymer composition of PHA can be judiciously altered to create polymeric materials with specific physical properties ranging from semi-crystalline plastic to elastic materials, which resemble rubber. PHA are known to exhibit biodegradability (Jendrossek & Handrick, 2002; Jendrossek, Schirmer, & Schlegel, 1996) in soil (Mergaert, Webb, Anderson, Wouters, & Swings, 1993; Sang, Hori, Tanji, & Unno, 2002), sludge (Briese, Jendrossek, & Schlegel, 1994), seawater (Gonda, Jendrossek, & Molitoris, 2000) and tropical mangrove ecosystem (Sridewi, Bhubalan, & Sudesh, 2006). It has been long known that PHA degrading microorganisms tend to attack the amorphous region of PHA leading to a reduction of molecular weight (Shimamura et al., 1994). An example of physical changes in the PHA films is illustrated in Figure 2.2.

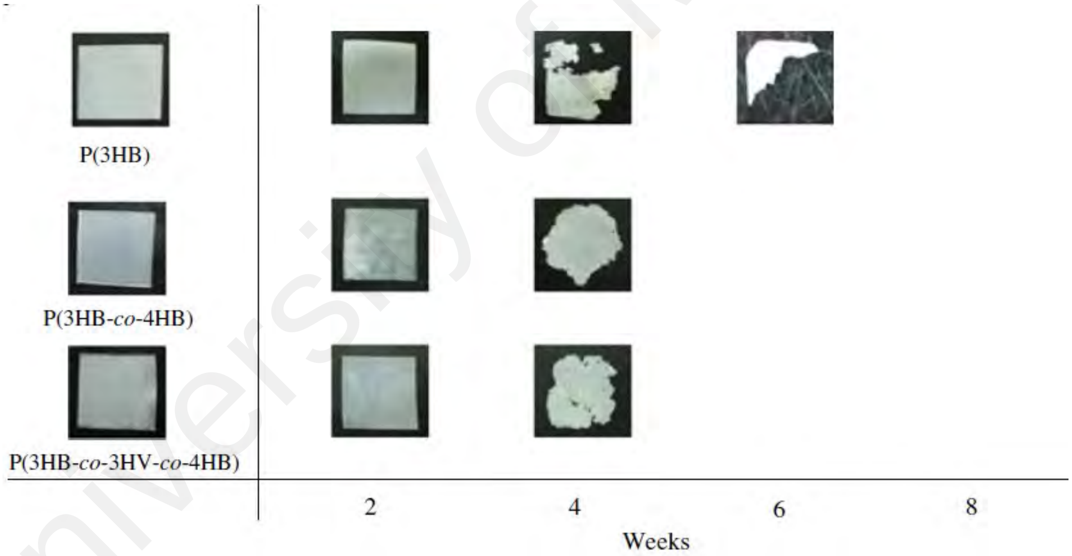

Figure 2.2 Physical changes of P(3HB), poly(3-hydroxybutyratye-*co*-4-hydroxybutyrate)/P(3HB-*co*-4HB), P(3HB-*co*-3HV-*co*-4HB) films over 8 weeks in soil environment (Salim, Sharon, Vigneswari, Mohamad Ibrahim, & Amirul, 2012)

PHA also exhibits biocompatibility to tissue cells: osteoblast (Zhao, Zou, Shi, Wu, & Chen, 2007), fibroblast (Sun, Dai, Zhao, & Chen, 2007), stem cells (You et al., 2011) and can be used for tarsal repair (Zhou et al., 2010); thus, they serve as alternative and environmentally friendly polymeric materials for many applications including environmental and medical applications. Current studies are devoted to the development of better genetically engineered bacteria (I. D. Hay, Du, Burr, & Rehm, 2015; Yokoo, Matsumoto, Ooba, Morimoto, & Taguchi, 2015) producing higher amount of PHA (S. Sato, Maruyama, Fujiki, & Matsumoto, 2015; Vo, Ko, & Ramsay, 2015) from renewable cheaper carbon sources such as fatty acids, sugars or industrial wastes (Fernández-Dacosta, Posada, Kleerebezem, Cuellar, & Ramirez, 2015; Oh et al., 2015; S. Sato et al., 2015). In fact, the choice of chemicals plays a major role to determine the efficiency of recovery process as well as the production cost in industrial scale. Kunasundari and Sudesh (2011) summarized various recovery processes from literatures and discussed the strategies to reduce production cost of PHA in large scale production (Kunasundari & Sudesh, 2011). The challenge of PHA recovery lies within the choice of solvents and chemicals with a certain level of purity, which depends on the types of final application, without compromising the molecular weight of extracted PHA. The biotechnological point-of-view of PHA is not included in this thesis due to the massive load of literatures. This includes genomic modification of bacteria, biosynthesis pathways, feeding strategies during fermentation, and biodegradation.

During storage over a certain period of time, e.g. 1–2 years, PHA undergoes secondary crystallization and the molecular weight of the PHA gradually decreases (de Koning & Lemstra, 1993). From the standpoint of product development, the knowledge of crystallization kinetics is of critical need in regulating the size, orientation/alignment and structure types (banded, fibrillar, shish kebab etc.) of the spherulites of PHA crystals, which in turn, affects the mechanical properties of the materials. The requirement for crystallization of a semi-crystalline polymer is restricted to a temperature range between its T_g and melting temperature (T_m).

2.1.2 Thermal properties of PHA

DSC is a powerful tool to characterize important thermal features of PHA materials such as apparent T_m, enthalpy of melting (ΔH_m), crystallization temperature (T_c) and T_g. In recent years, there have been numerous reports on the determination of crystallinity of PHA using DSC, *X*-ray diffraction (XRD), vibrational spectroscopy particularly on Fourier transform infrared (FTIR) and so on. However, in this chapter, we focus on the determination of crystallinity using DSC. The crystallinity of PHA or any other polymer can be regulated through heating/cooling processes, and these processes affect the final mechanical properties. In a study of isothermal crystallization, the first heating is usually applied to eliminate thermal history to which the polymer is stored. Upon quenched cooling, polymer crystals are formed at preselected isothermal crystallization temperatures. Once the crystallization completes, the polymer is re-heated in order to determine the T_m and ΔH_m. For semi-crystalline polymer processing, the polymer is usually heated and followed by cooling, for examples: injection molding, hot-pressing, extrusion and so on.

P(3HB) has the highest melting point (170–180 °C) in the class of PHA with high degree of crystallinity (X^*) at 55–65% (Barham, Keller, Otun, & Holmes, 1984). X^* is a quantity that depends on the molecular weight, biosynthesis pathway and thermal treatment. Its copolymers such as P(3HB-*co*-3HV), P(3HB-*co*-4HB), and P(3HB-*co*-3HHx) have lower crystallinity, lower melting points, lower crystallization temperatures and wider processing window for processing. Figure 2.3 summarizes the crystallinity of (a) P(3HB-*co*-3HV), (b) P(3HB-*co*-4HB), and (c) P(3HB-*co*-3HHx) in identical thermal conditions unless otherwise stated. Owing to the complexity and lack of studies on the 100% crystallinity materials for PHA copolymers such as P(3HB-*co*-4HB) and P(3HB-*co*-3HHx), all the crystallinity calculations used are based on the 100% crystallinity of

P(3HB) materials (ΔH_{ref} = 146.6 J g^{-1}), as determined by Braham and co-workers (1984). The fundamental issue here is to understand the crystallinity with increasing co-monomer compositions.

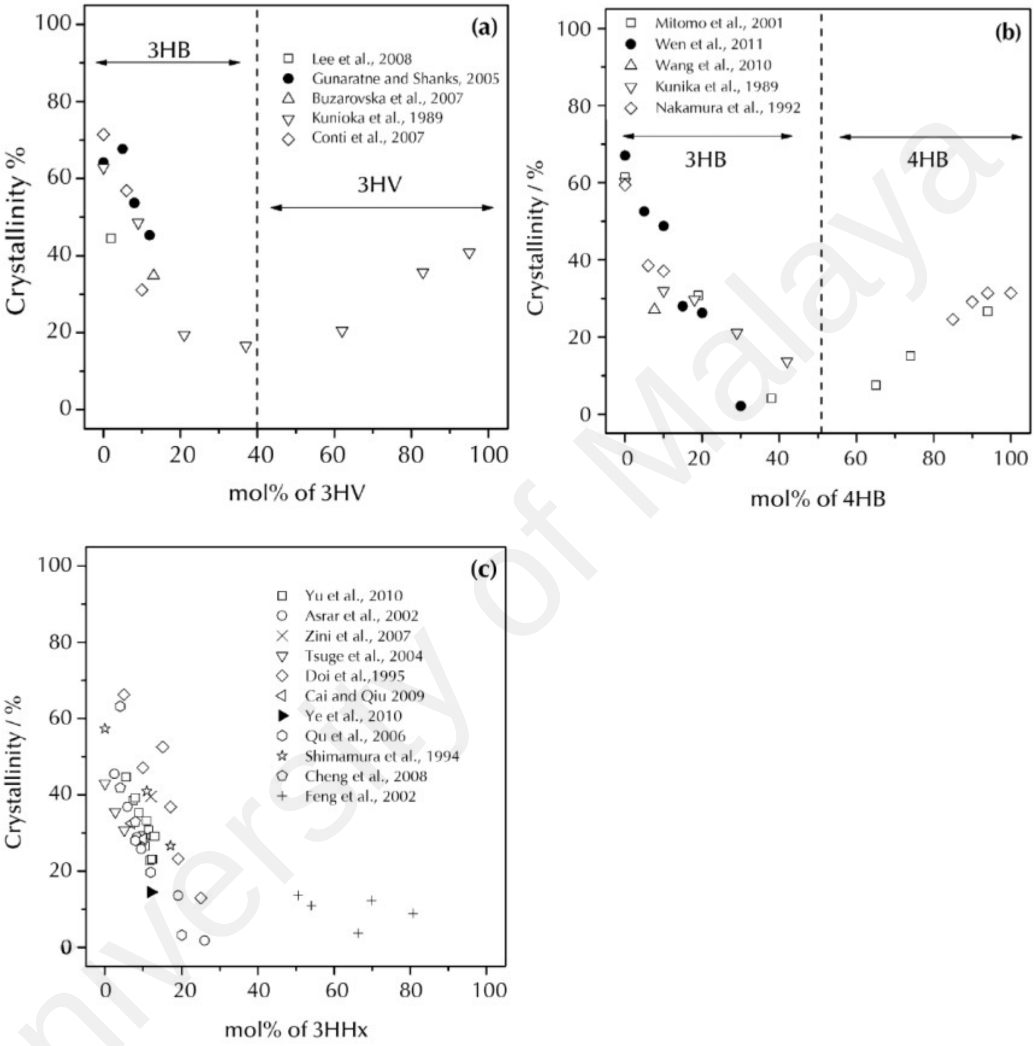

Figure 2.3 Crystallinity as a function of comonomer composition in a series of PHA samples: (a) P(3HB-*co*-3HV) (Buzarovska et al., 2007; Conti, Yoshida, Pezzin, & Coelho, 2007; Gunaratne & Shanks, 2005; Kunioka, Tamaki, & Doi, 1989; W. H. Lee, Loo, Nomura, & Sudesh, 2008), (b) P(3HB-*co*-4HB) (Kunioka et al., 1989; Mitomo, Hsieh, Nishiwaki, Kasuya, & Doi, 2001; Nakamura, Doi, & Scandola, 1992; Wang et al., 2010; Wen, Lu, Peng, Zhu, & Zheng, 2012) and (c) P(3HB-*co*-3HHx) (Asrar et al., 2002; Cai &

Qiu, 2009; Cheng, Lin, Su, Chen, & Sun, 2008; Doi et al., 1995; Feng et al., 2008; Qu, Wu, & Chen, 2006; Shimamura et al., 1994; Tsuge, Saito, Kikkawa, Hiraishi, & Doi, 2004; Ye, Wang, Wang, Chen, & Xu, 2010; Yu et al., 2009; Zini, Focarete, Noda, & Scandola, 2007)

P(3HB-*co*-3HV) can crystallize in either 3-hydroxybuyrate (3HB) or 3HV lattice depending on the compositional distribution. The transformation of 3HB lattice to 3HV lattice is between 40–45 mol% of 3HV as indicated by the dash curve in Figure 2.3(a). Exceeding this composition, the 3HV crystals dominantly prevail due to isodimorphism (Bloembergen, Holden, Hamer, Bluhm, & Marchessault, 1986; Bluhm, Hamer, Marchessault, Fyfe, & Veregin, 1986). The open marker in Figure 2.3 indicates first heating cycle starting from room temperature or lower to above the melting temperature of PHA while the solid marker indicates the second heating after isothermal crystallization at preselected crystallization temperature. There have not been many reports on the crystallinity of PHA with high composition of second monomer determined after isothermal crystallization by using DSC. The crystallinity of P(3HB-*co*-4HB) is illustrated in Figure 2.3(b). Here, it also behaves in similar manner to that of P(3HB-*co*-3HV). The crystallinity reduces drastically to approximately 15% when 40 mol% of 4HB present. The crystallinity of P(3HB-*co*-4HB) increases gradually from 65 to 100 mol% of 4-hydroxybutyrate (4HB). The corresponding polymer crystal in this region is expected to come from the fractions of 4HB. Studies of the crystallinity of P(3HB-*co*-3HHx) show a slightly different trend at high composition of 3HHx. The crystallinity does not increase with increasing monomer up to 100 mol% of 3HHx, as illustrated in Figure 2.3(c) (Asrar et al., 2002; Cai & Qiu, 2009; Cheng et al., 2008; Doi et al., 1995; Feng et al., 2008; Qu et al., 2006; Shimamura et al., 1994; Tsuge et al., 2004; Yu et al., 2009; Zini et al., 2007). This indicates that dominant amorphous longer side chains of 3HHx disrupt the crystalline region of 3HB in the copolymer. The side chain of the random co-monomer units in PHA does affect the crystallinity of the PHA at the same co-monomer composition (mol%) for the isodimorphized co-monomer crystal. For instance, at 80 mol% of second co-monomers in P(3HB-*co*-3HV), P(3HB-*co*-4HB) and P(3HB-*co*-3HHx), a reduction of crystallinity is observed at 30%, 20% and 10%, respectively.

The apparent melting temperature of the corresponding PHA crystals formed during heat-cool-heat process is illustrated in Figure 2.4. Figures 2.4(a), (b), and (c) show the apparent melting temperatures, T_ms, of P(3HB-*co*-3HV) (Buzarovska et al., 2007; Conti et al., 2007; Gunaratne & Shanks, 2005; Kunioka et al., 1989; W. H. Lee et al., 2008; Mitomo, Morishita, & Doi, 1995; Mitomo, Takahashi, Ito, & Saito, 1999; Yamada, Wang, Asakawa, Yoshie, & Inoue, 2001), P(3HB-*co*-4HB) (Kunioka et al., 1989; Lu, Wen, & Yang, 2011; Mitomo et al., 2001; Nakamura et al., 1992; Wang et al., 2010; Wen et al., 2012) and P(3HB-*co*-3HHx) (Asrar et al., 2002; Cai & Qiu, 2009; Doi et al., 1995; Feng et al., 2008; Qu et al., 2006; Shimamura et al., 1994; Tsuge et al., 2004; Yu et al., 2009; Zini et al., 2007) with different co-monomer compositions.

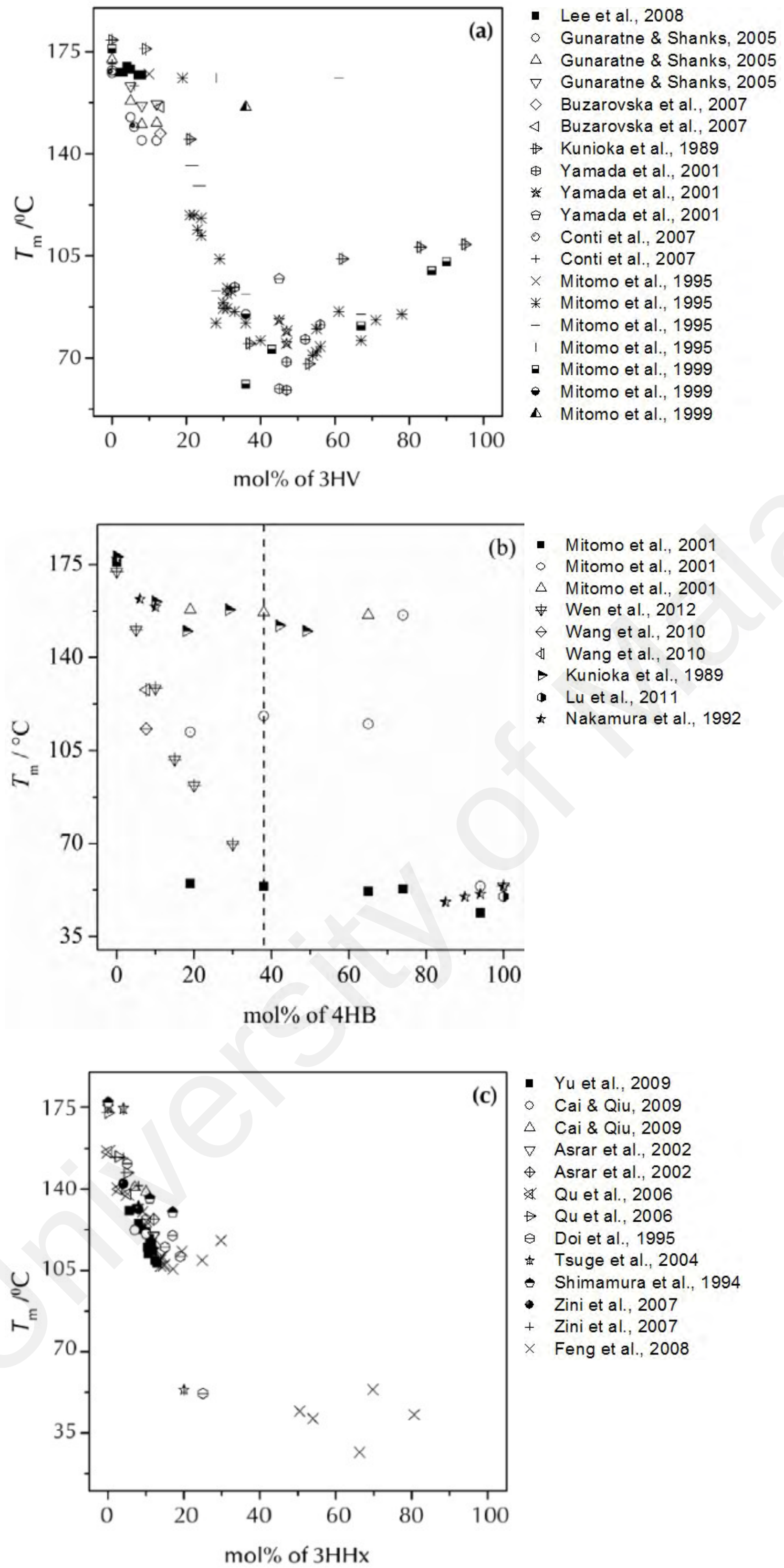

Figure 2.4 Apparent melting temperature as a function of co-monomer composition in the series of PHAs samples: (a) P(3HB-*co*-3HV) (Buzarovska et al., 2007; Conti et al., 2007;

Gunaratne & Shanks, 2005; Kunioka et al., 1989; W. H. Lee et al., 2008; Mitomo et al., 1995; Mitomo et al., 1999; Yamada et al., 2001), (b) P(3HB-*co*-4HB) (Kunioka et al., 1989; Lu et al., 2011; Mitomo et al., 2001; Nakamura et al., 1992; Wang et al., 2010; Wen et al., 2012) and (c) P(3HB-*co*-3HHx) (Asrar et al., 2002; Cai & Qiu, 2009; Doi et al., 1995; Feng et al., 2008; Qu et al., 2006; Shimamura et al., 1994; Tsuge et al., 2004; Yu et al., 2009; Zini et al., 2007)

The melting of P(3HB-*co*-3HV), in Figure 2.4(a), reduces drastically from 175 °C to approximately 70–90 °C up to 40 mol% of 3HV and gradually increases to 100 °C at 100 mol% 3HV. The transition of dominant crystal lattice from 3HB to 3HV indicates that the 3HV units co-crystallized in the sequence of 3HB units and accommodates the repeating monomer unit of 3HB as part of its crystal structure. This phenomenon is an evidence of isodimorphism in P(3HB-*co*-3HV). In the case of P(3HB-*co*-4HB), the T_ms of P(3HB-*co*-4HB) reduce from 175 °C, for P(3HB), to approximately 50 °C at and above 40 mol% of 4HB. The trend of T_ms of P(3HB-*co*-3HHx) also greatly reduces with the increase in 3HHx content. Both P(3HB-*co*-4HB) and P(3HB-*co*-3HHx) have multiple melting peaks. It is evident that there are multiple traces of melting peaks when second co-monomers present, as shown in the example in Figure 2.4(b) with the vertical dash curve for P(3HB-*co*-4HB) with 38 mol% of 4HB at 157, 118 and 54 °C. Multiple melting peaks observed in PHA may result from the presence of crystals with different stability and lamellar thickness (isomorphism and polymorphism), melting-crystallization-remelting mechanism during heating-cooling process, molecular weight differences and/or physical aging (Watanabe, He, Fukuchi, & Inoue, 2001).

2.1.3 Mechanical properties of PHA

Mechanical properties of some PHA are similar to those of conventional polymers such as poly(propylene), poly(ethylene) and poly(styrene). For example, the tensile strength and elongation at break of P(3HB) was reported at 30-45 MPa and 5%, respectively. This tensile strength is similar to that of poly(propylene), which was 38 MPa (Doi & Abe, 1990; Natta & Corradini, 1960). The mechanical properties of PHA are known to be influenced by type of crystals formation. The first study of temperature dependent drawing method that produces ultra-high modulus polymer was studied for poly(ethylene) (Capaccio, Crompton, & Ward, 1976). The drawing of semi-crystalline polymer leads to physically orientation of random coiled amorphous region of the polymer into relatively aligned or stretched form (β-form), and thus great improvement of mechanical strength can be observed. The first experimental observation of planar zigzag or β-form of P(3HB) was made by Yokouchi et al. (1973) (Yokouchi, Chatani, Tadokoro, Teranishi, & Tani, 1973), followed by Orts et al. (1990) (Orts, Marchessault, Bluhm, & Hamer, 1990). Another form of PHA crystal, α-form (2_1 helix with shish-kebab structure), is one of the common structures of PHA crystals and it can be produced from one-step annealing without isothermal crystallization, as illustrated in Figure 2.5(a). The β-form with fully extended PHA chain conformation can be produced using a combination technique of one- or two-step drawing followed by annealing (Furuhashi, Imamura, Jikihara, & Yamane, 2004; Iwata, Fujita, Aoyagi, Doi, & Fujisawa, 2005). The β-form contributes to higher tensile strength because the amorphous region between the lamella is fully extended, as illustrated in Figure 2.5(b) and 2.5(c). There are several factors influencing the tensile strength of semi-crystalline polymer in drawing method, such as the speed of melt-spinning, drawing ratio, applied strain, molecular weight of polymer, crystallization temperature, and annealing condition. In cold one-step drawing, the molten polymer is quenched into ice water and annealed at temperature near to its T_g while in the cold two-step drawing method, the polymer is quenched, annealed, kept at room temperature and further drawing is applied before annealing.

Kusaka and co-workers (1999) shows that the β-form P(3HB) obtained using combination of drawing method has tensile strength at 1.3 GPa (Kusaka, Iwata, & Doi, 1999), while Tanaka and co-workers (2006) reported that P(3HB-*co*-8mol% 3HV) has a tensile strength of 1 GPa (Tanaka et al., 2006). There is a remarkable increment of tensile strength when ultra high molecular weight of P(3HB) is used in the drawing as compared to lower molecular weight. The property of aligned β-form can be retained for several months and no cracks were observed in PHA, suggesting a suppression of secondary crystallization (Fischer, Aoyagi, Enoki, Doi, & Iwata, 2004). In addition to annealing thermal treatment, Martinez-Salazar and co-workers (1989) in their study show that there is a thermal expansion and cracking of P(3HB) and P(3HB-*co*-3HV) after isothermal crystallization (Martinez-Salazar, Sanchez-Cuesta, Barham, & Keller, 1989). The Bragg *d*-spacings of P(3HB-*co*-3HV) having different molar compositions, which are obtained from x-ray diffractometer, show a gradual and linear increment with increasing crystallization temperatures. This implies that when P(3HB) is cooled slowly, larger size of P(3HB) spherulites are formed thus it weakens the mechanical properties of P(3HB).

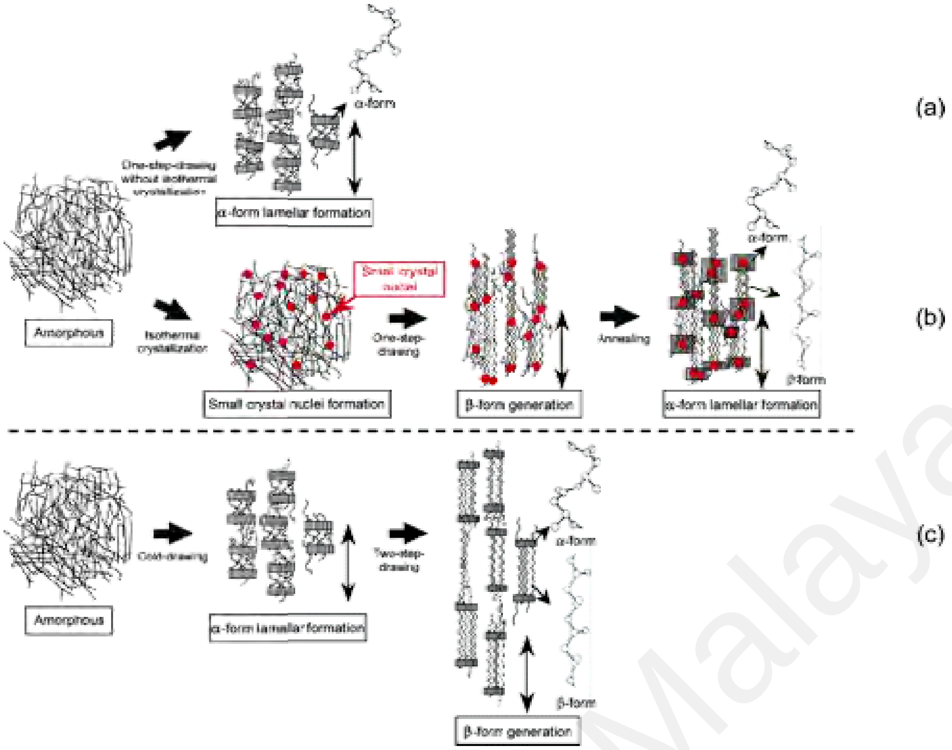

Figure 2.5 Mechanism to produce planar zigzag conformation (β-form) in high-strength P(3HB-*co*-3HV) fibers by different drawing methods: (a) one-step-drawing without isothermal crystallization, (b) one-step-drawing after isothermal crystallization, and (c) cold-drawing and two-step-drawing (Furuhashi et al., 2004; Iwata et al., 2005). The vertical arrows indicate the drawing direction.

2.2 ENR

The discovery of natural rubber (NR) begins in 15th century when Padre d'Anghieria reported that he had seen Mexican tribes people played with elastic balls. It was after a century that Frenando Hernandez reported the same balls can be obtained by tapping a specific bark. The gum that flows out of the bark was called 'holli' by the Indians. The scientific research of NR begins in 1735 when Charles de la Condamine concluded that NR is a type of condensed resinous oil. Since then, there has been more and more successful development of this material in various applications (depicted in Figure 2.6).

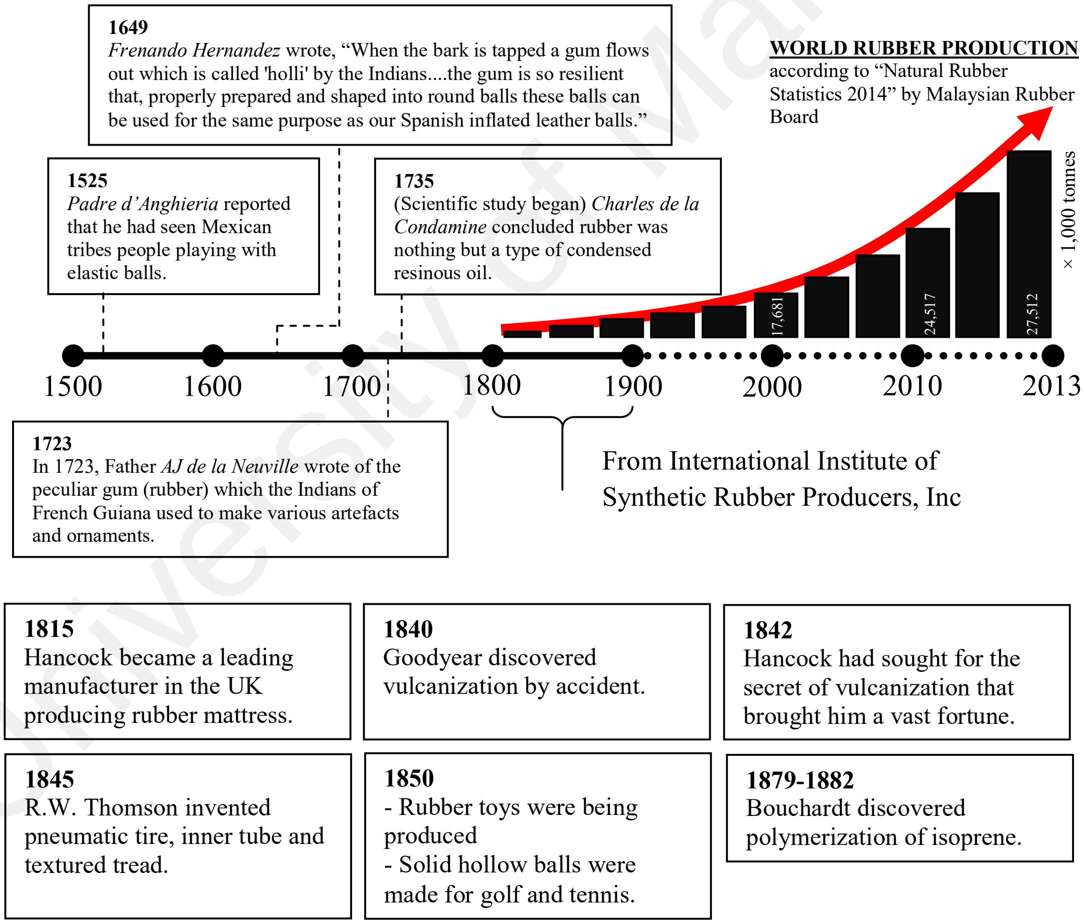

1649
Frenando Hernandez wrote, "When the bark is tapped a gum flows out which is called 'holli' by the Indians....the gum is so resilient that, properly prepared and shaped into round balls these balls can be used for the same purpose as our Spanish inflated leather balls."

1525
Padre d'Anghieria reported that he had seen Mexican tribes people playing with elastic balls.

1735
(Scientific study began) *Charles de la Condamine* concluded rubber was nothing but a type of condensed resinous oil.

1723
In 1723, Father *AJ de la Neuville* wrote of the peculiar gum (rubber) which the Indians of French Guiana used to make various artefacts and ornaments.

WORLD RUBBER PRODUCTION according to "Natural Rubber Statistics 2014" by Malaysian Rubber Board

From International Institute of Synthetic Rubber Producers, Inc

1815
Hancock became a leading manufacturer in the UK producing rubber mattress.

1840
Goodyear discovered vulcanization by accident.

1842
Hancock had sought for the secret of vulcanization that brought him a vast fortune.

1845
R.W. Thomson invented pneumatic tire, inner tube and textured tread.

1850
- Rubber toys were being produced
- Solid hollow balls were made for golf and tennis.

1879-1882
Bouchardt discovered polymerization of isoprene.

Figure 2.6 NR - From discovery to industrialization

In the context of sciences, NR comes from milky sap. The milky sap is obtained by tapping *euphorbiaceae* rubber trees. In the family of *euphorbiaceae*, *hevea brasiliensis* is the most commercially and economically important tree producing up to 28.5 million tonnes of NR around the world (Malaysia, 2014). NR latex consists of mainly poly-*cis*-1,4-isoprene, as shown in Figure 2.7 (<u>note:</u> IUPAC name for isoprene is 2-methyl-1,3-butadiene), with a molecular weight ranging from 100 kDa to 1000 kDa, and small amount of proteins, fatty acids, resins and inorganic compounds. After tapping, NR latex is converted to dry latex. A series of processes has to be performed such as (1) filtration, (2) coagulation with formic acid, (3) mechanical compression, (4) desiccation, and (5) stored until the next stage of processing. Depending on the final products that fit different needs, the dried latex can be further processed and modified into useful products.

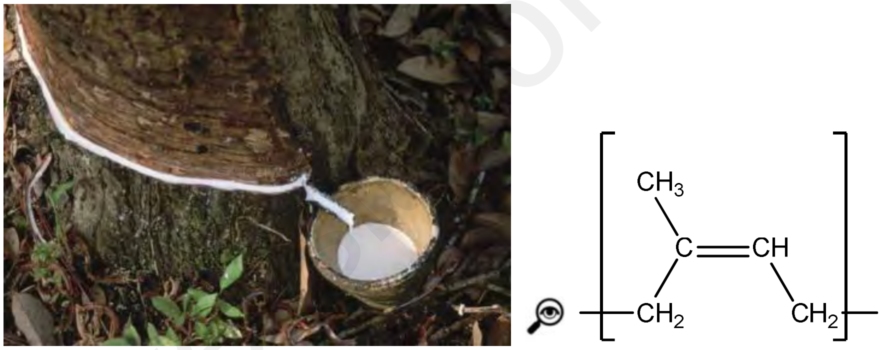

Figure 2.7 Milky sap (left) containing poly(*cis*-1,4-isoprene) (right) drips off rubber tree (picture taken from Encyclopedia Britannica)

Modified NR find its applications in general and industrial rubber goods, footwears, latex products (e.g. glove, condoms, catheters, latex thread), and automotive products (tyres, inner tubes). Without modification, the proteins and chemical compounds in NR latex may cause allergic reactions (Alenius, Turjanmaa, & Palosuo, 2002). One of the common modified NRs is ENR (structural formula is as depicted in Figure 2.8). In the synthesis of ENR, peroxy acid (RCOOOH) is firstly prepared by reacting hydrogen peroxide and carboxylic acid. Following this, epoxidation NR can be performed to produce different ENR containing various degrees of epoxidation. The reactions are shown as following (Gelling, 1991):

Step 1: HOOH + RCOOH ↔ RCOOOH + H_2O

Step 2: "NR" + RCOOOH → "ENR"

ENR is commercially available in two common grades: 25 mol% (also called as ENR-25) and 50 mol% of epoxidation (ENR-50) in Malaysia.

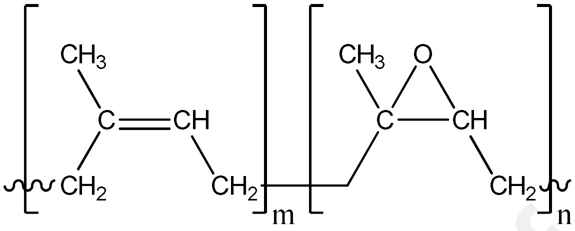

Figure 2.8 Chemical formula of ENR

The chemical (e.g. polarity and stereoregularity) and physical properties (e.g. T_g, resilience, permeability, viscosity) of NR change according to epoxidation level. It is well known that after modification, the polarity and T_g increase while the permeability and oil resistance improve. For DSC analysis, the transition of glassy-rubbery state in ENR occurs at different temperature depending on the level of epoxidation. For example, the T_gs (midpoint) of 25 mol% and 50 mol% ENR are −50 °C and −25 °C, respectively. ENR-50 has a tensile strength of 10 MPa and an elongation at break of 760% (Ishak & Bakar, 1995). The oxirane group of ENR is susceptible to ring opening reactions, and this provides a wide range of possible grafting and/or crosslinking reactions with other polymers.

2.3 Polymer blends

In general, polymer blends are made to prepare a new material and/or overcome the limitation of one or both of the parent materials. The limitation can be in terms of cost or poor physical and thermal performances. To utilize polymer blends, it is always important to study the phase behavior and the miscibility of the blends. We shall limit our subsequent discussion on binary blends. If the two polymers are miscible, which is quite rare in any case, it often produces one single combination of properties. However if the two polymers are immiscible, a modification of one polymer or introduction of compatibilizer agent to improve the interfacial adhesion between the two phases is often needed. The choice of compatibilizer agent influences the final mechanical properties of a blend. There are several possible morphologies of immiscible polymer blends depending on its compositions. They are depicted in the following Figure 2.9.

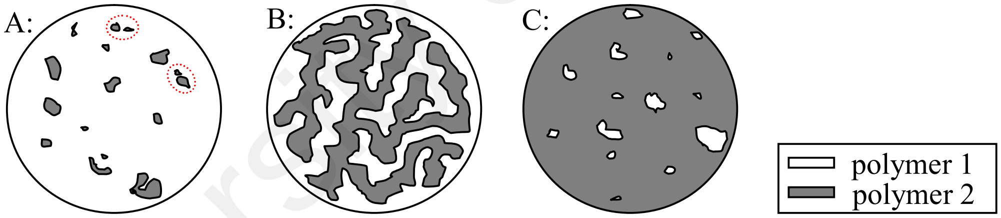

Figure 2.9 Composition-dependence morphologies in immiscible polymer blends (note : particle sizes may vary depending on nature of polymers)

Polymer 2 is randomly dispersed in the matrix of polymer 1 [Figure 2.9 (A)], and vice versa when polymer 1 is randomly dispersed in the matrix of polymer 2 [Figure 2.9 (C)] when one component is in excess. As the amount of polymer 2 increases in Figure 2.9 (A), there is likelihood that it forms agglomerates (indicated by red color square dot circle). Agglomeration can also happen when one polymer is doped with nanoparticles above certain mass fraction, e.g. 10 wt% and above, depending on the blend systems.

When the fraction of polymer 2 increases further, a “co-continuous structure” forms [Figure 2.9 (B)]. Here, a percolation threshold or pathway is formed (roughly 40% - 60% of polymer 2 or 50:50 blend composition in 100% mass fraction). Percolation threshold is defined as the formation of long-range connectivity in random system. This is particularly useful for polymer electrolytes in which the doped ion can ‘hop’ from one to the other end in one phase.

Another simple illustration of Figure 2.9 can usually be observed in semi-crystalline/elastomer blends such as PHA-based and ENR-based polymer blends. Calvão and co-workers (2012) investigated the mechanical properties of P(3HB) blended with ethylene propylene diene monomer (EPDM) and poly(vinyl butyral)-*co*-(vinyl alcohol)-*co*-(vinyl acetate) (PVB). Upon addition of rubber components, e.g. EPDM or PVB, the tensile strength and elastic modulus decrease while the elongation at break and impact strength increase. The crystallinity of P(3HB) phase is not influenced by the presence of EPDM or PVB (Calvão *et al*., 2012). In another related studies, the thermal properties of P(3HB) (H. K. Lee et al., 2005) and P(3HB-*co*-12mol% 3HV) (Chan & Kammer, 2009) blended with ENR-50 reveal that they are immiscible over the entire composition range. The crystallinity is almost constant in the blend. The interfacial adhesion between PHA and ENR can be improved by melt reaction at relatively high temperature or ‘reactive’ blending.

In recent years, there has been a vast amount of research on PHA-based and ENR-based ‘reactive’ polymer blends without adding any compatibilizing agent. For example, ENR/poly(ethylene-*co*-acrylic acid) (Mohanty, Mukunda, & Nando, 1995; Mohanty & Nando, 1996; Mohanty, Roy, Santra, & Nando, 1995), ENR/cassava starch (Nakason, Kaesaman, Wongkul, & Kiatkamjornwong, 2001), ENR/P(3HB) (H. K. Lee et al., 2005), ENR/P(3HB-*co*-3HV) (Chan et al., 2004; Chan & Kammer, 2009), ENR/poly(ε-caprolactone) (Chang, Eom, Kim, Kim, & Kim, 2010), ENR/poly(propylene) (Rooj et al., 2011), P(3HB-*co*-3HV)/poly(butylene succinate) (Praphulla, 2012), and ENR/nylon-12 (Narathichat, Kummerlöwe, Vennemann, Sahakaro, & Nakason, 2012).

In general, there are two ways in which the melt reaction can be performed. The former involves a thermal activation or degradation of one component followed by the reaction at interfacial region between the two components. Thermal induced reaction during melt was successfully performed by Lee et al., 2005 and Chan et al., 2004. Both investigators showed the in-depth kinetics of reaction in which P(3HB) and P(3HB-*co*-3HV) react with ENR-50. By utilizing the thermal degraded products of PHA formed at temperature above T_m, e.g. 180 °C – 234 °C, the carboxylic end groups of PHA react with ENR *via* ring opening polymerization (Chan et al., 2004; H. K. Lee et al., 2005). The thermal properties of melt-reacted P(3HB-*co*-3HV)/ENR blends reveal a single T_g over the entire range of blend compositions after the completion of melt reaction. The aforementioned two T_gs before melt reaction merge during melt reaction in the course of reaction time and they obey Fox equation to a good approximation. The rate of isothermal crystallization of P(3HB-*co*-3HV) after melt reaction decreases significantly.

Narathichat and co-workers (2012) also investigated the melt mixing between different types of NR and nylon-12. They found that ENR/nylon-12 blend exhibit superior mechanical properties as compared to that of air-dried sheet NR/nylon-12 blend. This is attributed to a stronger chemical reaction between the epoxide group of ENR and polar group of nylon-12 in melt mixing (Narathichat et al., 2012).

The latter involves addition of compatibilizing agents or the use of electron accelerator. Addition of compatibilizing agent enhances the surface reaction between one polymer and its adjacent component. For instance, presence of dicumyl peroxide/trimethylpropanetriacrylate enhances the chemical reaction between P(3HB-*co*-3HV) and poly(butylene succinate) (PBS) (Praphulla, 2012). There was an increase in the elongation at break of P(3HB-*co*-3HV)/PBS blend after the addition of dicumyl peroxide/trimethylpropanetriacrylate. When a non-polar polymer such as polypropylene is blended with ENR, a Brabender mixing chamber coupled with an electron accelerator can be used (Rooj et al., 2011). It was shown that the electron induced reactive processing in the presence of triallyl cyanurate yield a significant enhancement to the mechanical properties of final product (23% higher in tensile strength, 400% more elongation and 10% higher in Young's modulus as compared to that of ENR/PP blend without melt reaction).

Introduction of second polymer into a binary polymer blend may change the physical properties (e.g. thermal, mechanical and/or morphological properties). Specific examples on P(3HB)/ENR and P(3HB-*co*-3HV)/ENR have been described above. This leads to the current study of PHA-related blend system such as P(3HB-*co*-3HHx). P(3HB-*co*-3HHx) is known to exhibit higher chain flexibility (elongation at break) due to one extra carbon atom [e.g. P(3HB-*co*-3HV)] on the side chain at the backbone of the polymer chain. The thermal properties of P(3HB-*co*-3HHx) as well as influence of ENR-50 to the isothermal crystallization as well as melt reaction with P(3HB-*co*-8mol% 3HHx) are to be studied in this research.

2.4 Background theories

2.4.1 Glass transition

Glass transition analyzed using DSC can be used to characterize the miscibility of binary polymer blends. Miscibility of a binary blend is characterized by single and compositional dependence T_g. In a miscible system, two T_gs can be seen and it depends on the composition of the blend or in some cases, single and compositional dependence T_g can be observed as well. In immiscible however, two T_gs do not change with blend compositions. A common model to characterize miscibility is Fox equation (Fox & Flory, 1950), which is given by

$$\frac{1}{T_{\mathrm{g}}} = \frac{w_1}{T_{\mathrm{g1}}} + \frac{w_2}{T_{\mathrm{g2}}} \tag{2.1}$$

where, T_g is the glass transition of miscible system, w_1 and w_2 are the mass fraction of polymer 1 and polymer 2, respectively, T_{g1} and T_{g2} are the glass transition temperature of pure components (in Kelvin).

2.4.2 Crystallinity

To determine the crystallinity of PHA, melting enthalpy of a 100% crystalline PHA is often used as a reference value. The ratio of melting enthalpy corresponds to the crystalline lamellae, which is obtained from first or second heating process, and melting enthalpy of 100% crystalline material yields X^* [Eq. (2.2)].

$$X^* = \frac{\left(\Delta H_{\mathrm{m}} - \Delta H_{\mathrm{cc}}\right)}{w_{\mathrm{c}} \times \Delta H_{\mathrm{ref}}} \times 100\% \tag{2.2}$$

where, X^* refers to the crystallinity, ΔH_{cc} is the crystallization enthalpy during second heating (in J g^{-1}) and w_c is the weight fraction of crystallizable component.

The crystallinity of PHA after isothermal crystallization (X) at preselected crystallization temperature for 5 half times of the crystallization time is calculated from Eq. (2.3)

$$X_{\mathrm{iso}}^{*} = \frac{\Delta H_{\mathrm{m}}}{w_{\mathrm{c}} \times \Delta H_{\mathrm{ref}}} \times 100\% \tag{2.3}$$

where X^{*}_{iso} is the crystallinity after isothermal crystallization.

Eq. (2.2) is used in heat-cool-heat experiment (c.f. refer to heat-cool-heat procedure in Section 3.5.6.2), while Eq. (2.3) is used in isothermal experiment (c.f. refer to isothermal procedure in Section 3.5.6.3). In the heat-cool-heat experiment, P(3HB-*co*-3HHx) was heated to melt (heating cycle 1) and cooled down below glass transition temperature (cooling cycle 1), followed by re-heating (heating cycle 2) to temperature above its melting point. Depending on applied cooling rate, P(3HB-*co*-3HHx) may undergo crystallization during heating cycle 2. If the cooling rate is fast enough, the polymer melt cannot undergo crystallization, and polymer crystals were not developed during cooling. Upon heating, the amorphous polymer reorganizes itself and cold crystallization peak appears. Thus, the term ΔH_{cc} shall be added into the equation in order to determine the crystallinity of the polymer. In Eq. (2.3) however, the polymer crystals were developed during isothermal crystallization thus there was theoretically no crystal growth during cooling and re-heating and $\Delta H_{\mathrm{cc}} = 0$ J g^{-1}. By inserting ΔH_{cc} value (= 0 J g^{-1}) into Eq. (2.2), Eq. (2.3) can be obtained.

2.4.3 Equilibrium melting temperature (T_{m}^{0})

The T_{m}^{0} of a semi-crystalline polymer is defined as the melting temperature of most stable or perfect crystal. It can be determined by a step-wise annealing procedure as proposed by Hoffman and Weeks in 1962 (Hoffman & Weeks, 1962). When a semi-crystalline polymer with long chain molecules such as PHA is crystallized near to its T_{m}^{0}, the crystallization rate is so slow that it is not practical to study the kinetics of isothermal crystallization and the subsequent corresponding apparent melting temperature. Hence, the semi-crystalline polymer is crystallized at temperature far away from T_{m}^{0} and the corresponding apparent T_m can be determined. Extrapolation of linear function of the results of T_m *vs* T_c to $T_m = T_c$ yields T_m^0. The data points of T_m *vs* T_c of PHA shall be sufficient (*e.g.* 7–8 points) in order to obtain reliable extrapolated T_m^0s by means of Eq. (2.4) (Hoffman & Weeks, 1962).

$$T_m = \frac{1}{\gamma} T_c + \left(1 - \frac{1}{\gamma}\right) T_m^0 \tag{2.4}$$

where, $1/\gamma$ is related to entropy change in the amorphous phase caused by crystallization from the point of view of thermodynamics.

In polymer blends, T_m^0 can be used to evaluate the polymer-polymer interaction (χ) and miscibility between semi-crystalline and amorphous polymers (Nishi & Wang, 1975). As also pointed out by Mandelkern (2004), T_m^0 depression is a colligative property and it is by necessity very small for polymers with high molecular mass. This depression of T_m^0 is observed only if χ value is negative. This means that the magnitude of thermodynamic χ and amount of T_m^0 depression is dependent on the strength of interaction between two polymers. The depression of T_m^0 in binary blends comprising of one crystallizable component can be expressed as

$$\frac{1}{T_m} - \frac{1}{T_m^{\ 0}} = -\left(\frac{R}{\Delta H_u} \frac{V_{2u}}{V_{1u}}\right)\left[\frac{\ln v_2}{x_2} + \left(\frac{1}{x_2} - \frac{1}{x_1}\right)(1 - v_2) + \chi(1 - v)^2 + \Delta\overline{G}_H\right] \tag{2.5}$$

where, ΔG_H is a composition dependent terms that represents the hydrogen bonding mixing interaction, R is a gas constant, V_{1u} and V_{1u} is the molar volume of a repeating unit of the polymer species 1 (crystallizable) and 2 (non-crystallizable), respectively, x_1 and x_2 is the number of segments, χ represents non-polar interaction.

2.4.4 Kinetics of isothermal crystallization

The crystallization of polymer in bulk as well as in solution is initiated by nucleation followed by growing of spherulites (Mandelkern, 2002). A common fundamental approach to study isothermal crystallization kinetics is the heuristic Avrami phase transition theory (Avrami, 1939, 1940, 1941).

The Avrami model was originally derived for the study of kinetics of crystallization and growth of a simple metal system, and further extended to the crystallization of polymer. Avrami assumes the nuclei develop upon cooling of polymer and the number of spherical crystals increases linearly with time at a constant growth rate in free volume. The Avrami equation is given as

$$X(t) = 1 - \exp\left[-K^{1/n}\left(t - t_0\right)\right]^n \tag{2.6}$$

where, $X(t)$ is relative crystallinity after Avrami at time t; t_0 is an induction time; $K^{1/n}$ is an overall rate constant of isothermal crystallization (min^{-1}); and n is Avrami exponent. Induction time is defined as the initial time in which the polymer crystals start to grow. Selection of induction time for Avrami fitting is important to achieve reasonable value of $K^{1/n}$ and n (Lorenzo, Arnal, Albuerne, & Müller, 2007). The Avrami exponent depends not only the structure of nuclei/crystal but also on the nature of the nucleation (Avrami, 1940).

Rearrangement of Eq. (2.6) arrives at Eq. (2.7), and the calculation of estimated half-time isothermal crystallization ($t_{0.5}$) from Avrami plot is shown in Eq. (2.8).

$$\lg\left[-\ln\left(1 - X\right)\right] = \lg K^{1/n} + n\lg\left(t - t_0\right) \tag{2.7}$$

$$t_{0.5} = \frac{(\ln 2)^{1/n}}{K^{1/n}} \tag{2.8}$$

$K^{1/n}$ and n can be extracted from the intercept and the slope of Avrami plot, $lg[-ln(1-X)]$ *versus* $lg(t-t_0)$, respectively. The prime requirement of Avrami model is the ability of spherulites of a polymer to grow in a free space. Besides, Avrami equation is usually only valid at low degree of conversion, where impingement of polymer spherulites is yet to take place. The rate of crystallization of polymer can also be characterized by reciprocal half-time of isothermal crystallization $(t_{0.5})^{-1}$. The use of Avrami model permits the understanding on the kinetics of isothermal crystallization as well as non-isothermal crystallization. However, in this chapter the discussion of the kinetics of crystallization is limited to isothermal conditions.

2.4.5 Temperature dependence of the isothermal crystallization

The activation energy of rate of isothermal crystallization PHA is calculated using Hoffman-Arrhenius' approach (Hoffman, 1982). The Hoffman's Arrhenius-like model is described as

$$\frac{1}{t_{0.5}} = \frac{1}{\tau}\exp\left[-\frac{\Delta g^*}{k_\mathrm{B}T_\mathrm{c}}\right] \tag{2.9}$$

and

$$\Delta g^* = L\alpha\beta\frac{\sigma^2 T_\mathrm{m}^0}{\Delta H_\mathrm{m}\rho\Delta T_\mathrm{c}} \tag{2.10}$$

where, Δg^* is the free energy barrier that must be overcome before a new stable PHA crystal can develop. ΔT_c is the undercooling $(T_\mathrm{m}^0-T_\mathrm{c})$. All the abbreviations of temperature independent quantities are given by B, and τ is a constant that does not depend on temperature. It is thus convenient to define the reciprocal half-time of isothermal crystallization $(t_{0.5}^{-1})$, as

$$\frac{1}{t_{0.5}} = \frac{1}{\tau}\exp\left[-\frac{B}{\Delta T_\mathrm{c}}\right] \tag{2.11}$$

When $\frac{\Delta T_c}{T_m^0}$ is constant or approximately constant, the activation energy, B^*, can be rewritten as

$$B^* \equiv \frac{B}{\left(1 - \frac{\Delta T_c}{T_m{}^0}\right)} \tag{2.12}$$

By multiplying the B^* energy of activation with gas constant, R, one can obtain the activation energy in the unit of J mol^{-1} or kJ mol^{-1}.

2.4.6 Temperature dependence of the spherulitic growth rates for semi-crystalline polymer

The temperature dependence of the radial spherulite growth rates (G) in semi-crystalline polymer can be analyzed using Lauritzen-Hoffman approach, which was developed in 1973 and 1976 (Hoffman, Davis, & Lauritzen, 1976; Lauritzen & Hoffman, 1973). G is dependent on crystallization temperature, expressed as

$$G = G_0 \, exp\left(-\frac{\Delta F^*}{\Delta T_c}\right) \tag{2.13}$$

G_0 is a pre-exponential constant assumed to be constant or proportional to T_c, ΔF^* is the activation energy responsible for the transport of molecular chains across liquid-solid interface and the free energy of formation of a surface nucleus with critical size. The quantity G is influenced by the type, molecular weight, composition, etc. of the semi-crystalline polymer.

2.4.7 Temperature dependence of the rate of thermal degradation

The temperature dependence of rate of thermal decomposition after thermogravimetry analysis was described using Hoffman's Arrhenius-like relationship. This can be calculated from the slope of natural logarithmic of absolute derivative weight (*ln*|deriv. weight|) versus reciprocal temperature (1/*T*). The rate constant during thermal decomposition is generally given by Arrhenius equation:

$$k = Ae^{-\frac{E}{RT}} \tag{2.14}$$

where A and E are the material properties, R is a gas constant, T is the absolute temperature. A is a measure of probability the molecule having energy E will participate in a reaction while E is the activation energy (energy barrier against opposing the reaction). The fundamental rate equation can be described as $\frac{\mathrm{d}\alpha}{\mathrm{d}T} = k \times f(\alpha)$, where $f(\alpha)$ is a reaction model. Since we are comparing the reaction within the same PHA family having different type of monomers units, $f(\alpha)$ is assumed to be constant. Thus, Arrhenius equation can be rearranged to

$$ln\left|\frac{\mathrm{d}\alpha}{\mathrm{d}T}\right| = (lnA) - \left(\frac{E}{R}\right)\frac{1}{T} \tag{2.15}$$

where, α is a fraction of decomposition (weight %), T is temperature, A is constant, E is activation energy during initial thermal decomposition and R is gas constant [8.314 J (mol K)$^{-1}$].

2.4.8 Viscosity of dilute P(3HB-*co*-3HHx) solutions

Viscosity is a fundamental property of polymer solutions. It is a measure of resistance against flow, and is a function of both temperature and pressure. The calculation of viscosity can be performed using Ubbelohde viscometer, which is based on Poiseuille's equation. Consider an incompressible fluid that flows through a tube with radius R and length l, with pressure P_1 at one end and a pressure at another P_2 (Figure 2.10).

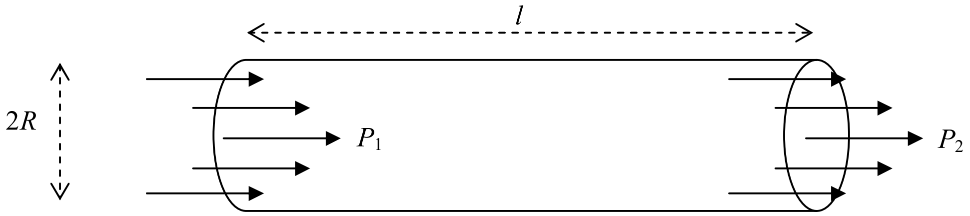

Figure 2.10 Measurement of viscosity when liquid flows through from a capillary tube with P_1 pressure to P_2

We have from above Poiseuille's equation:

$$Q = \frac{\pi \Delta P a^4}{8\eta l} \tag{2.16}$$

where Q is flow rate (cm^3 s^{-1}), P is hydrostatic pressure (dyn cm^{-2}), a is radius of capillary (cm), and l is the length of capillary. This equation is used in the calculation of viscosity by using capillary viscometer. It is expressed by measuring the time required for a defined liquid to flow through a capillary tube because of the hydrostatic pressure of the liquid column itself. The pressure difference in term of hydrostatic pressure is given by:

$$\Delta P = \rho g h \tag{2.17}$$

where ΔP is pressure difference between two ends of the liquids with h, ρ is density of the liquid, g is acceleration of gravity, and h is the height of the liquid.

Expression of the viscosity (η) can be obtained by combining Eq (2.16) and (2.17)

$$\eta = \frac{\pi g h a^4}{8 l V} \rho t \tag{2.18}$$

where t is the efflux time to flow between two graduation marks in viscometer, V is volume of liquid dispensed during experiment. For particular viscometer, Eq (2.18) can be rewritten as

$$\eta = K \rho t \tag{2.19}$$

where K is a constant for a given viscometer. Eq. (2.19) can be used to obtain kinetic viscosity, which is given as $v = Kt$ and $v = \eta/\rho$.

The relative viscosity is the ratio of the increment in the solution viscosity (η) with respect to that of the pure solvent, η_0.

$$\eta_{\mathrm{rel}} = \frac{\eta}{\eta_0} \tag{2.20}$$

The specific viscosity of a polymer solution with C concentration is

$$\eta_{\mathrm{spec}} = \frac{\eta - \eta_0}{\eta_0} = \eta_{\mathrm{rel}} - 1 \tag{2.21}$$

and the intrinsic viscosity is defined as

$$[\eta] = \lim_{C \to 0} \frac{\eta_{\mathrm{spec}}}{C} \equiv \lim_{C \to 0} C^{-1}\, ln\, \eta_{\mathrm{rel}} \tag{2.22}$$

Based on Eq. (2.22), the intrinsic viscosity can be obtained by determination of viscosities of polymer solutions in various concentrations. The viscosities are obtained by measuring the efflux time of the solutions to flow between two points in the Ubbelohde viscometer. Then, it is followed by extrapolation of η_{spec}/C to zero concentration. In a range of moderate concentration, the dependence is linear and can be written as the Huggins' equation:

$$\eta_{\mathrm{spec}} / C = [\eta] + k_{\mathrm{H}} [\eta]^2 C \tag{2.23}$$

where k_{H} is the (dimensionless) Huggins' constant. Thus $[\eta]$ can be obtained as the intercept in a linear least-squares fit.

CHAPTER III – MATERIALS AND METHODS

3.1 Materials

Copolymers P(3HB-*co*-3HHx) containing 3 mol% of 3HHx content was synthesized in Ecobiomaterial Research Laboratory, School of Biological Sciences, Universiti Sains Malaysia, Penang, Malaysia. Other copolymers of P(3HB-*co*-3HHx) containing 8 mol% and 12 mol% of 3HHx were kindly provided by Kaneka Corporation, Osaka, Japan. ENR (50% epoxidation level) is commercial product from Malaysia Rubber Board, Sg. Buloh, Malaysia. Analytical reagents EMSURE® chloroform and methanol were obtained from Merck KGaA, Darmstadt, Germany. Characteristics of the polymers used in this study are given in Table 3.1.

Table 3.1 Characteristics of P(3HB-*co*-3HHx) and ENR samples

Polymer	P(3HB-*co*-3HHx)			ENR
	3 mol% 3HHx	8 mol% 3HHx	12 mol% 3HHx	50 mol% epoxidation
$M_w \times 10^5$ (g mol^{-1})^a	7.4	5.9	7.6	10.1
$M_n \times 10^5$ (g mol^{-1})^a	4.0	3.0	4.0	3.0
M_w/M_n ^{a}	1.8	1.9	1.9	3.5

[a] Molecular masses as estimated in this work by gel permeation chromatography (GPC) (detailed procedure is shown in Section 3.5.1)

M_w = weight average molecular weight

M_n = number average molecular weight

3.2 Biosynthesis of PHA

Biosynthesis of P(3HB-*co*-3mol% 3HHx) was carried out using *C. necator* PHB^{-}4 transformant harboring the PHA synthase enzyme of *Aeromonas caviae* (Fukui & Doi, 1998) in shake-flask method. The bacterium was first grown for 5 h at 30 °C under aerobic conditions (agitation at 200 rpm) on a *dual action shaker SK-71* in 250 mL conical flasks containing 50 mL of a nutrient-rich medium containing 1.0 g of meat extract, 1.0 g of peptone, and 0.2 g of yeast extract in distilled water. Once the optical density reaches 4.5 – 5 (analyzed using *HITACHI U-1900* spectrophotometer at a wavelength of K_{270}), 3% *v/v* of the grown cell was transferred to 250 mL mineral salt medium containing 2.8 g of KH_2PO_4, 3.32 g of Na_2HPO_4, 0.25 g of $MgSO_4 \cdot 7H_2O$ and 1 mL of trace element solution per liter of distilled water. The micro-trace element solution contained the following (per liter of 0.5 N HCl): 20 g of $FeCl_3 \cdot 6H_2O$, 10 g of $CaCl_2 \cdot H_2O$, 0.03 g of $CuSO_4 \cdot 5H_2O$, 0.05 g of $MnCl_2 \cdot 4H_2O$, and 0.1 g of $ZnSO_4 \cdot 7H_2O$. All the formulations aforementioned are according to Doi and co-workers (Doi et al., 1995). The initial pH of mineral salt medium was adjusted to 7 by adding sodium hydroxide and/or hydrochloric acid. A certain amount of crude palm kernel oil (CPKO) ranging from 5.0 to 17.5 g L^{-1} and 50 μg mL^{-1} of kanamycin was added into the mineral medium and was allowed to incubate for 72 h at 30 °C (agitation at 200 rpm) prior to harvesting. The cultivated cells after 72 h were harvested by centrifugation (*Kubota 6500* refrigerated centrifuge, Japan) at check 8000 rpm, washed with distilled water and lyophilized (freeze-drying).

To determine the PHA content and monomer composition, lyophilized cells were subjected to methanolysis in the presence of 15% (v/v) sulphuric acid and 85% (v/v) methanol, before the analysis using chromatography (Braunegg, Sonnleitner, & Lafferty, 1978). The heating was performed in a *Techne Dr-block® DB-3A* heater (Bibby Scientific

Limited, UK) for 140 min at 100 °C. The mixture was added with 1 mL deionized H_2O upon cooling and homogenized by vortex mixing. Two layers were formed and the organic layer (0.5 mL) containing hydroxyacyl methyl ester PHA was separated into a new vial containing sodium sulfate prior to gas chromatography (GC) (*Shimadzu GC-2010*). It was shown that the P(3HB-*co*-3mol% 3HHx) produced from the biosynthesis contained 3 mol% of 3HHx.

3.3 Purification of polymers

All polymers, P(3HB-*co*-3HHx) with different 3HHx contents and ENR, were purified prior to analyses and polymer blending. In the purification step, 4% (w/w) polymer was dissolved in chloroform for 24 h. The polymer solution was concentrated in an *Eyela® N-1110SW-D* rotary evaporator (Japan) at 45 °C under vacuo, and further precipitated in ice-cold methanol under constant agitation. White precipitate was separated and left to dry at room temperature before further drying in a convection oven at 50 °C for 24 h and vacuum oven at the same parameter.

3.4 Film preparation

3.4.1 Neat polymers

Neat PHA thin films were prepared by solution casting technique. A mass of 1 g polymer [P(3HB-*co*-3mol% 3HHx), P(3HB-*co*-8mol% 3HHx), P(3HB-*co*-12mol% 3HHx), ENR] was dissolved in 10 mL chloroform and poured into Teflon dish. The polymer solution was mixed homogenously at 50 °C for 24 h – 48 h. After dissolution, the mixture was casted onto Teflon dish and was allowed to evaporate slowly through aluminum foil (with little pin-head sized holes). Once the film dried, it was kept in convection oven at 50 °C for 24 h and further dried in vacuo for another 24 h to ensure removal of residual solvent.

3.4.2 PHA/ENR blends

P(3HB-*co*-8mol% 3HHx)/ENR blends [also called as P(3HB-*co*-8mol% 3HHx)-*blend*-ENR] was prepared by solution casting technique. The composition of the blends ranged from (*w/w*) 100/0 to 0/100, with increment of 10 wt% step (Table 3.2). A total amount of 1 g polymer was dissolved in 10 mL AR-grade chloroform and poured into Teflon dish. The Teflon dish containing mixture solution was covered with aluminum foil (with little pin-head sized holes), and was allowed to evaporate at room temperature. The process of drying blend films was as described in Section 3.4.1.

Table 3.2 Compositions of P(3HB-*co*-8mol% 3HHx)/ENR blends

P(3HB-*co*-8mol% 3HHx)/ENR (w/w)	Weight of P(3HB-*co*-8mol% 3HHx) (g)	Weight of ENR (g)
100/0	1.0	0.0
90/10	0.9	0.1
80/20	0.8	0.2
70/30	0.7	0.3
60/40	0.6	0.4
50/50	0.5	0.5
40/60	0.4	0.6
30/70	0.3	0.7
20/80	0.2	0.8
10/90	0.1	0.9
0/100	0	1.0

3.5 Analytical techniques

3.5.1 GPC

The M_w and M_n of neat P(3HB-*co*-3HHx) was estimated by GPC at 40 °C using an *Agilent 1200* GPC (USA) coupled with refractive index detector and *Waters Styragel* columns (HR 3 and HR 5E). Chloroform HPLC grade (Fisher Scientific, UK) was used as eluent at flow rate of 0.8 mL min^{-1} and solvent with sample concentration of 1.0 mg mL^{-1}. Polystyrene standards (Sigma-Aldrich, USA) (M_w = 70,000 to 1,000,000 g mol^{-1}) with narrow polydispersity (D) were used to prepare the calibration curve.

3.5.2 Viscosity measurement of P(3HB-*co*-3HHx) in chloroform

The temperature of *Schott CT 52* thermostat bath (Mainz, Germany) was set at 25 °C. The system was allowed to equilibrate for 1 h. After that, a cleaned Ubbelohde *Cannon* viscometer (Capillary no: 0B) was inserted into the thermostat bath in upright position. 15.0 mL of P(3HB-*co*-3HHx) solution was inserted into the filling tube of viscometer by using a *Eppendorf* micropipette (Hamburg, Germany) with the accuracy of ± 0.10 mL. Parts of Ubbelohde viscometer are shown in Figure 3.1. Temperature equilibration was achieved in 10 min (c.f. Figure 3.1). Then, the liquid level in the viscometer was brought above the upper graduation mark of bulb 9. The pipette filler was used to pull the desired liquid level up to bulb 9 through tube 3. At the same time, tube 2 was closed by using finger. The liquid was allowed to drain down the capillary by releasing the finger that covered tube 2. The efflux time started as the meniscus passed the upper graduation mark and stopped as the meniscus passed the lower mark by visual inspection. A digital timer was used to measure efflux time. The efflux time was determined for at least three times. Then, 0.8 mL (0.008 dL) of chloroform was added to bulb 6 through tube 1 in order to reduce the initial concentration of the polymer solution. The liquid level was pulled up and down by using a pipette filler alternately through tubes 1 and 3 in order to mix the solution well. This process was done for about four to five times before the solution was let for three minutes in order to obtain the thermal equilibration at 25 °C. Then, the efflux time of the solution was taken. After that, another 0.8 mL of chloroform was added and the steps above were repeated until different concentrations of P(3HB-*co*-3HHx) were obtained. The viscometer was removed from the thermostat bath and cleaned as instructed in the cleaning method. Then, the viscometer was put in the oven at 100 °C for 45 minutes. All the steps above were repeated to measure the viscosity of P(3HB-*co*-3HHx) with different 3HHx contents.

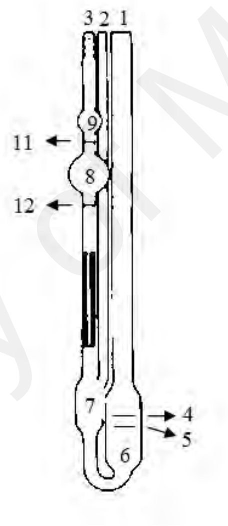

Figure 3.1 Ubbelohde suspended viscometer for measuring viscosity of transparent liquid. The components of this viscometer are: (1) filling tube, (2) venting tube, (3) suction tube, (4) upper filling mark, (5) lower filling mark, (6) solution bulb, (7) suspended level bulb, (8) lower flow bulb, (9) upper flow bulb, (10) lower graduation mark, (11) upper graduation mark.

3.5.3 FTIR

Infrared spectrum was recorded at room temperature by FTIR *Perkin Elmer Spectrum One* spectrometer (USA) equipped with attenuated total reflectance Germanium cell. Sample was placed on top of the crystal and spectra were recorded at a resolution of 2 cm^{-1} with 16 scans. The spectral range was 4000 – 600 cm^{-1}.

3.5.4 Nuclear magnetic resonance (NMR)

The ^{1}H NMR analysis of samples was carried out on *Bruker Avance 300* spectrometer (Bruker Corporation, USA). The 300-MHz ^{1}H NMR spectra was recorded at 30 °C in a $CDCl_3$ solution of polymer solution (1 wt%) with a 10.0-μs pulse width (45° pulse angle), 18-s pulse repetition, and 2000-3000 scan numbers. Tetramethylsilane (TMS) was used as internal reference. The chemical shifts of ^{1}H NMR were recorded in relative to TMS.

3.5.5 Thermogravimetry analysis (TGA)

The thermal decomposition of neat polymer and blends was investigated using *TA Instruments Q500* (USA). Exact mass of 10-20 mg sample was heated from 30 °C to 500 °C at a rate of 10 K min^{-1}.

For the observation of mass changes during reactive blend, it was observed using Netzsch thermogravimetric analyzer (TGA) 209 (Germany) equipped with chiller. An exact mass of 17.000 – 25.000 mg sample was heated up from 30 °C to 195 °C at 10 K min^{-1} in a constant N_2 atmosphere (20 μL min^{-1}) and held isothermally for 5 × $t_{0.5,rb}$ (described later in Section 3.5.6.4). After the isothermal reaction, sample was cooled to 30 °C at 50 K min^{-1}. All thermograms were normalized against empty aluminum pans (Perkin Elmer, Japan).

After reactive blending, 13.000 – 17.000 mg of reacted product [P(3HB-*co*-3HHx)-*graft*-ENR] was subjected to standard heating from 30 °C to 900 °C at 10 K min^{-1} in a constant N_2 atmosphere using the same system. Note that the term "P(3HB-*co*-3HHx)-*graft*-ENR" means there is a chemical (melt) reaction between P(3HB-*co*-3HHx) and ENR.

3.5.6 DSC

Calorimeter measurements were performed in *TA Instruments Q200* (USA) equipped with refrigerated cooling system 90-series under nitrogen atmosphere (purity: 99.9995%; flow rate: 50 mL min^{-1}). High purity indium was used for Tzero calibrations (cell constant and heat capacity).

3.5.6.1 Thermal stability

An exact mass in a range of 3-5 mg purified sample was encapsulated in standard aluminum pan (*Perkin Elmer*, USA) before placing into DSC cell. The sample was heated from 30 °C to different holding temperatures (T_h: 170, 175, 180, 185, and 190 °C) at a heating rate of 10 °C min^{-1}, held for different holding times (t_h: 1, 3, 5, 7, 10, 15, 30 min), and cooled to 30 °C. The change of average molecular weight, crystallinity indicator and crystal lattice was investigated using GPC (Section 3.5.1), FTIR (Section 3.5.3), and XRD (Section 3.5.9), respectively. Analysis of molecular weight is according to procedure shown in Section 3.5.1.

3.5.6.2 Heat-cool-heat

Thermal profile of neat polymer and P(3HB-*co*-3HHx)-*blend*-ENR was investigated using DSC *TA Instruments Q200* (USA). Sample (3.00-10.00 mg) was heated from 30 °C to 175 °C at a rate of 10 K min^{-1}, held for 3 min, followed cooling rapidly to −80 °C and reheated to 30 °C at a rate of 10 K min^{-1} (reheating cycle).

To understand the T_g behavior during reactive blends, an exact mass of 3.00 – 5.00 mg of P(3HB-*co*-3HHx)-*blend*-ENR was heated from 30 °C to 197 °C at a rate of 10 K min^{-1}, hold isothermally at different half-time of melt reaction (for 50/50 blend composition, $t_{0.5,\text{rb}}$ = 13.3 min) and rapidly cooled to −80 °C and reheated to 160 °C at a rate of 10 K min^{-1}.

T_{cc} (cold crystallization temperature) and T_m values were obtained from the maximum peak after linear integration in Universal Analysis 2000. Since multiple endothermic peaks are common in P(3HB-*co*-3HHx) as a result of recrystallization, the area of all the endothermic peaks were used to determine ΔH_m values.

3.5.6.3 Isothermal crystallization and melting behavior

An exact mass of 3.00 - 7.00 mg P(3HB-*co*-3HHx) samples were encapsulated in standard DSC aluminum pans. The isothermal crystallization was performed by the following thermal procedures (a) samples were heated from 30 °C to 175 °C [160 °C for both P(3HB-*co*-8mol% 3HHx) and P(3HB-*co*-12mol% 3HHx)] at a rate of 10 °C min^{-1} for 3 min and rapidly cooled to a predetermined T_c [121-127 °C for P(3HB-*co*-3mol% 3HHx), 111-117 °C for P(3HB-*co*-8mol% 3HHx), and 109-115°C for P(3HB-*co*-12mol% 3HHx)], until complete crystallization where no significant change of heat flow was seen as a function of time. The $t_{0.5}$ can be estimated using horizontal baseline integration. Once $t_{0.5}$ was obtained, the following step was employed to extract the kinetics information: (b) samples were heated from 30 °C to 175 °C [160 °C for both P(3HB-*co*-8mol% 3HHx) and P(3HB-*co*-12mol% 3HHx)] at a rate of 10 °C min^{-1} for 3 min and rapidly cooled to several T_cs and isothermal for five $t_{0.5}$s (to ensure same extent of crystallization for all samples), then the samples were heated again to 175 °C [160 °C for both P(3HB-*co*-8mol% 3HHx) and P(3HB-*co*-12mol% 3HHx)] at a rate of 10 °C min^{-1} to determine the melting point of corresponding polymer crystals. For each experiment, a fresh sample was prepared to minimize the influence of molecular weight degradation on the crystallization behavior. As mentioned before, PHA is known to thermally degrade at and above its melting temperature (Kopinke, Remmler, & Mackenzie, 1996; Li, He, Yu, & Cheung, 2003). Under identical conditions, a single DSC experiment at T_c = const. is used for each regression calculation. The errors were estimated using regression analysis based on 2-tailed student *t*-test at 95% confidence level (refer to Appendix G).

3.5.6.4 Reactive blends

All blend compositions (2.00 - 7.00 mg) were heated from 30 °C to a reaction temperature (T_{rb}) and held isothermally in *TA Instruments Q200* (USA). The T_{rb} ranged from 190 to 197 °C. For isothermal reaction, half-time of isothermal melt reaction ($t_{0.5,rb}$) was calculated.

3.5.7 Polarizing optical microscopy (POM)

Exact amount of 1 g samples from Section 3.4 were dissolved in 10 mL chloroform. Upon complete dissolution, the polymer solution was placed drop-wise on top of a glass cover slip and allowed to dry at room temperature. The cover slip was then placed in vacuum oven at 50 °C for 24 h. All samples were heated from 30 °C to 175 °C at a rate of 10 °C min^{-1}, annealed for 3 min followed by cooling to T_cs (109 – 117 °C. Note: the choice of T_cs was similar as compared to that in the study of isothermal crystallization in DSC) and hold isothermally until complete crystallization. Micrographs of growing spherulites were captured before and after impingement of the spherulites. The time requires for P(3HB-*co*-3HHx) samples to fully impinge is approximately 30-90 min.

The above heating process was performed using a hot stage system (*Mettler Toledo FP82HT,* Switzerland) mounted on an *Olympus BX51* POM (Tokyo, Japan). The POM microscope was equipped with various magnification lenses from 5×, 10×, 20× to 50×. The diameter of developed spherulites was measured using a time-interval function in Olympus software (cellSens standard v1.8), and the final morphology after isothermal crystallization was captured using *Olympus DP26* camera (*Tokyo, Japan*).

3.5.8 Dynamic mechanical analysis (DMA)

DMA film samples were prepared by dissolving 2 g polymers blend in 10 mL of chloroform, as described in Section 3.4.2. The dried film was placed on top of a graph paper, followed vertical cut using a piece of blade and hammer. DMA samples have dimension of ($l \times w \times t$) 30 × 5 × 0.2-0.3 mm^3. Dynamic frequency sweep was carried out on neat and blends of P(3HB-*co*-8mol% 3HHx) and ENR using a *Perkin Elmer DMA 8000* (USA). All samples were tightened in a dual-cantilever clamp at a force of 1 N, and tension mode is applied. The sample was subjected to a frequency sweep from 0.01 Hz to 300 Hz with 22 points per decade at 27 °C while undergoing a dynamic displacement of 0.02 mm. The modulus (storage and loss modulus) and tan δ (loss modulus divided by storage modulus, and is often called damping) were calculated from the actual measured dynamic displacement amplitude.

3.5.9 *X*-ray diffraction (XRD)

XRD experiment was performed using a *PANalytical* (Empyrean, USA) diffractometer with Cu-K$_\alpha$ radiation (λ = 1.5406 Å). The generator was operating at 40 kV and 40 mA. The thermally treated samples after Section 3.5.6.1 were scanned at diffraction angle 2θ from 5° to 60° at a step size of 0.026° at 25 °C.

3.5.10 Scanning electron microscope (SEM)

For SEM investigation, P(3HB-*co*-3HHx) and its blend films obtained from solution casting (w_{ENR} = 0, 0.2 and 0.4) described in Section 3.4.2 were chemically etched in tetrahydrofuran in order to selectively remove ENR phase. Tiny piece of samples film (approximately 5 × 5 × 0.2 mm^3) was dipped inside ACS grade tetrahydrofuran for 4 h at room temperature in a tight-capped glass bottle. The sample was carefully separated from glass bottle and allowed to dry at room temperature followed by further drying in convection and vacuum ovens at 50 °C for 24 h. The etched samples were analyzed with SEM (JEOL JSM6360LA, USA) coupled with in-lens secondary electron detectors operating at 5 kV, 5.7 mm working distance, and 2000× magnification.

CHAPTER IV – RESULTS AND DISCUSSION

4.1 P(3HB-*co*-3HHx)

4.1.1 Biosynthesis of PHA

We begin our discussion on the production of PHA. CPKO is a renewable carbon substrate for PHA production (Loo et al., 2005). In this study, different concentrations of CPKO were fed to the transformant *C. necator* PHB¯4 (pBBREE32d13) harboring PHA synthase of *Aeromonas caviae*. The effect of culture volume was also investigated. Table 4.1 shows the obtained total PHA content and PHA composition with variation of CPKO concentrations. The total PHA (in g L^{-1}) increases with increasing concentrations of CPKO of up to 12.5 g L^{-1}, and gradually decreases beyond this limit. It is assumed that bacteria cells can only sustain a certain amount of oil concentration during PHA production before it becomes an inhibitor. This trend was also observed in previous research. For instance, Bhubalan and coworkers (2010) studied the synthesis of P(3HB-*co*-3HHx) from CPKO fed to *C. necator* transformant harboring phaC of *Chromobacterium* sp. USM2. Their study showed that the yield of PHA increases with increasing CPKO concentration of up to 15 g/L and decreases beyond this limit (Bhubalan, Rathi, Abe, Iwata, & Sudesh, 2010).

Table 4.1 Biosynthesis of P(3HB-*co*-3HHx)[a] using different concentrations of CPKO (results presented in CDW, PHA composition and total PHA produced)

CPKO concentration ($g\ L^{-1}$)	CDW (wt.%)[b]	PHA composition (mol %)		Total PHA ($g\ L^{-1}$)
		3HB	3HHx	
5	63.3 ± 5.1	96	4	3.3
7.5	78.6 ± 6.3	96	4	6.5
10	85.9 ± 1.4	96	4	7.5
12.5	81.1 ± 8.5	97	3	9.2
15	73.9 ± 4.1	97	3	5.8
17.5	71.8 ± 1.4	96	4	6.0

[a] Culture was incubated for 72 h at 30 °C with agitation speed of 200 rpm in mineral salt medium supplemented with 50 $\mu g\ mL^{-1}$ of kanamycin. Initial pH medium was set at 7.

[b] PHA content in freeze-dried cells were determined *via* GC

CDW, cell dry weight

Visual observation during the accumulation of PHA in *C. necator* PHB¯4 is shown in Figure 4.1. *C. necator* PHB¯4 has rod shape morphology. At 12 h of biosynthesis, there is no accumulation of PHA [c.f. Figure 4.1(a)]. As the biosynthesis progressively advances to 72 h, one observes accumulation of PHA as indicated by white reflective pattern in the bacteria cells [c.f. white arrow in Figure 4.1(b)]. Phase-contrast microscope provides a good visual technique to verify if there were any PHA accumulations during biosynthesis.

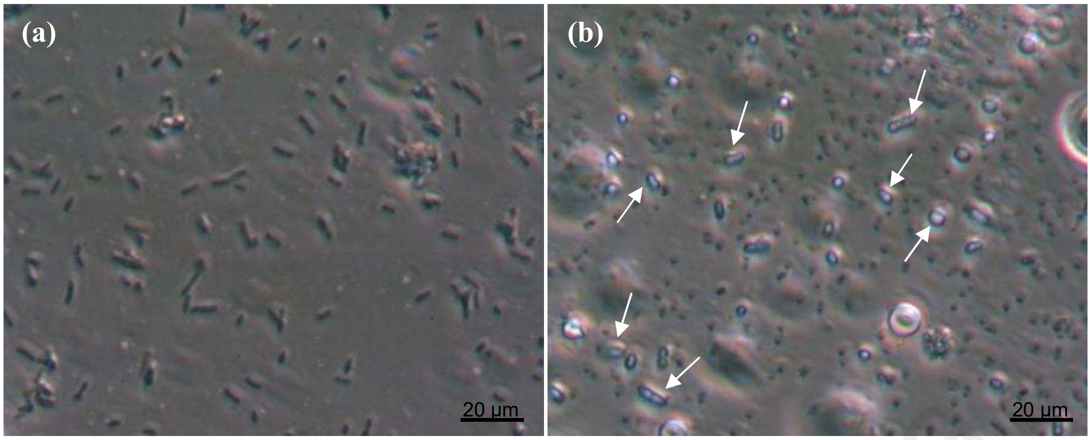

Figure 4.1 Phase-contrast micrographs of *C. necator* PHB¯4 at (a) 12 h and (b) 72 h (white arrows show bacteria strain containing luminescence PHA granules)

Since the synthesis of PHA is primarily aim to produce as much amount as possible for later analyses, it is necessary to understand the effect of culture volume. Table 4.2 summarizes the PHA content and compositions with a variation of culture volumes. It is shown that the total PHA decreases significantly, from 71.7 ± 0.3 wt% to 41.3 ± 3.1 wt%, when the culture volume increases from 200 mL to 400 mL culture volume in 1000 mL volumetric flasks. This result is reasonable considering that the ratio of optimum culture volume to available oxygen in the system is approximately 1:5 (Loo et al., 2005).

Table 4.2 Effect of culture volume on the accumulation (CDW and 3HHx content) of P(3HB-*co*-3HHx)[§] in *C. necator* PHB¯4

Culture volume (mL)	CDW (wt.%)	3HHx content (mol %)
200	71.7 ± 0.3	3
300	49.8 ± 3.6	3
400	41.3 ± 3.1	5

[§] Culture was cultivated in mineral salt medium containing 12.5 g L^{-1} CPKO for 72 h at 30 °C with agitation speed of 200 rpm and initial pH at 7.

4.1.2 Structure elucidation (FTIR and NMR)

The molecular structure of synthesized PHA is confirmed and carried out using NMR and FTIR. The observed ^{1}H NMR spectra at 300 MHz of all P(3HB-*co*-3HHx) containing different 3HHx contents show that there are triplet resonance at 0.9 ppm and doublet resonance at 1.3 ppm, which can be assigned to methyl protons of 3HHx and 3HB unit, respectively. The methylene proton resonance at 2.5-2.7 ppm is associated to methine proton of 3HB and 3HHx units, while the multiplet resonance at 5.3 ppm is assigned to methine proton of both 3HB and 3HHx units. The chemical shift assignment for each proton resonance is accordance to Doi and co-workers (1995) (Doi et al., 1995) and two examples e.g. P(3HB-*co*-3mol% 3HHx) and P(3HB-*co*-12mol% 3HHx) are shown in Appendix A.

Besides peaks assignment, NMR is also a useful tool to determine monomer content of a copolymer. In the case of P(3HB-*co*-3HHx), the mole fraction of 3HHx can be determined from the intensity ratio of the doublet CH_3-proton resonance at 1.3 ppm to the triplet CH_3-proton resonance at 0.9 ppm (Doi, Kunioka, Nakamura, & Soga, 1986). An example of NMR spectrum of P(3HB-*co*-12mol% 3HHx) revealed that the monomer content of 3HHx is 10 mol% (Appendix A). This value is very close to that of P(3HB-*co*-12mol% 3HHx) given by KANEKA Corporation. The other two copolymers containing 3mol% and 8mol% of 3HHx were not determined.

FTIR spectroscopy is a versatile tool that provides a wealth of information about molecular structure of PHA. The absorption bands explain availability of functional groups and its deformations. The characteristic vibrational frequencies of P(3HB-*co*-3HHx) containing different mol% of 3HHx are summarized in Table 4.3. In general, the spectra of all P(3HB-*co*-3HHx) having different mol% of 3HHx do not show clear distinction. The main functional group that characterizes P(3HB-*co*-3HHx) is located at 1719 cm^{-1}, which represents the absorption spectra of anti-symmetric stretching of carbonyl group (C=O). Other important absorptions band are –C–O–C– , which is located at 1130 and 1350 cm^{-1}, –O–H stretching at 3400 cm^{-1}, –C–H stretching at 2850 – 3000 cm^{-1} and –C–H deformation at (rocking) 1055 cm^{-1} and (bending) 825 – 980 cm^{-1}. The absorption band at 1380 cm^{-1} ($\delta_s CH_3$) is insensitive to crystalline phase of P(3HB-*co*-3HHx) (Xu et al., 2002). For more detailed visual observation of P(3HB-*co*-3HHx) spectra, please refer Appendix B.

Table 4.3 Assignment FTIR peaks of P(3HB-*co*-3HHx)

Absorption bands (cm^{-1})			Assignment peaks
3 mol% 3HHx	8 mol% 3HHx	12 mol% 3HHx	
3400	3400	3400	O–H stretching
2976	2976	2976	sp^3 C-H stretching
2933	2935	2934	sp^3 C-H stretching
1719	1720	1719	sp^2 C=O stretching (C)
1452	1457	1452	sp^3 C-H bend (alkanes) (C)
1379	1380	1379	sp^3 C-H bend (alkanes), which is insensitive to the degree of crystallinity
1261	1262	1262	sp^3 stretching vibration of acyl C-O (ester) (A)
1227	1228	1227	sp^3 stretching vibration of acyl C-O (ester) (C)
1180	1181	1180	$\nu_{as}C{-}O{-}C$ (A)
1130	1131	1130	sp^3 stretching vibration of alkoxy C-O (ester)
1100	1100	1100	sp^3 stretching vibration of alkoxy C-O (ester)
1054 / 1044	1055 / 1045	1054 / 1044	rocking of $C{-}CH_3$
979	979	979	sp^2 CH bend of monosubstituted alkene (C)

(C) crystalline sensitive band
(A) amorphous sensitive band

4.1.3 Intrinsic viscosity and viscosity constant

The viscosity data of dilute solution containing P(3HB-*co*-3HHx) was studied with Ubbelohde viscosimeter at 25 ± 0.2 °C. The viscosimeter of water and chloroform was performed and the results were summarized in Appendix C. All other viscosity data for P(3HB-co-3HHx) were also summarized in the same section. The correlation between the intrinsic viscosity (η), Huggins' constant (K_H) and co-monomer content of P(3HB-*co*-3HHx) is shown in Figure 4.2 and Figure 4.3, respectively. The viscometry analysis of P(3HB-*co*-3HHx) solution reveals that the slope of η_{spec}/C versus C curve (c.f. Appendix C), Huggins' constant, and the intrinsic viscosity are all dependant on the co-monomer content of P(3HB-*co*-3HHx). From Figure 4.2, there is a dramatic decrease of intrinsic viscosity showing that chloroform turns from good solvent for P(3HB) to increasingly poor solvent with addition of 3-hydroxyhexanoate. The intrinsic viscosity $[\eta]$ decreases from 2.95 dL g^{-1} in P(3HB) (Chee, Kummerlöwe, Lechner, & Kammer, 2004) to 2.07 ± 0.04 dL g^{-1}, 1.49 ± 0.04 dL g^{-1}, 1.53 ± 0.03 dL g^{-1} and 1.03 ± 0.03 dL g^{-1} in co-polymers containing 3 mol%, 8 mol%, 12 mol% 3HHx and 35 mol% 3HHx, respectively) (c.f. Figure 4.2). Looking at the viscosity, we have swollen chains of P(3HB) in a good solvent thus the viscosity is high. With increasing 3HHx contents, the solvent is not anymore a good solvent and the coils shrink. The coils do not like anymore surrounding liquid. Qualitatively, the same we got to know from K_H values in Figure 4.2. In general observation, the K_H values range from $0.3 < K_H < 0.4$ for good solvent. Thus, behavior of $[\eta]$ and K_H are consistent.

Figure 4.3 illustrates the relationship between intrinsic viscosity and coil size, and is given as $[\eta]N_{HB} \propto R^3$. The coil size reduces when 3HHx content increases. Apparently, this agrees well to the result discussed in Figure 4.2. The calculation of N_{HB} is shown in Figure 4.3.

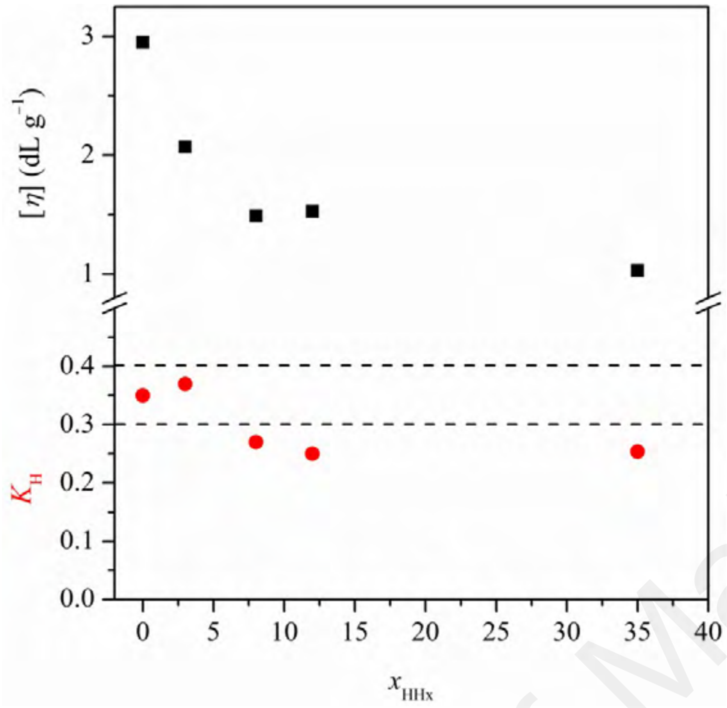

Figure 4.2 Plot of [η] and K_H versus 3HHx fraction (x_{HHx}) in the copolymer of P(3HB-*co*-3HHx)

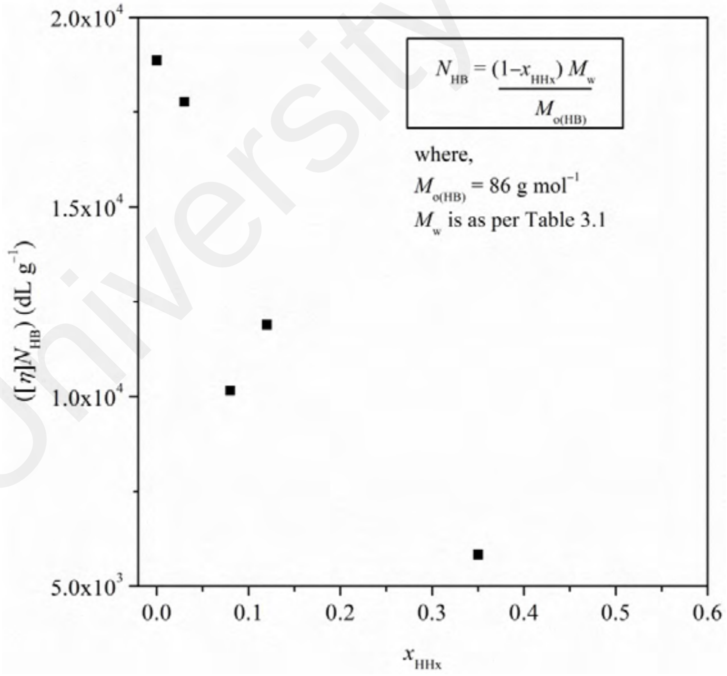

Figure 4.3 Coil size against co-monomer content of P(3HB-*co*-3HHx)

4.1.4 Thermal decomposition

4.1.4.1 TGA

Thermogravimetric curve of P(3HB-*co*-3HHx) containing different mol% of 3HHx is shown in Figure 4.4. The decomposition temperatures of P(3HB-*co*-3HHx) start from ~260 °C (onset temperature) and end around 290 °C (endset temperature). All 1st derivatives of weight % curves exhibit similar shape with one step decomposition. This implies that the mechanism or kinetic of thermal decomposition obeys the same pathway in P(3HB-*co*-3HHx) of different contents of 3HHx. The observed thermal decomposition range is similar to that of other reported results in literatures. For instance, Li and coworkers (2003) investigated the thermal degradation products of P(3HB) and P(3HB-*co*-3HV) by means of TGA/FTIR and pyrolysis GC coupled with mass spectrometer (Li et al., 2003; Li, Yu, & Cheung, 2001). They showed that P(3HB) and P(3HB-*co*-3HV) decomposes at 260–290 °C and 280–320 °C, respectively. Although there was no precise information on the molecular masses of both P(3HB) and P(3HB-*co*-3HV), the derivative thermograms also exhibited similar shape. The degradation of PHA is initiated from the random chain scission of ester linkage, and the products of decomposition are mainly propene, 2-butenoic acid, propenyl-2-butenoate and butyric-2-butenoate (due to 3HB component), propenyl-2-pentenoate and pentanoic-2-pentenoate (due to 3HV component), and CO_2. Further analysis of degraded products during thermal decomposition was not performed. The rate of thermal decomposition is of the interest.

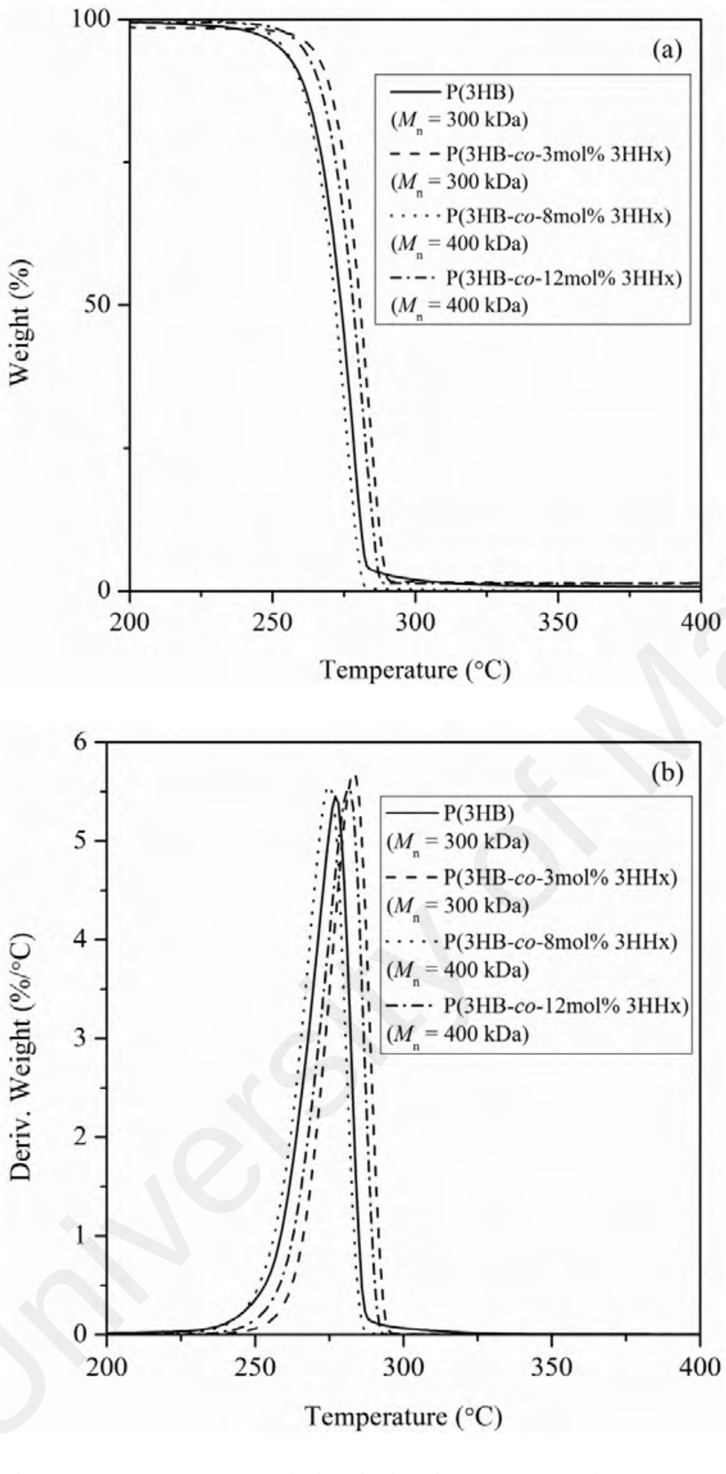

Figure 4.4 (a) TGA and (b) derivative curves of P(3HB-*co*-3HHx) of different mol% of 3HHx with respect to P(3HB) as a reference

Ariffin and coworkers (2008) reported two mixed mechanisms for decomposition of P(3HB), which are: 1) random thermal degradation with auto-accelerated transesterification and 2) kinetically favored chain reaction from crotonate chain ends. These mechanisms are dependent on time and/or temperature (Ariffin, Nishida, Shirai, & Hassan, 2008), as shown in Figure 4.5.

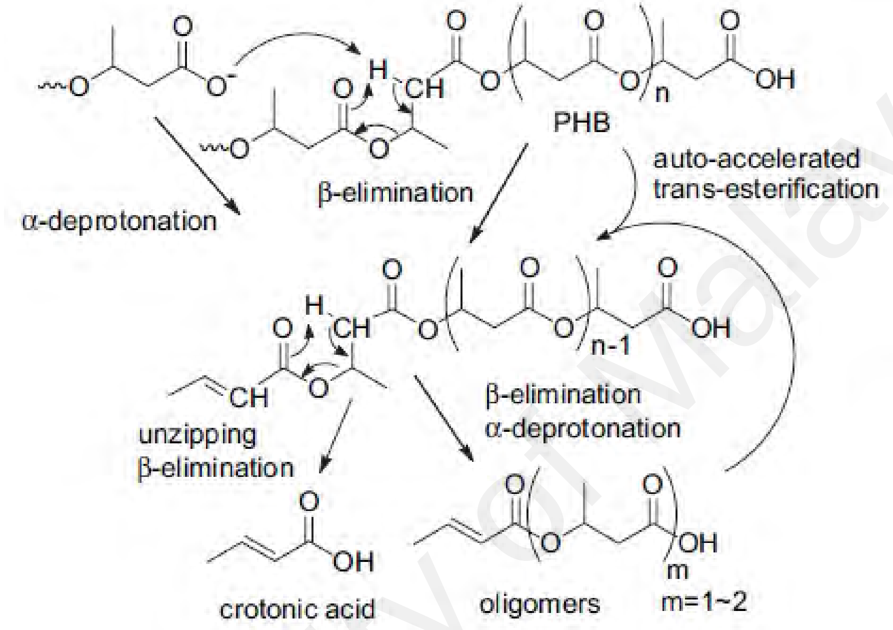

Figure 4.5 Expected thermal degradation pathways of P(3HB) (Ariffin et al., 2008)

When comparing different P(3HB-*co*-3HHx) thermograms, we suggest that the amount of second monomer (in mol%) present in a polymer chain does not have significant influence on thermal decomposition. Instead, the molecular masses play a prominent role towards the degree of decomposition. For example, P(3HB-*co*-3mol% 3HHx) and P(3HB-*co*-12mol% 3HHx) have higher molecular masses than P(3HB-*co*-8mol% 3HHx) therefore they have higher thermal decomposition temperature. A direct study on the effect of molecular mass of PHA towards thermal decomposition is not available as yet. Nevertheless within the same macromolecule system (in general, high molecular mass polymer), Calahorra and co-workers (1989) had shown that the thermal stability of cellulose increases with increasing molecular mass (Calahorra, Cortazar, Eguiazabal, &

Guzman, 1989). It should also be noted that the side chains of PHA with a finite number of carbon do not have significant variation in terms of thermal decomposition behavior. For instance, Lee and co-workers (2001) showed in their study that PHAs with different side chain lengths, such as P(3HB), P(3HB-*co*-3HV) and P(3HB-*co*-4HB), exhibit a single transition degradation process with almost similar maximum decomposition temperatures (M. Y. Lee, Lee, & Park, 2001).

Figure 4.6 shows the plot of *ln*|deriv. weight loss| against 1/*T* for neat P(3HB-*co*-3HHx). The activation energy was calculated from the initial decomposition (linear region as indicated by arrow in Figure 4.6). More detailed calculations related to the calculation of activation energy during thermal decomposition of P(3HB-*co*-3HHx) having different 3HHx contents were summarized in Appendix I. The corresponding activation energies (*E*) during initial thermal decomposition of the co-polymer are 378 kJ (3 mol% 3HHx), 302 kJ (8 mol% 3HHx), and 347 kJ (12 mol% 3HHx). The activation energy during initial decomposition of P(3HB) is 291 kJ. Higher values in the co-polymer containing 3 and 12 mol% of 3HHx as compared to P(3HB) and P(3HB-*co*-8mol% 3HHx) could possibly come from higher molecular masses. These values are in agreement to earlier observation, that there is a decline of energy barrier and decomposition temperature when the molecular masses of P(3HB-*co*-3HHx) are lower.

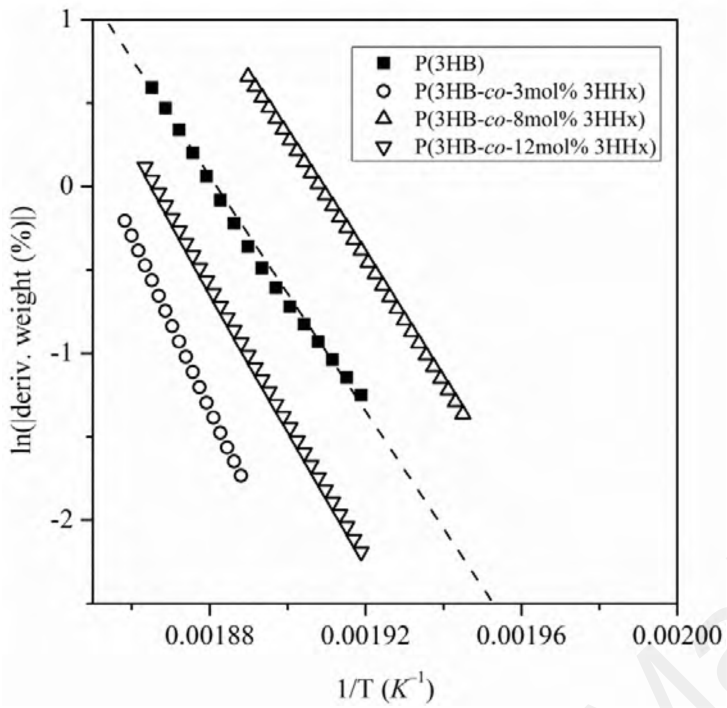

Figure 4.6 Plot of *ln*|deriv. weight| against 1/*T* for neat P(3HB-*co*-3HHx) [dashed line in P(3HB) sample is for visual aid]

4.1.4.2 Isothermal heat treatment

Isothermal degradation of P(3HB-*co*-3HHx) having different mol% of 3HHx was carried out in N_2 atmosphere at 170, 175, 180, 185, and 190 °C, respectively. According to numerous published sources, PHA undergoes random chain scission at temperature above its melting temperature (Aoyagi, Yamashita, & Doi, 2002; Ariffin et al., 2008; Kopinke et al., 1996; Li et al., 2003). When the chain scission of PHA is random, the rate constant of degradation (k_{d}) can be predicted using Eq. (4.1) (Jellinek, 1955):

$$\frac{1}{P_{\mathrm{n},t_{\mathrm{h}}}} = k_{\mathrm{d}} t_{\mathrm{h}} + \frac{1}{P_{\mathrm{n},0}} \qquad (4.1)$$

where, $P_{\mathrm{n},0}$ and $P_{\mathrm{n},t_{\mathrm{h}}}$ are the number-average degrees of polymerization at time 0 and t_{h}, respectively. To simplify the equation and adopt to our system, we replace $P_{\mathrm{n},0}$ and $P_{\mathrm{n},t}$

with $M_{w,0}$ and M_{w,t_h}, where $M_{w,0}$ and M_{w,t_h} are the weight-average molecular weight of P(3HB-*co*-3HHx) at a given time 0 and t_h, respectively. This arrives to Eq. (4.2):

$$\frac{1}{M_{w,t_h}} = k_d t_h + \frac{1}{M_{w,0}} \tag{4.2}$$

The values of $M_{w,0}$ for P(3HB-*co*-3HHx) containing different mol% of 3HHx were obtained before any heat treatment, while the values of M_{w,t_h} were the values obtained after isothermal treatment at time t_h. After isothermal treatment, samples were also subjected to GPC, FTIR and WAXD analyses. For simplicity purpose, M_{w,t_h} is referred as M_w in the discussion below. It is also important to note that P(3HB) underwent the same isothermal treatment as P(3HB-*co*-3HHx), but the P(3HB) sample after isothermal treatment had an issue of dissolution in chloroform at 50 °C after extended storage period. A comparison of the rate constant of isothermal degradation using P(3HB) as a reference polymer was made using a published result (Hablot, Bordes, Pollet, & Averous, 2007) (refer Table 4.4).

Figure 4.7(a) shows an example of reciprocal changes of the M_w of P(3HB-*co*-3mol% 3HHx) at various T_hs, and Figure 4.7(b) shows M_w changes for different molar compositions of P(3HB-*co*-3HHx) at same T_h. There is a linear relationship in accordance to random chain scission phenomena in all studied P(3HB-*co*-3HHx). According to Aoyagi and coworkers (2002), if the plots of $1/M_w$ *versus* t_h were convex, the thermal degradation does not proceed *via* simple random scission of the polymer chain (Aoyagi et al., 2002). Figure 4.7(a) and 4.7(b) show that in all cases, linear regression are followed for the reciprocal of M_w vs t_h. This implies simple random scission of polymer chains takes place above the melting temperature of P(3HB-*co*-3HHx). In our case, the weight of P(3HB-*co*-3mol% 3HHx) decreases linearly with increasing isothermal temperature and time. Similar trend is observed for isothermal degradation of P(3HB-*co*-8mol% 3HHx) and P(3HB-*co*-12mol% 3HHx) at 170-190 °C. At the same isothermal degradation temperature, the weight loss of P(3HB-*co*-3HHx) containing higher 3HHx is more prominent. Complete changes in the M_w and M_n are tabulated in Appendix D.

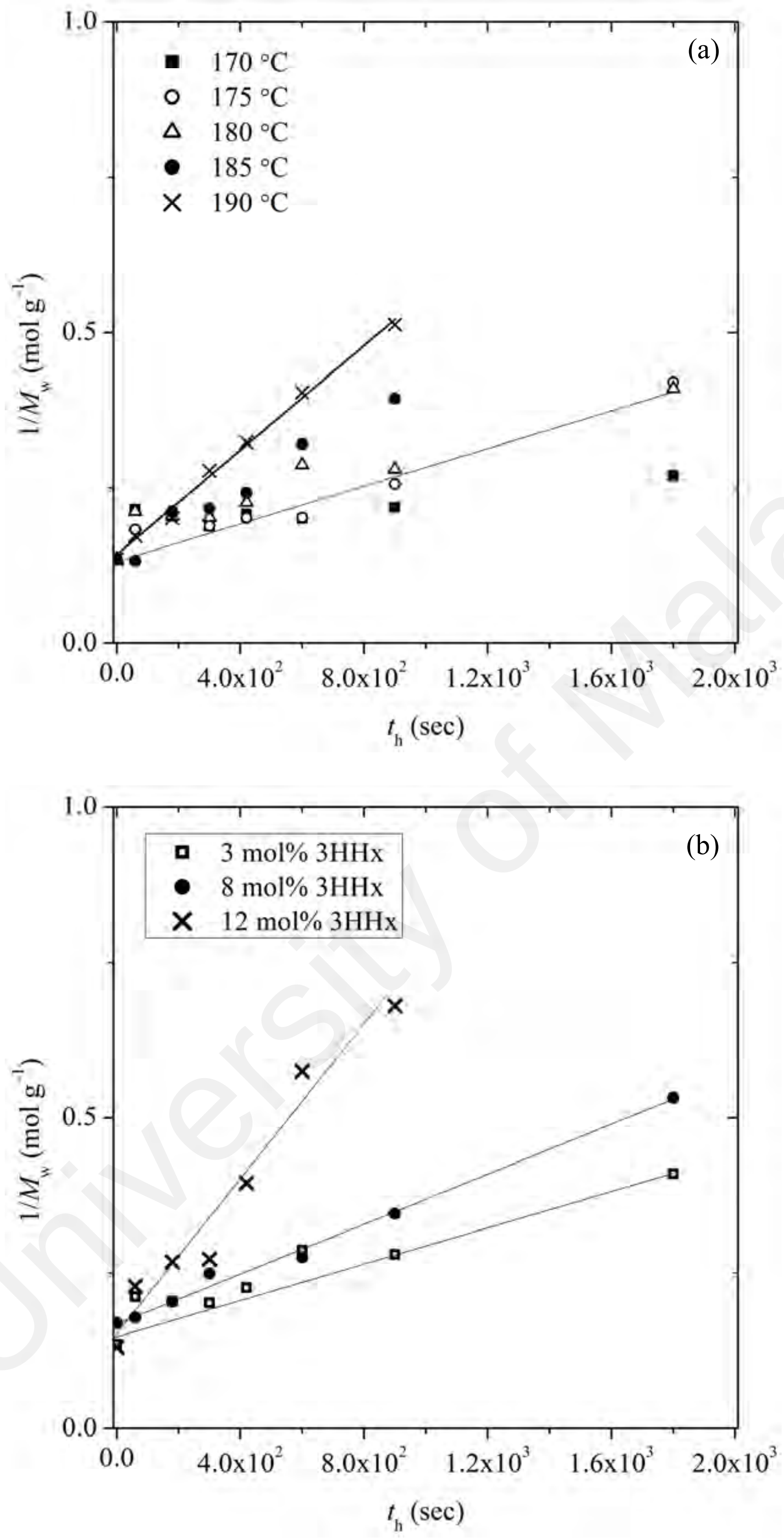

Figure 4.7 Reciprocal M_w against t_h for (a) P(3HB-*co*-3mol% 3HHx) at various T_hs, and (b) different molar compositions in P(3HB-*co*-3HHx) at T_h=180 °C

Figure 4.8 shows the rate constant of isothermal molecular degradation of P(3HB-*co*-3HHx) containing 3, 8, and 12 mol% of 3HHx. At T_h = 170 °C, the k_d values of the co-polymers that contain 0 [P(3HB) as a reference], 3, 8, and 12 mol% of 3HHx, respectively, are 0.03×10^{-7} s^{-1}, 380×10^{-7} s^{-1}, 1000 $\times10^{-7}$ s^{-1}, and 3100×10^{-7} s^{-1}. It seems that the longer carbon backbone in the polymer results in the increase of rate of isothermal degradation. This could be closely related to the lowering of melting temperatures with increasing 3HHx contents. For instance, P(3HB) has a melting temperature of approximately 180 °C while P(3HB-*co*-12mol% 3HHx) has a melting temperature of approximately 140 °C. As the choice of temperatures used in isothermal treatment was 170-190 °C and PHA in general is known to degrade at and above its melting temperature, it is logical that the co-polymer e.g. P(3HB-*co*-12mol% 3HHx) with lower melting temperature experiences higher thermal degradation thus results in higher loss of molecular masses. In the same copolymer, the rate constant of isothermal molecular degradation increases with isothermal temperature. The molecular weight of copolymer decreases in a rapid manner with increasing temperature. The time-dependent profiles of weight loss shown in this study are in accordance to the results of homo-polymer P(3HB) obtained by Aoyagi and co-workers (2002) (Aoyagi et al., 2002). A summary of rate constant of isothermal degradation at various T_hs for P(3HB-*co*-3HHx) are shown in Table 4.4.

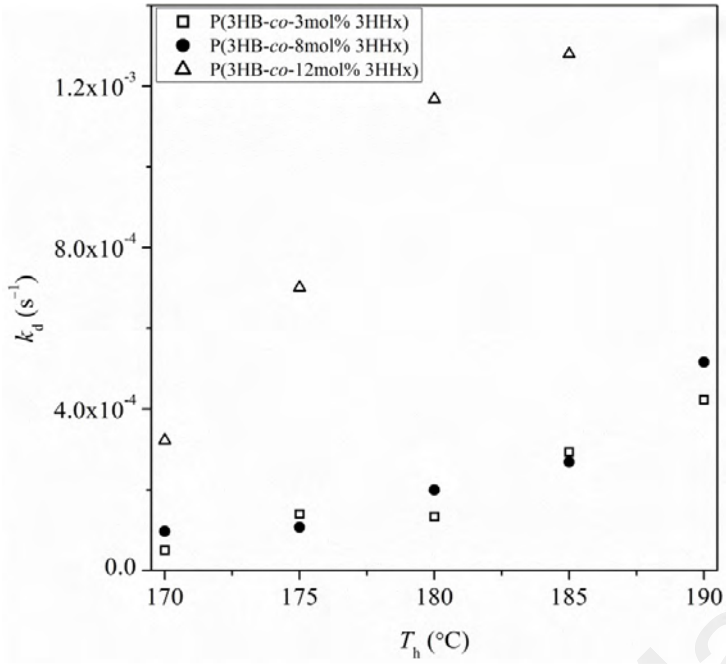

Figure 4.8 Rate constant of isothermal degradation of P(3HB-*co*-3HHx) at various T_hs (□: 3 mol% 3HHx, ●: 8 mol% 3HHx, Δ: 12 mol% 3HHx)

Table 4.4 Summary of rate constant of isothermal degradation for P(3HB-*co*-3HHx)s treated at various T_hs

P(3HB-*co*-*x*mol% 3HHx)	T_h (°C)	$k_d \times 10^{-7}$ (s^{-1})	r^2
$x = 0$ [data adopted from Table 6 in (Hablot et al., 2007)]	170	0.03	0.935
$x = 3$	170	380	0.866
	175	1400	0.957
	180	1200	0.970
	185	3000	0.983
	190	4200	0.997
$x = 8$	170	1000	0.949
	175	1100	0.997
	180	2000	0.996
	185	2700	0.997
	190	5100	0.998
$x = 12$	170	3100	0.961
	175	7200	0.964
	180	12000	0.964
	185	13000	0.976
	190	-	-

The changes of molecular structure of P(3HB-*co*-3HHx) after isothermal degradation were investigated by mean of FTIR and XRD analyses. Figure 4.9 shows an example of FTIR spectra of P(3HB-*co*-8mol% 3HHx) before and after isothermal degradation. The experiment of FTIR after isothermal treatment was limited only to P(3HB-*co*-3HHx) containing 3 mol% and 8 mol% of 3HHx, while the XRD analysis was limited only to P(3HB-*co*-8mol% 3HHx) sample.

In IR analysis, all absorption bands retain their wavenumbers after isothermal degradation. It can be appreciated that there is no obvious change to the molecular structure of P(3HB-*co*-3HHx) despite having lower molecular mass. The intensity of many absorption bands decreases. For example, the asymmetrical C=O stretching vibration at 1720 cm^{-1}, which represents highly ordered P(3HB-*co*-3HHx) chain, decreases after thermal treatment at 170 °C for 30 mins. Other intensities of the important absorption bands at 1131, 1181, 1228, 1262, and 1276 cm^{-1} also decrease after thermal treatment. To further investigate the influence of isothermal treatment to molecular structure of P(3HB-*co*-3HHx), we calculate the crystallinity indicator (*c.i.*) as proposed by Galego et al (2000).

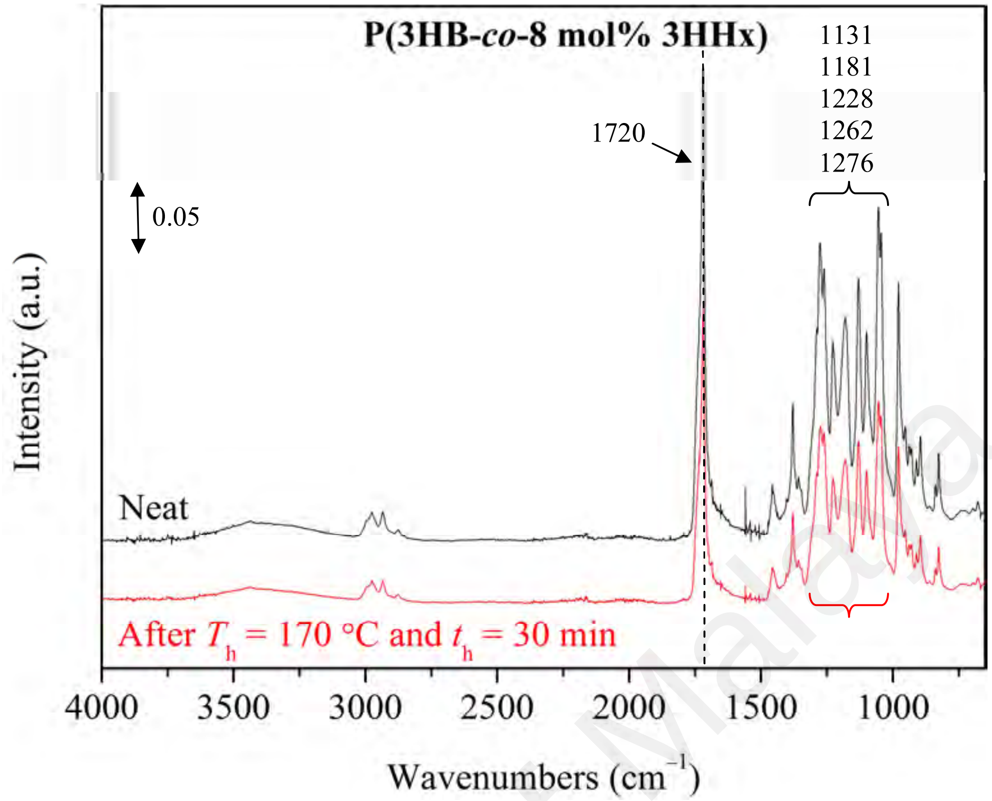

Figure 4.9 FTIR spectra of neat P(3HB-*co*-8mol% 3HHx) and P(3HB-*co*-8mol% 3HHx) after isothermal heat treatment at T_h = 170 °C, t_h = 30 min (dashed line is for visual aid)

The term *c.i.* can be calculated from a ratio between the area of absorption band at 1380 cm^{-1} [sp^3 C-H bend (alkanes) as a reference peak] and 1182 cm^{-1} (ν_{as} C-O-C, amorphous peak), according to the following formula, Eq (4.2):

$$c.i. = \frac{A_{1380}}{A_{1182}} \tag{4.2}$$

The *c.i.* does not represent the absolute amount of crystallites in a semi-crystalline polymer (Galego et al., 2000). The application of this formula allows one to compare relative value related to the crystallinity after isothermal treatment. Our results show that the *c.i.* of P(3HB-*co*-3HHx) do not vary with isothermal heat treatment at a particular mol% of 3HHx. The *c.i.* of P(3HB-*co*-3mol% 3HHx) and P(3HB-*co*-8mol% 3HHx) is around 0.36 – 0.45 and 0.25 – 0.31, respectively (c.f. Table 4.5). One could see that the crystallinity is not influenced by the thermal degradation. The average *c.i.* of P(3HB-*co*-3mol% 3HHx) (average *c.i.* = 0.40) is higher to that (*c.i.* = 0.28) of P(3HB-*co*-8mol% 3HHx). Very minor reduction (almost negligible) of *c.i.* with the increase of second monomer was also observed by other researchers. For instance, Galego and co-workers (2000) used the intensity peak without any peak fitting and found that the *c.i.* for P(3HB) at 0.95 reduced to 0.93 when 8 mol% of 3HV is present. This value decreased further to 0.87 with increasing 3HV content (Galego et al., 2000). Following Galego study, Simon-Colin et al (2008) showed that mcl-PHA has a crystallinity indicator of 0.32 and 0.37 for *mcl*-PHA with T_g of −41 and −50 °C.

Table 4.5 Crystallinity indicator of P(3HB-*co*-3HHx) for different thermal treatments

T (°C)	*t* (min)	*c.i.*	
		P(3HB-*co*-3mol% 3HHx)	P(3HB-*co*-8mol% 3HHx)
170	1	0.39	0.28
	3	0.40	0.29
	5	0.40	0.25
	7	0.40	0.27
	10	0.45	0.29
	15	0.40	0.28
	30	0.40	0.31
180	1	0.37	0.27
	3	0.38	0.27
	5	0.38	0.26
	7	0.36	0.25
	10	0.41	0.27
	15	0.36	0.27
	30	0.37	0.31
Average *c.i.* for individual column		0.40	0.28

To confirm preceding IR analysis [that the crystallinity indicator of P(3HB-*co*-3HHx) is somewhat not influenced after isothermal treatment], we performed WAXD analysis on selected P(3HB-*co*-8 mol% 3HHx) sample. Figure 4.10 shows the *X*-ray diffractograms of P(3HB-*co*-8mol% 3HHx) before and after isothermal treatment recorded at room temperature. The P(3HB-*co*-8mol% 3HHx) before isothermal treatment exhibits primarily two diffraction patterns at 2θ equals to 14° [(hkl) = (020) crystal plane] and 18° (110 crystal plane). The *d*-spacing calculated using Bragg's equation (n $\lambda = 2d \sin \theta$, where λ = 0.154 nm, n = 1) at 2θ = 14° is 6.2 nm. Before calculating the *d*-spacing, the diffractograms shown in Figure 4.10 have to be subtracted against a baseline. An example of baseline subtraction is shown in Figure 4.11. This subtraction process was performed in HighScore Plus software v3.0.4 (MenuBar>Treatment>Determine Background> Subtract).

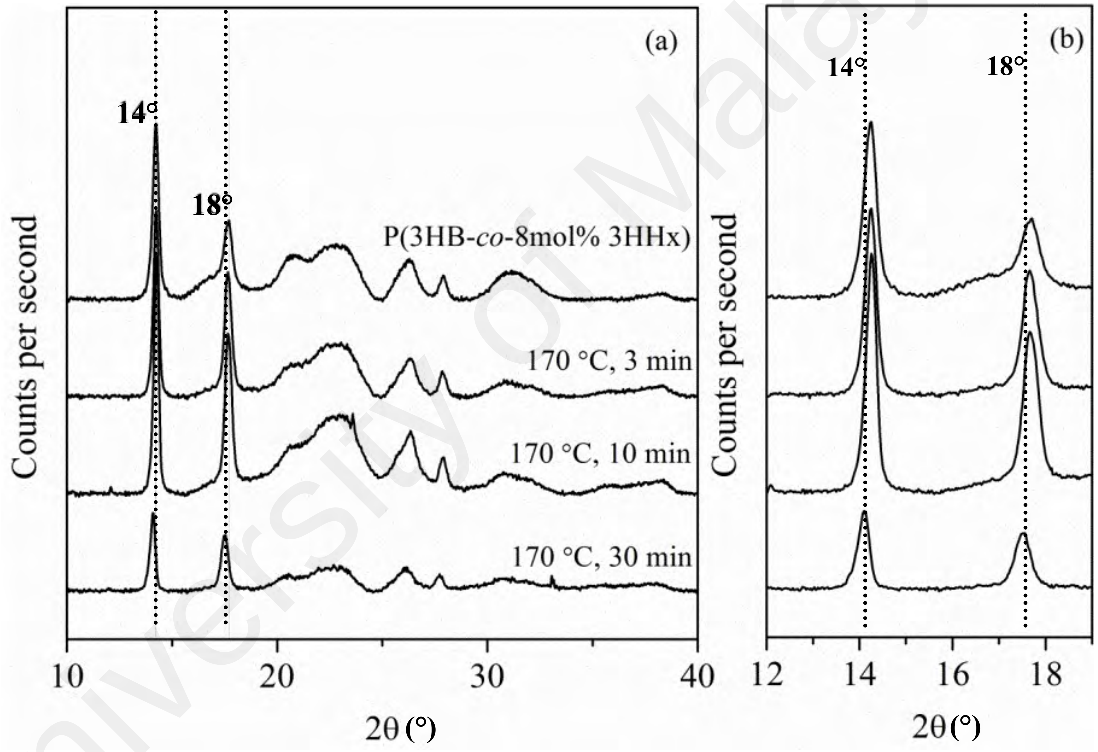

Figure 4.10 *X*-ray diffractograms of P(3HB-*co*-8mol% 3HHx) before and after isothermal degradation (from top to bottom: control or P(3HB-*co*-8mol% 3HHx), and the same polymer after isothermal treatment at 3 min, 10 min, and 30 min). (a) Full spectrum of 2θ from 10° to 40°, and (b) magnified 2θ region from 12° to 19°.

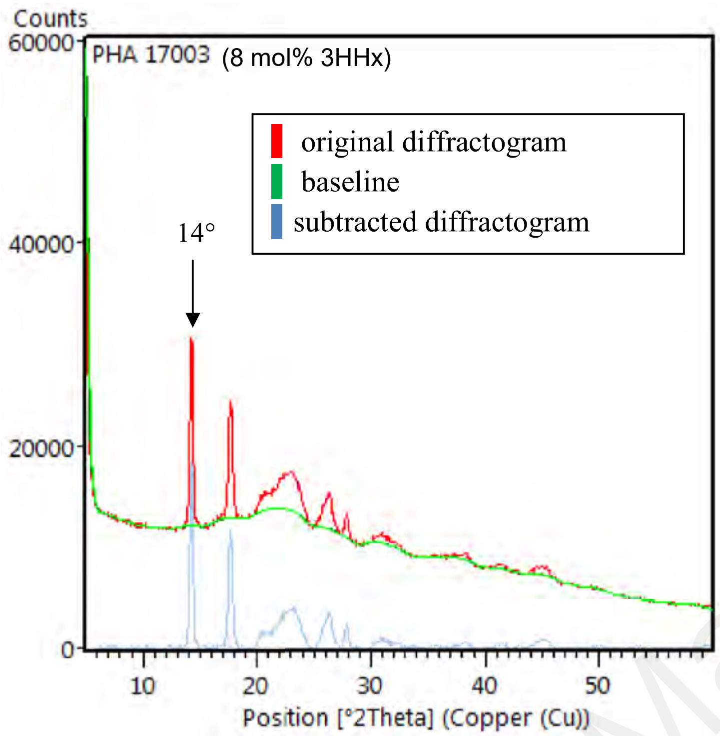

Figure 4.11 An example of baseline subtraction of P(3HB-*co*-8mol% 3HHx) diffractogram that had been isothermally treated at 170 °C for 3 min

These diffraction patterns are similar to that reported by Doi (Doi et al., 1995) and Sato (H. Sato et al., 2004). After thermal treatment, the 2θ and *d*-spacings of P(3HB-*co*-8mol% 3HHx) do not change. For instance, after 3, 10 and 30 min of isothermal treatment, the *d*-spacing at 2θ = 14° is 6.2, 6.2 and 6.3 nm, respectively. This could mean that isothermal heat treatment has little impact on the crystal structure (or lattices) of P(3HB-*co*-8mol% 3HHx). From FTIR and XRD results, it can be deduced that the isothermal treatment does not have significant effect on the crystal structure and molecular structure of P(3HB-*co*-3HHx)s even though their molecular masses reduce as a function of isothermal holding time, and isothermal treatment temperature.

4.1.5 Thermal profile using DSC

4.1.5.1 Heat-cool-heat

From heat-cool-heat experiment, one observes related thermal events of P(3HB-*co*-3HHx) as illustrated in Figure 4.12 for the reheating cycle. Figure 4.12 shows an example of three thermal events during the reheating of P(3HB-*co*-8mol% 3HHx) such as T_g, T_{cc} and T_m. The T_g of P(3HB-*co*-8mol% 3HHx) is located at 0 °C, and the ΔC_p value is 0.48 J (g °C)$^{-1}$. Quantity T_g is defined as the midpoint of half-extrapolated tangent between the two transitions. The melting of spherulites formed during cold crystallization (T_{cc} = 60 °C) is located at 117 °C and 136 °C. In accordance, the melting peak of P(3HB-*co*-3mol% 3HHx) is higher than that of P(3HB-*co*-8mol% 3HHx) while the melting temperature of P(3HB-*co*-12mol% 3HHx) is similar to that of P(3HB-*co*-8mol% 3HHx). All P(3HB-*co*-3HHx) containing different mol% of 3HHx have multiple melting peaks. The existence of multiple melting peaks is discussed later. The observable melting peaks of P(3HB-*co*-3HHx) is much lower than that of homo-polymer P(3HB). It is well known that the melting temperature of P(3HB-*co*-3HHx) reduces with increasing 3HHx content. The melting temperatures of P(3HB) are in the range of 180-190 °C (Ariffin et al., 2008; Gunaratne, Shanks, & Amarasinghe, 2004; Xu et al., 2002). The lowering of melting peaks in P(3HB-*co*-3HHx) as compared to P(3HB) is attributed to longer backbone that disrupts the orientation of main polymer chain. Higher content of 3HHx in the copolymer also reduces the melting temperature.

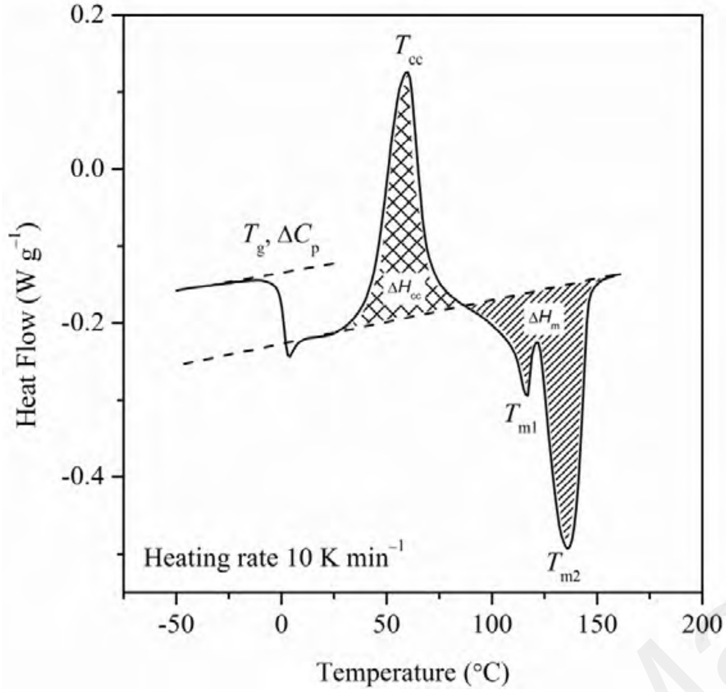

Figure 4.12 DSC curve of P(3HB-*co*-8mol% 3HHx) during second heating

4.1.5.2 Apparent melting temperatures and equilibrium melting temperatures after isothermal crystallization temperature

The melting temperatures of different P(3HB-*co*-3HHx)s were investigated after isothermal crystallization mentioned in Section 3.5.6.3. Figure 4.13 illustrates an example of the melting peaks of P(3HB-*co*-3mol% 3HHx) after isothermal crystallization at various T_cs (121-127 °C). Here, one clearly observes two T_ms at 156 °C and 163 °C in P(3HB-*co*-3mol% 3HHx) isothermally crystallized at 121 °C. First melting peak gradually increase with increasing isothermal temperatures. However, the second melting peak gradually disappears with increasing isothermal temperatures. Multiple melting peaks in P(3HB-*co*-3HHx) could be due to compositional heterogeneity, different crystalline phase formed during isothermal crystallization, or re-crystallization during heating. With the disappearance of second melting peak, it can be appreciated that the lower melting peak in P(3HB-*co*-3mol% 3HHx) is due to the primary crystallites that are formed during isothermal crystallization, while the higher melting peak is due the melting of recrystallize crystals. At lower isothermal crystallization temperature, the formation of spherulites is faster thereafter it may not allow formation of more perfect crystals as compared to that at higher isothermal crystallization temperature. Hence, during the heating cycle, the formation of more perfect crystal during recrystallization may take place and we may observe additional higher melting peak. The formation of spherulites and growth rate analysis is discussed later.

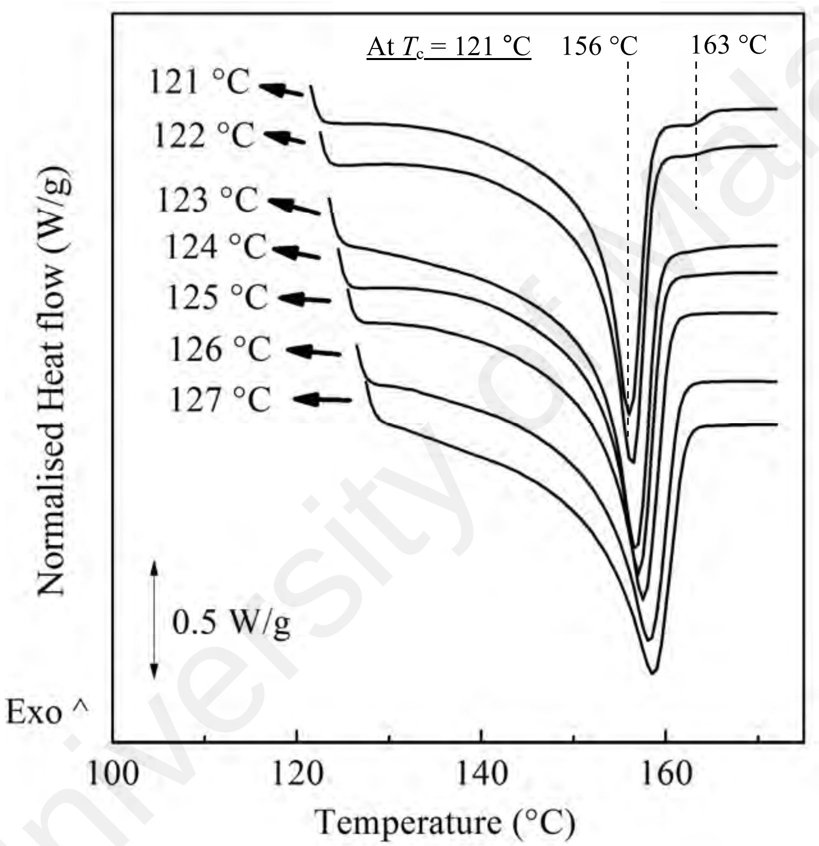

Figure 4.13 Melting temperature of P(3HB-*co*-3mol% 3HHx) after isothermal crystallization for 5 × $t_{0.5}$ at preselected T_c

There is also occurrence of multiple melting peaks in P(3HB-*co*-3HHx) containing 8 mol% and 12 mol% 3HHx, but with more obvious shoulder peaks detectable at lower temperatures (c.f. Appendix E). For example, a shoulder melting peak is located at 119 °C for P(3HB-*co*-8mol% 3HHx) isothermally crystallized at 111 °C. All melting peaks increase with increasing isothermal crystallization temperatures. There is no significant variation to the values of ΔH_m as a function of isothermal T_c.

Our observation on multiple melting peaks agrees well to that reported in the literatures. These were observed in homopolymer P(3HB) according to Lee (2008). The first melting peak is due to the melting of crystallites formed during sample preparation (e.g. isothermal crystallization) while the higher peak is due to the melting of crystals formed from recrystallization during heating. Chen and co-workers (2005) reported the occurrence of multiple melting peaks after isothermal crystallization for P(3HB-*co*-15mol% 3HHx) (Chen, Cheung, & Yu, 2005). However, the second melting peak remains almost constant with increasing isothermal crystallization temperature. This could be due to the difference choice of isothermal crystallization temperature. In Chen et al (2005), the isothermal crystallization temperature (T_c = 48-60 °C or ΔT_c = 62-74 °C) is far below melting temperature. In our study, the isothermal crystallization temperature [T_c = 110-116 °C (ΔT_c = 44-50 °C) for P(3HB-*co*-8mol% 3HHx] is near to melting temperature. All other copolymers containing 3 mol% and 12 mol% of 3HHx in this study used similar range of ΔT_c, which is in the range of 55-61 °C and 43-49 °C, respectively. The choice of supercooling temperature ($\Delta T_c = T_m^0 - T_c$) play important role. It is generally recognized that the smaller the undercooling, the lower is the thermodynamic driving force for nucleation and growth. If ΔT_c were high, there is a restriction of molecular mobility near to T_g. Thus, one has to take into account this contribution. More detailed analysis on the melting behavior of P(3HB-*co*-3HHx) is given in Ding and co-workers (2011) (Ding, Cheng, & Wu, 2011) and Hu and co-workers (2007) (Hu, Zhang, Sato, Noda, & Ozaki, 2007).

Quantity T_m^0 are estimated after Hoffman-Weeks method where the melting peaks are plotted against their corresponding isothermal crystallization temperatures. In this study, one sees that P(3HB-*co*-3HHx)s have primarily two obvious melting peaks. The first melting peak corresponds to primary crystallites that are formed during isothermal crystallization. The second melting peak gradually diminishes with increasing isothermal crystallization temperature, which indicates that it is the result of reorganization during recrystallization of less perfect crystal. For this reason, Hoffmann-Weeks (HW) plot (kindly refer Section 2.4.4 for detailed HW approach) utilizes only the first melting peak was adopted in order to obtain reliable T_m^0 values. Detailed calculation for the values of T_m^0 for P(3HB-*co*-3HHx) with different 3HHx contents is shown in Appendix G. The extrapolation of linear experimental T_ms to plot $T_m = T_c$ yields T_m^0 (Section 2.4.4). An example of HW plot for P(3HB-*co*-8mol% 3HHx) is given as follow (Figure 4.14):

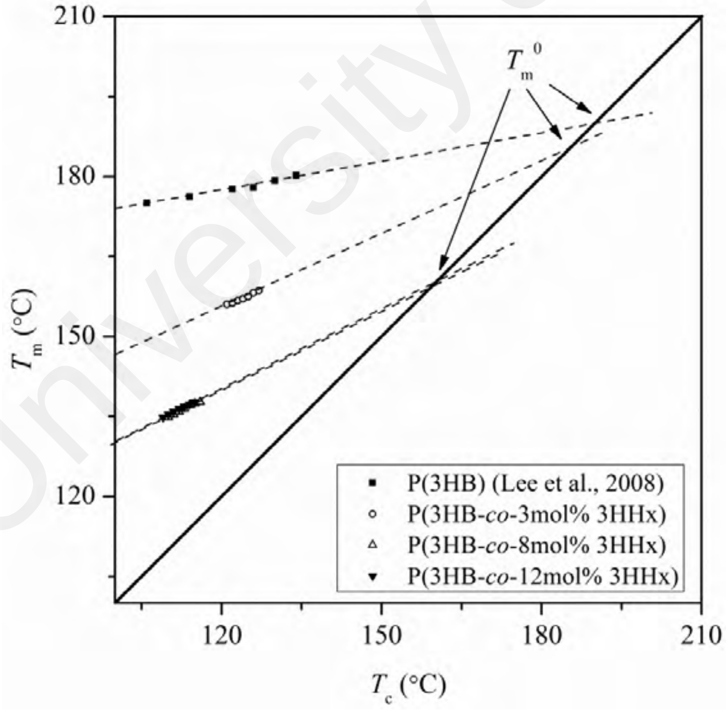

Figure 4.14 An example of HW plot for P(3HB-*co*-3HHx) [P(3HB) as a reference (H. K. Lee, 2008)]

Quantity T_m^0 for different mol% of 3HHx in the copolymer is summarized in Table 4.6. The T_m^0 for P(3HB-*co*-3HHx) containing 3, 8, and 12 mol% of 3HHx is 183 ± 7, 160 ± 8, 158 ± 3 °C, respectively. According to literature, P(3HB) has a T_m^0 of 190 ± 15 °C (Barham et al., 1984; H. K. Lee, 2008). It is shown that increasing the mol% of 3HHx in the copolymer decreases the hypothetical melting of perfect crystals. These values are higher to that reported by Chen et al (2005), with P(3HB-*co*-15mol% 3HHx) having a T_m^0 of 122 °C. Quantity $1/\gamma$ of P(3HB) is lower than that of P(3HB-*co*-3HHx). The constancy of $1/\gamma$ in P(3HB-*co*-3HHx) suggests the entropy change in the amorphous phase of P(3HB-*co*-3HHx) caused by crystallization is not influenced by the commoner content of 3HHx.

Table 4.6 Equilibrium melting point of P(3HB-*co*-3HHx) with different molar fractions of 3HHx

Molar fraction of 3HHx (mol%)	T_c (°C)	T_m^0 (°C)	$1/\gamma$
0[a]	106-134	190 ± 15	0.17
3	121-127	183 ± 7	0.44
8	110-116	160 ± 8	0.50
12	109-115	158 ± 3	0.47
15[b]	48-60	122	-
18[c]	85-100	161 ± 3.6	-

a(H. K. Lee, 2008)
b(Chen et al., 2005)
c(Cai & Qiu, 2009)

4.1.5.3 Crystallinity after isothermal crystallization

The crystallinity (X^*_{iso}) of P(3HB-*co*-3HHx) can be determined by extracting the melting enthalpies (ΔH_{m}s were obtained by integrating all area of all melting peaks) after five $t_{0.5}$s using a linear integration. Quantity X^*_{iso} can be estimated according to Eq. 2.3. Figure 4.15a shows the crystallinity values of P(3HB-*co*-3HHx) as a function of isothermal crystallization temperature. At a glance, the X^*_{iso} of PHA decreases with increasing 3HHx contents. The crystallinities of P(3HB), P(3HB-*co*-3mol% 3HHx), P(3HB-*co*-8mol% 3HHx) and P(3HB-*co*-12mol% 3HHx) were calculated as the average of 62.7 % 42.5 %, 21.0 % and 20.0 %, respectively, with reference to 100% crystalline material of P(3HB). The incorporation of 3 mol% of 3HHx reduces the crystallinity by approximately 10-20% as compared to that of P(3HB), and further decreases the crystallinity when more 3HHx is present in the system (Figure 4.15b).

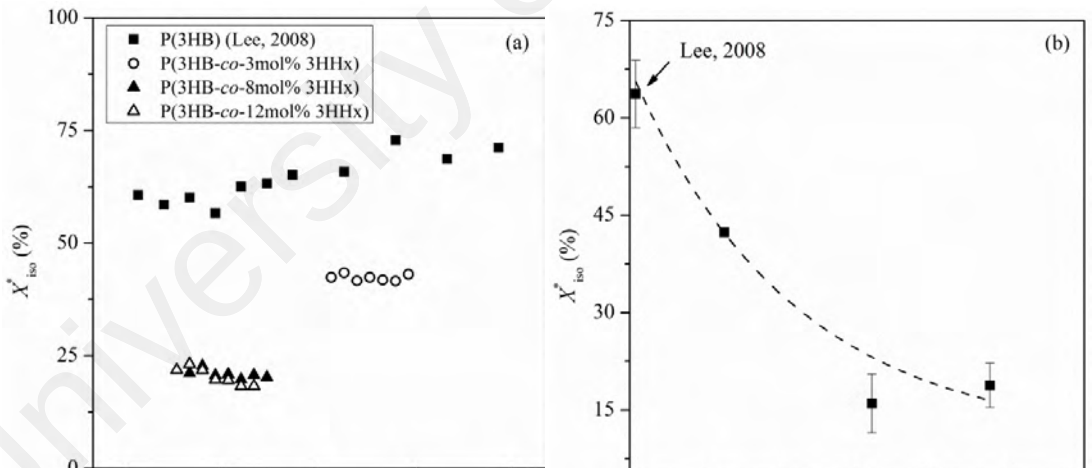

Figure 4.15 Crystallinity of polyhydroxyalkanoates as a function of (a) isothermal crystallization temperature and (b) 3HHx contents [*Note:* X^*_{iso} *in (b) is the average values from (a)*].

4.1.6 Kinetics of isothermal crystallization

Evaluation of isothermal crystallization of PHAs begins from the extraction of area integral of exothermic crystallization peaks as a function of time, as illustrated in Figure 4.16. This figure shows an example of exothermic crystallization curve of P(3HB-*co*-8mol% 3HHx), which was isothermally crystallized at 111 °C. Extrapolation from the end point of crystallization curve (also called as horizontal baseline integration) (J. N. Hay & Mills, 1982) was employed to estimate the half-time of isothermal crystallization. This way of extrapolation was preferred over straight line integration, with higher accuracy of approximately 6% (Salim, Chan, Sudesh, & Gan, 2014).

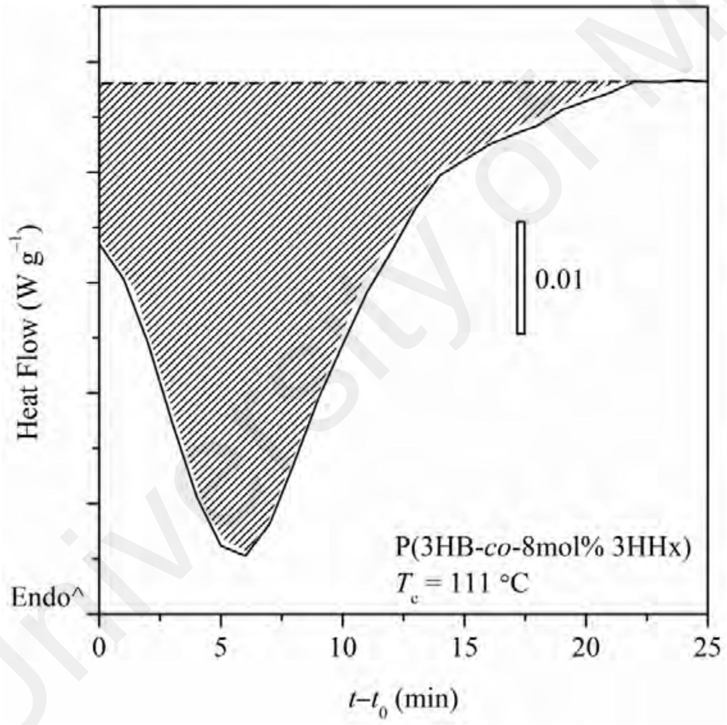

Figure 4.16 Exothermic crystallization curve of P(3HB-*co*-8mol% 3HHx) for isothermal crystallization at T_c = 111 °C analyzed using horizontal baseline integration

Figure 4.17 illustrates the plots of *X*(*t*) *versus* crystallization time (t-t_0), for P(3HB-*co*-8mol% 3HHx) isothermally crystallized at 110-116 °C. The curves exhibit 'sigmoidshape' of isotherms, and shift to longer time with increasing isothermal crystallization temperature. In general, all PHAs containing different mol% of 3HHx show similar pattern of crystallization transformation curves.

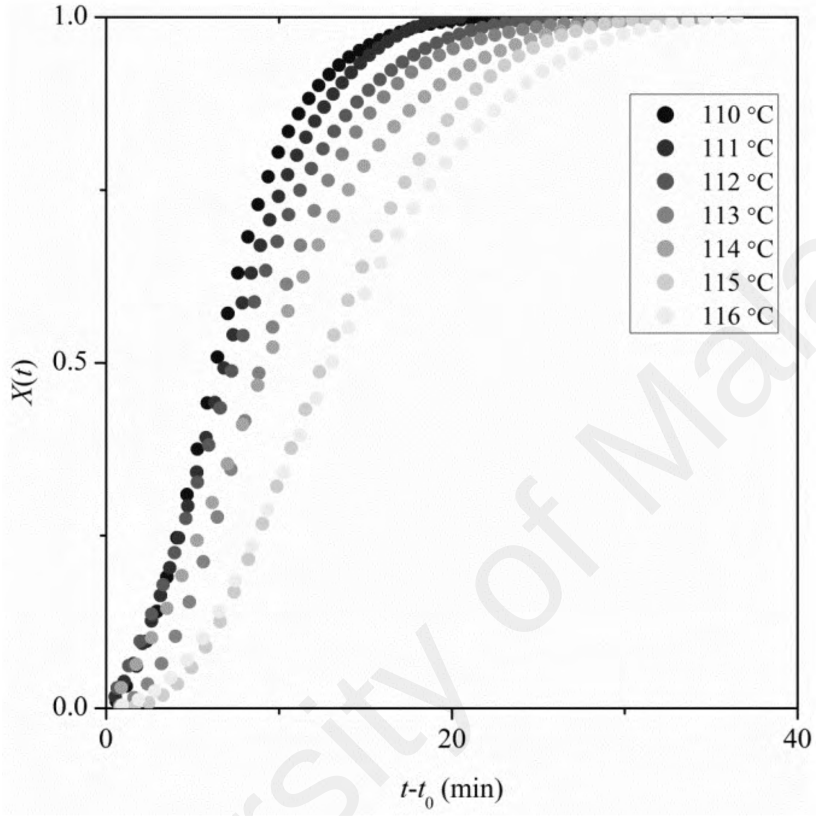

Figure 4.17 Fraction of crystallizable component as a function of isothermal crystallization time for P(3HB-*co*-8mol% 3HHx) [T_c = 110 °C (black) to 116 °C (light grey)]

The fraction of crystallizable component, $X(t)$, is also plotted against reduced time, $\left(\frac{t-t_0}{t_{0.5}}\right)$, to see if the mechanism or feature of isothermal crystallization are of any difference. The curves for neat P(3HB-*co*-3HHx) crystallized at different T_cs, followed by P(3HB-*co*-3HHx) having different mol% of 3HHx coincide reasonable well forming a master curve as shown in Appendix F. This means that the feature of crystallization, e.g.

nucleation and growth, do not change with crystallization temperatures and 3HHx contents.

One of the important parameters used to describe the crystallization kinetics is $t_{0.5}$. The full spectrum of calculated $t_{0.5}$ for different mol% of 3HHx is shown in Figure 4.18. This quantity is obtained from 50% area integration of crystallization peak shown in Figure 4.16. The $t_{0.5}$ increases exponentially with increasing isothermal crystallization temperature. This trend is commonly observed in most semi-crystalline polymers that are isothermally crystallized at low undercooling temperature. The same trend is observed in all P(3HB-*co*-3HHx) having different mol% of 3HHx. At the same isothermal crystallization temperature, it takes longer time for e.g. P(3HB-*co*-12mol% 3HHx) to crystallize as compared to that of P(3HB-*co*-3mol% 3HHx).

Aside from experimental value from 50% area integration, the value of $t_{0.5}$ can also be estimated using Avrami equation (Eq. 2.4) by inserting the value of relative crystallinity at times t equals to 0.5. In this way, the equation becomes $t_{0.5} = (ln\ 2/K)^{1/n}$. One can immediately evaluate if the experimental and calculate values are corresponding well or vice versa. Result shows that the calculated and experimental values of $t_{0.5}$ agree to a good approximation (see Table 4.7).

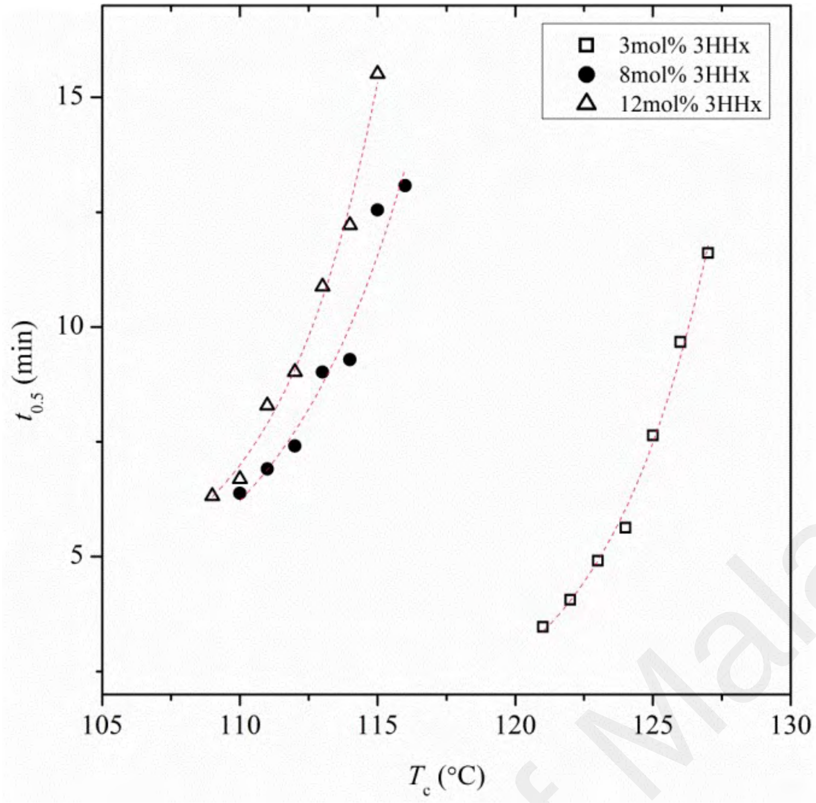

Figure 4.18 Half-time of isothermal crystallization as a function of isothermal crystallization temperature (dashed curves represent exponential peak fitting obtained from OriginPro 8.1)

It is interesting at this point to examine the influence of different types or content of the co-monomer on $K^{1/n}$ values during isothermal crystallization. An example of Avrami plot for P(3HB-*co*-8mol% 3HHx) is shown in Figure 4.19. Although the linearity is not observed over the entire transformation range in P(3HB-*co*-8mol% 3HHx), a very good agreement (r^2 = 0.9986 – 0.9999) to Avrami is found to a certain range of time with up to 50% degree of conversion. This was due to the secondary crystallization that takes place after impingement of spherulites.

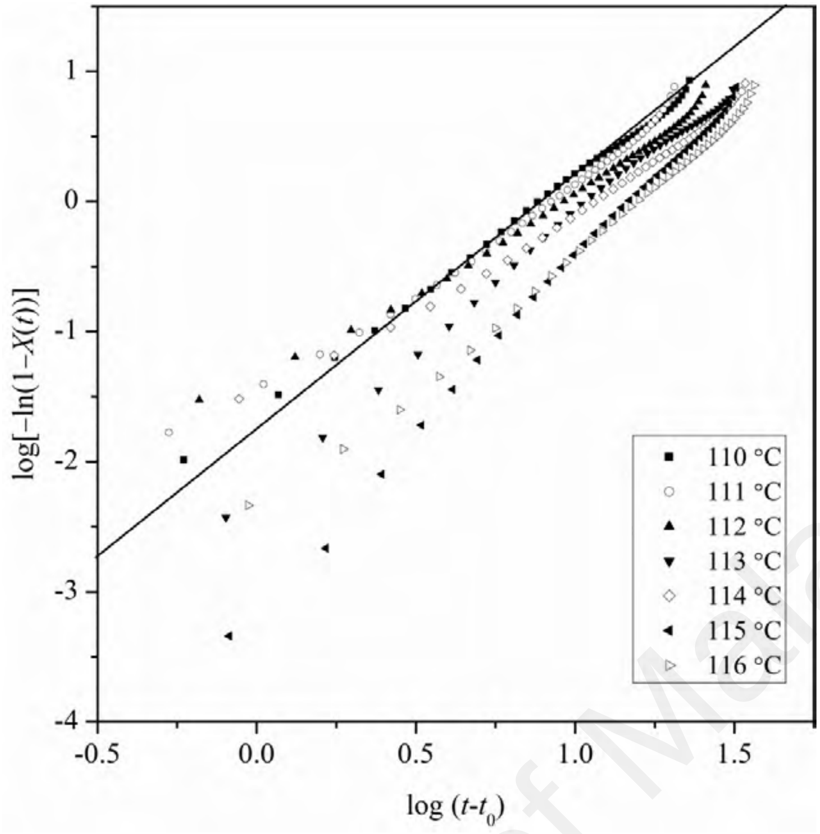

Figure 4.19 Avrami plots of P(3HB-*co*-8mol% 3HHx) at isothermal crystallization temperatures (solid curve represents linear peak fitting obtained from OriginPro 8.1)

A summary of $K^{1/n}$ values for P(3HB-*co*-3HHx) with different mol% of 3HHx is given in Figure 4.20. Generally, it is shown that the rate constant of isothermal crystallization reduces exponentially for P(3HB-*co*-3HHx) with increasing crystallization temperatures. Rate constants of isothermal crystallization reduce with the increment of co-monomer content in PHAs, illustrated by the vertical dash curve in Figure 4.20. The choice of crystallization temperature in our study is located at low undercooling temperature (ΔT_c = 43-61 °C). It is shown that the rate constants reduce at high undercooling for P(3HB-*co*-12mol% 3HV) (ΔT_c = 83 °C) (Chan, Kammer, Sim, & Winie, 2011).

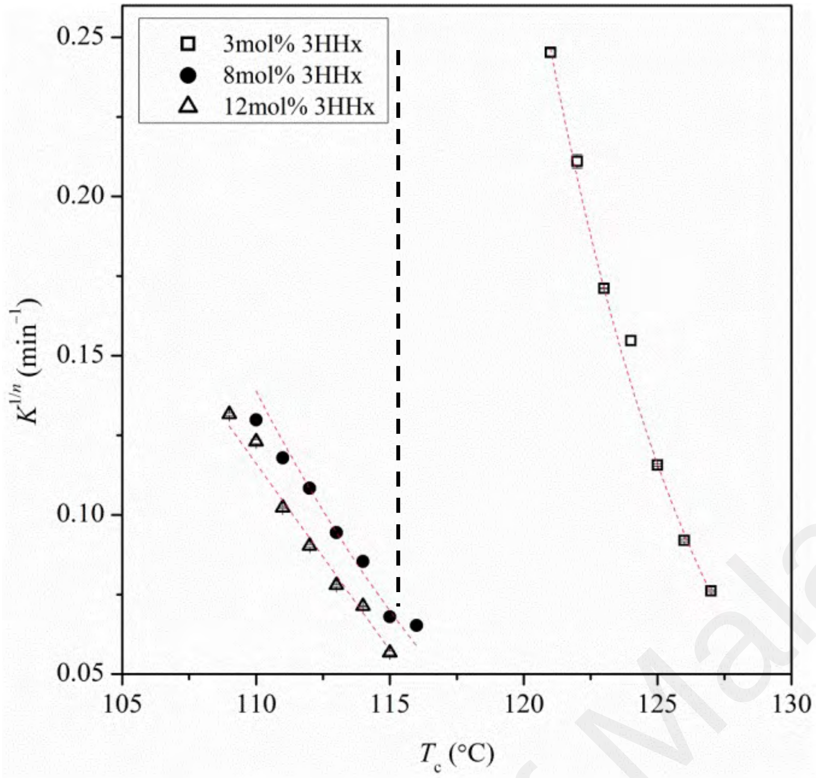

Figure 4.20 Plot of rate constant of isothermal crystallization versus crystallization temperature for P(3HB-*co*-3HHx) (dashed curves represent exponential peak fitting obtained from OriginPro 8.1)

Table 4.7 summarizes the Avrami parameters for the kinetics of crystallization in P(3HB-*co*-3HHx) containing different mol% of 3HHx. P(3HB-*co*-3mol% 3HHx) has average *n* values of 2.8. At higher mol% of 3HHx such as 8 mol% and 12 mol% of 3HHx, *n* values appear to be lower at 2.0 and 2.2, respectively. The higher the isothermal crystallization temperatures, the higher the *n* values. This result correlates well to other published result. For example, within the same molecular weight of P(3HB-*co*-4HB), the average *n* values decrease with increasing mol% of 4HB (Lu et al., 2011). Mandelkern (2004) dictates that *n* value plays a key role in the analysis of overall crystallization kinetics (Mandelkern, 2004). Although in a few cases, the *n* value is affected by the crystallization temperature, the revelation of the crystallization mechanism based on only DSC result remains a challenge. All the *n* values reported in P(3HB-*co*-3HHx) have non-integral values, indicating nature of non-instantaneous nucleation.

Table 4.7 Avrami parameters for the kinetics of crystallization in P(3HB-*co*-3HHx) containing different molar fractions of 3HHx

Molar percentage of 3HHx (mol%)	T_c (°C)	t_0 (min)	$t_{0.5}$ (min)	$t^*_{0.5}$ (min)	T_m (°C)	ΔH_m (J g^{-1})	ΔH_c (J g^{-1})	n	$K^{1/n} \times 10^{-1}$ (min^{-1})	r^2
3	121	1.0	3.47	3.51	156.1	62.2	59.6	2.46 ± 0.04	2.453 ± 0.011	0.9994
	122	1.3	4.06	4.10	156.3	63.7	56.7	2.53 ± 0.06	2.111 ± 0.021	0.9986
	123	1.4	5.18	5.18	156.7	61.1	57.4	2.56 ± 0.12	1.712 ± 0.001	0.9998
	124	2.0	5.63	5.67	157.1	62.2	53.8	2.79 ± 0.05	1.547 ± 0.013	0.9995
	125	1.4	7.64	7.68	157.5	61.3	58.0	3.10 ± 0.05	1.157 ± 0.004	0.9997
	126	1.5	9.67	9.72	158.2	61.0	55.6	3.28 ± 0.04	0.920 ± 0.004	0.9997
	127	2.2	11.60	11.69	158.6	63.2	51.6	3.14 ± 0.04	0.761 ± 0.003	0.9997
8	110	1.0	6.38	6.41	134.9	31.0	25.6	1.99 ± 0.02	1.298 ± 0.002	0.9997
	111	1.0	6.91	6.90	135.3	33.4	30.5	1.78 ± 0.03	1.179 ± 0.006	0.9993
	112	1.8	7.41	7.41	135.9	30.3	22.8	1.67 ± 0.01	1.084 ± 0.001	0.9999
	113	1.7	9.02	9.01	136.5	30.7	16.0	2.27 ± 0.03	0.944 ± 0.005	0.9999
	114	1.3	9.29	9.31	137.2	28.9	18.6	1.59 ± 0.04	0.854 ± 0.010	0.9993
	115	1.8	12.55	12.57	137.4	30.4	16.6	2.34 ± 0.03	0.680 ± 0.001	0.9998
	116	3.3	13.08	12.98	137.7	29.7	17.6	2.21 ± 0.04	0.653 ± 0.008	0.9997
12	109	1.0	6.32	6.37	134.8	32.0	27.5	2.09 ± 0.03	1.316 ± 0.004	0.9996

Table 4.7 continued

Molar percentage of 3HHx (mol%)	T_c (°C)	t_0 (min)	$t_{0.5}$ (min)	$t^*_{0.5}$ (min)	T_m (°C)	ΔH_m (J g^{-1})	ΔH_c (J g^{-1})	n	$K^{1/n} \times 10^{-1}$ (min^{-1})	r^2
	110	0.5	6.69	6.76	135.4	34.0	27.0	1.99 ± 0.08	1.230 ± 0.006	0.9986
	111	0.4	8.29	8.27	136.0	32.0	27.2	2.18 ± 0.03	1.023 ± 0.003	0.9997
	112	1.0	9.02	8.99	136.4	28.9	19.4	1.75 ± 0.03	0.903 ± 0.004	0.9996
	113	1.6	10.88	10.94	136.8	28.7	19.9	2.29 ± 0.03	0.779 ± 0.003	0.9998
	114	2.1	12.22	12.17	137.3	26.8	16.6	2.59 ± 0.01	0.713 ± 0.002	0.9999
	115	1.6	15.51	15.29	137.7	26.8	13.3	2.56 ± 0.05	0.567 ± 0.006	0.9995

$t^*_{0.5}$ is calculated value using $t^*_{0.5} = \left(\frac{\ln 2}{K}\right)^{\frac{1}{n}}$

r^2 = correlation coefficient

4.1.7 Spherulitic growth rate

The rate of growing spherulites was investigated using polarized optical microscope. Growing images were taken and measurement was performed on a single spherulite before the impingement of the spherulites as shown in Figure 4.21. An example of radius of spherulite against time during isothermal crystallization at T_c = 110 °C for P(3HB-*co*-8mol% 3HHx) is shown in Figure 4.22. Based on this figure, one sees easily a linear correlation between the diameters of spherulites as a function of time. The slope of this curve represents radial growth rate (in μm s^{-1}). All other copolymer containing different mol% of 3HHx behaves in similar pattern but with different values of slope. Detailed radii measurement was summarized in Appendix H.

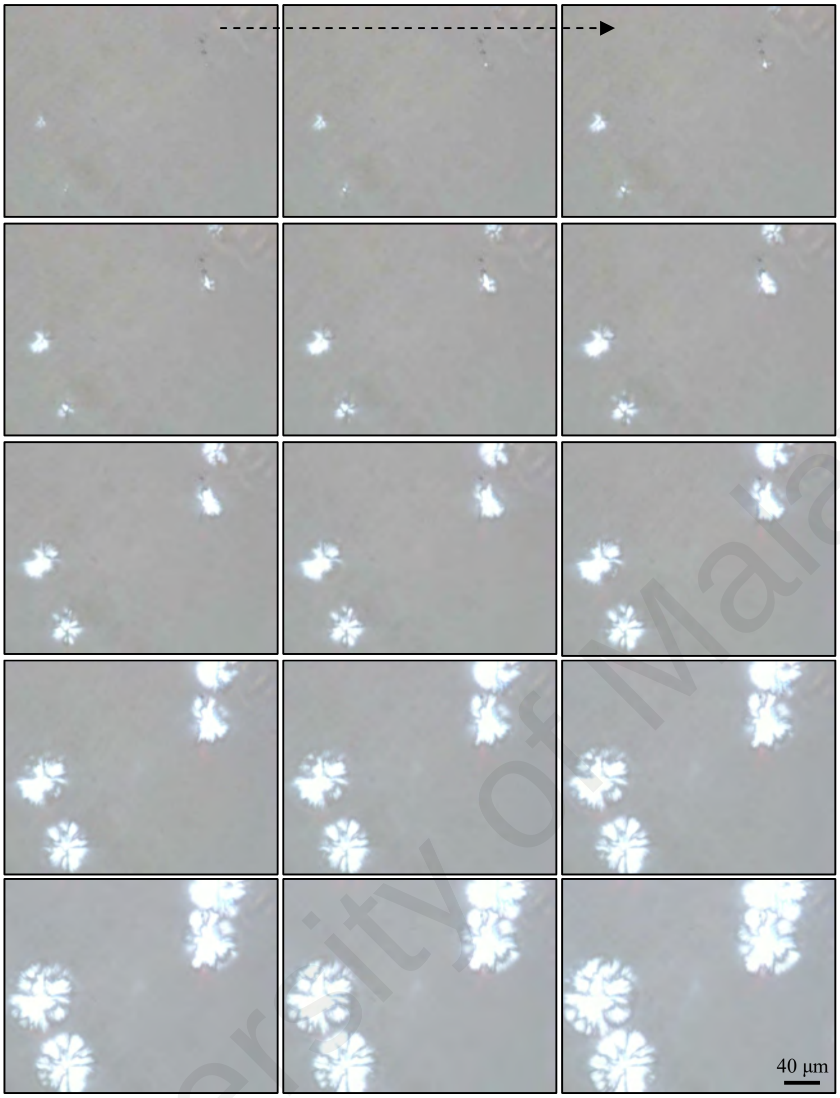

Figure 4.21 Micrographs captured after 5 min growing of P(3HB-*co*-8mol% 3HHx) spherulites at T_c = 110 °C at 60 s time interval every micrograph. Magnification 50×

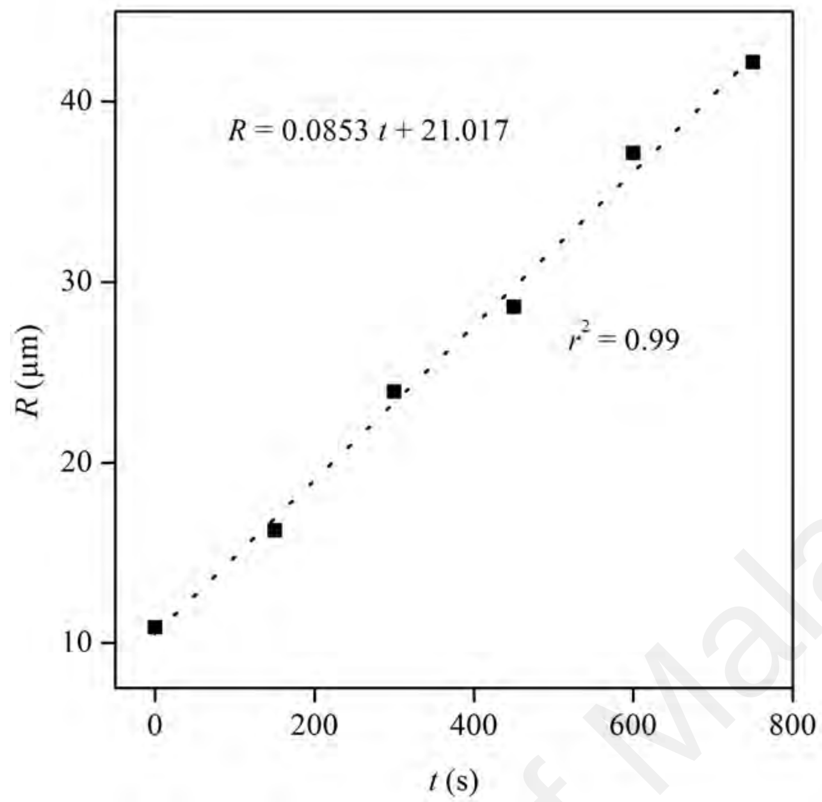

Figure 4.22 Radii of growing spherulites of P(3HB-*co*-8mol% 3HHx) isothermally crystallized at T_c 110°C (dotted curve represents linear growth rate fitted using OriginPro 8.1)

For each isothermal crystallization temperature, one slope is obtained [i.e. the radial growth rate of P(3HB-*co*-3HHx) spherulites]. Figure 4.23 illustrates the changes of G as a function of isothermal T_c for P(3HB-*co*-8mol% 3HHx). Obviously with increasing isothermal crystallization temperature, the growth rate decreases exponentially. For example, at T_c = 110 °C, the spherulite grows at a rate of 5.1 μm min^{-1} for P(3HB-*co*-8mol% 3HHx). While at T_c = 120 °C, the spherulite grows at a rate of 1.1 μm min^{-1} for the same co-polymer. Spherulitic growth rate behaves similarly to that of the constant rate of isothermal crystallization (c.f. Figure 4.20). As outlined in earlier text, when the crystallization temperature is close to its melting temperature, it takes longer time to crystallize.

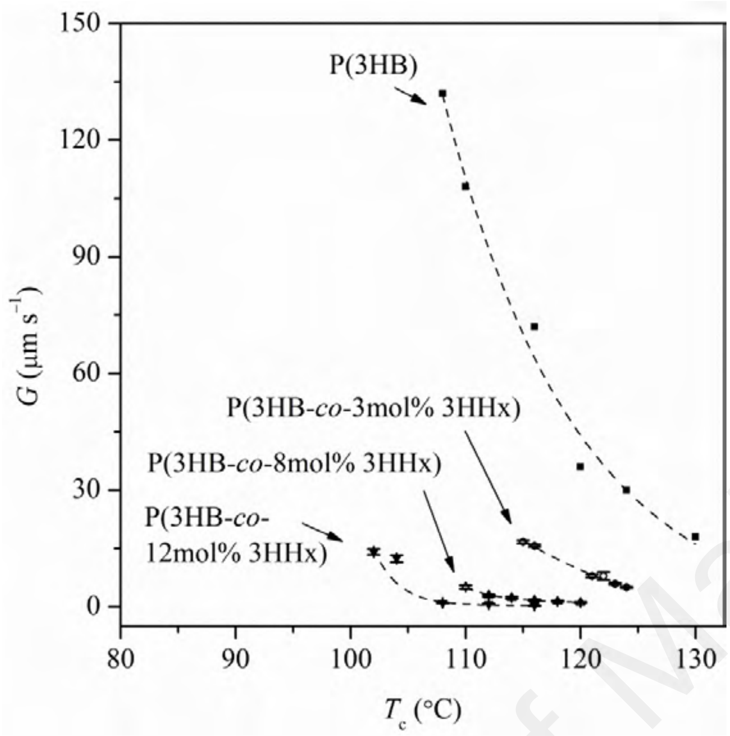

Figure 4.23 Plot of *G* as a function of isothermal T_c for P(3HB-*co*-3HHx) with different 3HHx contents (dotted curves represent decreased exponential growth rate fitted using OriginPro 8.1). P(3HB) as a reference polymer (H. K. Lee, 2008).

Table 4.8 summarizes the quantity *G* for P(3HB-*co*-3HHx) with different mol% of 3HHx. At the same T_c, e.g. 116 °C, *G* decreases with increasing mol% of 3HHx. For example, the quantity *G* for P(3HB-*co*-3mol% 3HHx) is 15.7 µm min^{-1}. By increasing the mol% of 3HHx to 8 mol%, *G* decreases approximately one order of magnitude to 1.7 µm min^{-1}, and subsequently to 0.3 µm min^{-1} when 12 mol% of 3HHx presents.

Table 4.8 Quantity G for P(3HB-*co*-3HHx) with different mol% of 3HHx

0 mol% of 3HHx[*]		**3 mol% of 3HHx**		**8 mol% of 3HHx**		**12 mol% of 3HHx**	
T_c (°C)	G (μm min^{-1})	T_c (°C)	G (μm min^{-1})	T_c (°C)	G (μm min^{-1})	T_c (°C)	G (μm min^{-1})
108	132	115	16.7 ± 0.4	110	5.12 ± 0.48	100	-
110	108	116	15.7 ± 0.3	112	2.87 ± 0.29	102	14.14 ± 0.65
116	72	121	7.88 ± 0.43	114	2.31 ± 0.26	104	12.40 ± 0.89
120	36	122	7.91 ± 1.03	116	1.65 ± 0.21	108	0.95 ± 0.08
124	30	123	5.91 ± 0.20	118	1.41 ± 0.17	112	0.65 ± 0.10
130	18	124	5.04 ± 0.15	120	1.11 ± 0.11	116	0.26 ± 0.08

[*] (H. K. Lee, 2008)

4.1.8 Temperature dependence of rate of isothermal crystallization

The Arrhenius activation energy of isothermal crystallization associated to the overall process of crystallization of P(3HB-*co*-3HHx) can be expressed in terms of Arrhenius-like relationship (Eq. 2.11) using DSC. Quantity $lg(t_{0.5}^{-1})$ is plotted against the reciprocal undercooling temperature (ΔT_c^{-1}) for P(3HB-*co*-3HHx) with different 3HHx contents, as illustrated in Figure 4.24. From our data, it is shown that the average of $\Delta T_c/T_m^0$ is almost constant, therefore the activation energy for P(3HB-*co*-3HHx) containing 3, 8 and 12 mol% 3HHx is calculated to be 3.9, 1.7, and 1.9 kJ mol^{-1}, respectively. By employing the data from Kai and co-workers (2005) (Kai, He, & Inoue, 2005), followed by Chen and co-workers (2005) (Chen et al., 2005) to Arrhenius approach, the calculated activation energy of P(3HB) and P(3HB-*co*-15mol% 3HHx) are found to be 4.2 and 0.5 kJ mol^{-1}, respectively. Further data analysis obtained by Cai and Qiu (2009) (Cai & Qiu, 2009) suggests that the activation energy of P(3HB-*co*-7mol% 3HHx), P(3HB-*co*-10mol% 3HHx) and P(3HB-*co*-18mol% 3HHx) is 1.3 kJ mol^{-1}, 1.1 kJ mol^{-1}, and 0.6 kJ mol^{-1}, respectively. The increase of content of the flexible side chains along the backbone in the PHA reduces the activation energy, which is responsible for the energy required to crystallize. All the activation energies of isothermal crystallization are summarized in Table 4.9.

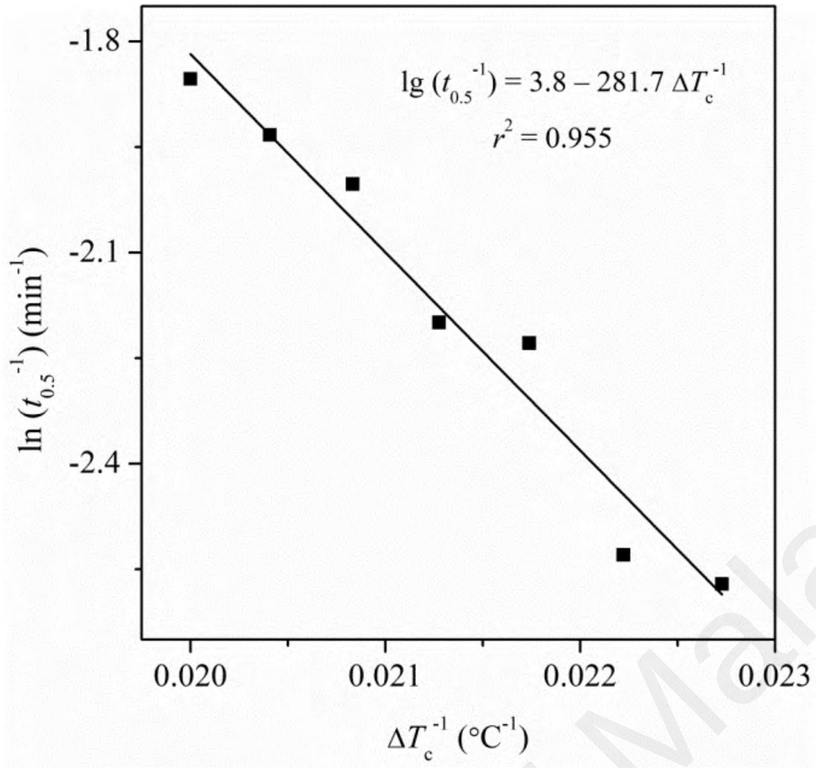

Figure 4.24 Plot of *lg*($t_{0.5}^{-1}$) *versus* ΔT_c^{-1} of P(3HB-*co*-8mol% 3HHx)

Table 4.9 Summary of activation energy during isothermal crystallization of P(3HB-*co*-*x*-mol% 3HHx)

x	Arrhenius' activation energy $B^{*}R$ (kJ mol^{-1})	Comment
0	4.2	(Kai et al., 2005). T_m^0 = 200 °C according to Barham and co-workers 1984 (Barham et al., 1984).
3	3.9	This study
7	1.3	Cai and Qiu (2009)
8	1.7	This study
10	1.1	Cai and Qiu (2009)
12	1.9	This study
15	0.5	Chen et al. (2005)
18	0.6	Cai and Qiu (2009)

4.1.9 Morphology

The morphology of P(3HB-*co*-3HHx) as prepared sample and after isothermal crystallization are shown in Figure 4.25. The sub-Figure '1', '2' and '3' represents micrographs for P(3HB-*co*-3mol% 3HHx), P(3HB-*co*-8mol% 3HHx), and P(3HB-*co*-12mol% 3HHx); while 'a' and 'b' illustrates as-prepared and fully-impinged spherulites after isothermal crystallization at T_c = 115, 118 and 102 °C in P(3HB-*co*-3mol% 3HHx), P(3HB-*co*-8mol% 3HHx), and P(3HB-*co*-12mol% 3HHx) respectively, for 5 × $t_{0.5}$. In all cases of P(3HB-*co*-3HHx) before isothermal crystallization (as-prepared sample), there are some de-wetting of polymer on the glass surface. It can be seen from the ‘bubble’ mark in sub-figure ‘a’. Fully-impinged crystals of P(3HB-*co*-3mol% 3HHx) show relatively large crystals (see magnification in Figure 4.25) with Maltese-cross shape. In co-polymers containing 8 mol% and 12 mol% of 3HHx, there is more nucleation sites that results in more spherulites. The morphologies of these two co-polymers are different to that of P(3HB-*co*-3mol% 3HHx). In P(3HB-*co*-8mol% 3HHx), one sees Maltese-cross but with a more disturbed orientation. In P(3HB-*co*-12mol% 3HHx), it forms spherulites with a concentric extinction ring (or bands). It should be noted that the morphologies of each co-polymer do no vary with variation of isothermal T_c.

The spherulites of P(3HB-*co*-3mol% 3HHx) is similar to that of reported by Barham and co-workers (1984) when P(3HB) is isothermally crystallized at T_c = 100 °C (Barham et al., 1984). Since the co-polymer contains only 3 mol% of 3HHx, it behaves similarly to P(3HB). The morphology of P(3HB-*co*-3HHx) containing higher 3HHx content is also similar to the reported literature. For instance, Xu and co-workers (2004) demonstrated through a real-time atomic force microscope that the banded spherulites in P(3HB-*co*-17mol% 3HHx) exhibit complicated growth behaviors such as twisting, bending, backward growth, and branching. The twisting and bending however reduces when isothermal T_c increases. The origin of banding in spherulites was under debate (Xu et al., 2004).

The understanding of spherulitic morphology is important to understand its influence on final mechanical properties. In many cases, one adds nucleating agents such as uracil (Pan, Liang, Nakamura, Miyagawa, & Inoue, 2009), cyanuric acid (Weng & Qiu, 2014), cyclodextrin-complex (Dong, Mori, Aoyama, & Inoue, 2010) to obtain many nucleation sites with small spherulites. Bigger spherulites tend to derive brittleness in semi-crystalline polymer.

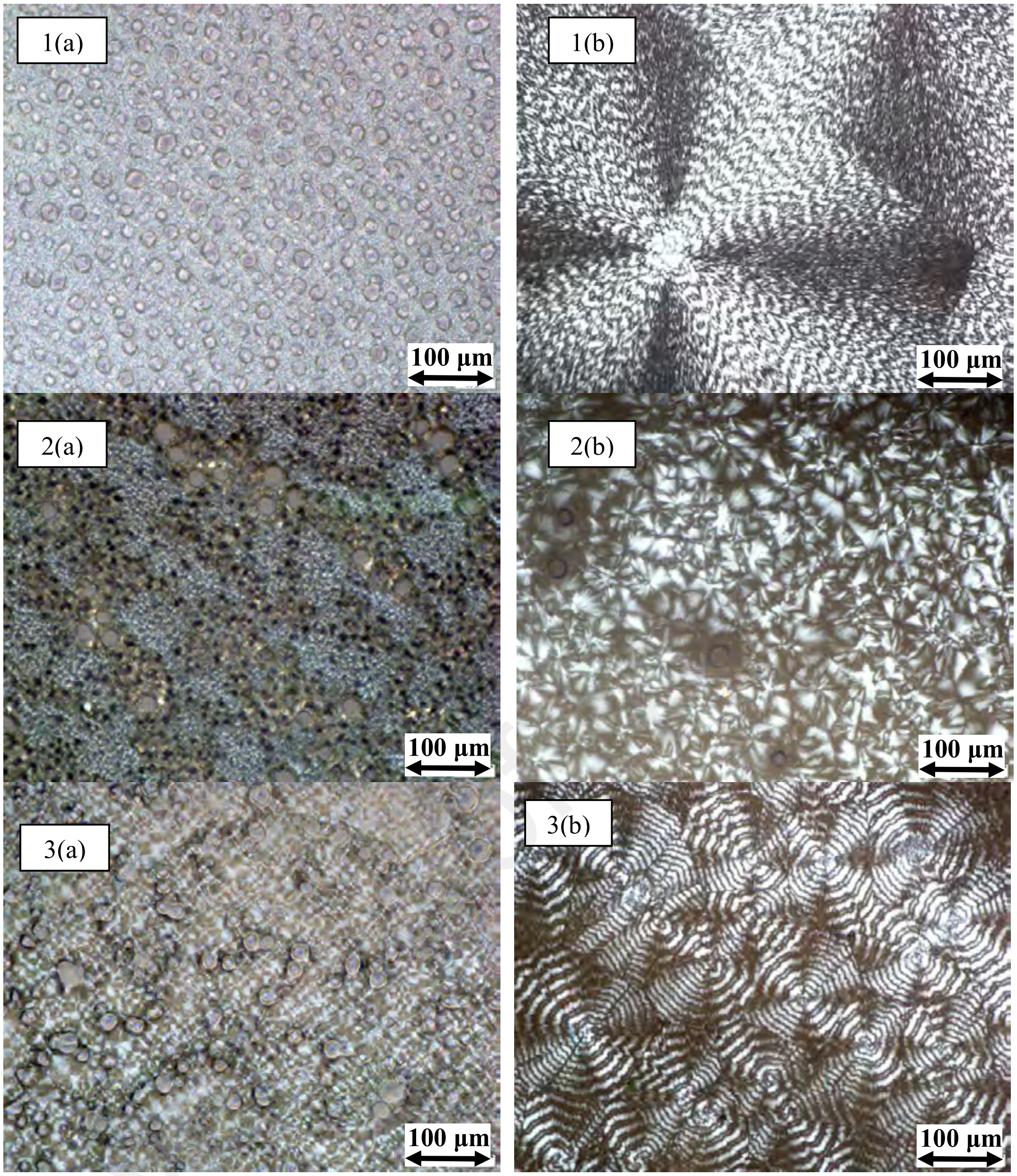

Figure 4.25 (a) as prepared and (b) volume-filled spherulites of P(3HB-*co*-3HHx) [(1): 3 mol% 3HHx at T_c = 115 °C, (2): 8 mol% 3HHx at T_c = 118 °C, and (3): 12 mol% 3HHx at T_c = 102 °C]. The micrographs were taken after 120 – 150 min of isothermal crystallization.

The thermal properties of P(3HB-*co*-3HHx) containing different mol% of 3HHx was discussed in previous sections. In the next section, we adopted only P(3HB-*co*-3HHx) containing 8 mol% of 3HHx to be blended with ENR-50. The choice of P(3HB-*co*-8mol% 3HHx) over two other co-polymers containing 3 mol% and 12 mol% of 3HHx was made to justify the effect of ENR-50 to thermal properties of P(3HB-*co*-3HHx) in the presence of low 3HHx content. On another hand, ENR-50 was chosen over ENR-25 because it provides more epoxide groups. These groups act as active sites for the melt reaction between P(3HB-*co*-8mol% 3HHx) and ENR.

4.2 P(3HB-*co*-8mol% 3HHx)/ENR blends

In this section, P(3HB-*co*-8mol% 3HHx)/ENR blend is sometimes referred as P(3HB-*co*-3HHx)-*blend*-ENR. For each composition, for instance 90:10 (wt%) blend ratio of P(3HB-*co*-3HHx) and ENR, it is referred as w_{ENR} = 0.1 (w_{ENR} = weight fraction of ENR). The blend films were prepared by solution casting, dried and used as it is. All samples are cut vertically to the films prior to analysis. The study of blends was limited only to P(3HB-*co*-3HHx) containing 8 mol% 3HHx. The choice was made based on two considerations: (1) the physical properties of P(3HB-*co*-3HHx) containing 3 mol% 3HHx closely resembles that of P(3HB), and (2) P(3HB-*co*-3HHx) containing 12 mol% 3HHx has lower crystallization rate.

4.2.1 Miscibility

4.2.1.1 T_g

Figure 4.26 shows the T_g of P(3HB-*co*-3HHx)-*blend*-ENR investigated by mean of DSC analysis. Similarly to previous analysis, the T_g is defined as the midpoint of half extrapolated tangents between onset and end (½ × ΔC_p). P(3HB-*co*-8mol% 3HHx) has a T_g located at 0 °C. When ENR is introduced, the T_g of P(3HB-*co*-8mol% 3HHx) remains almost constant, and *vice versa*. There are two T_gs correspond to each component, which strongly indicates immiscibility between P(3HB-*co*-8mol% 3HHx) and ENR.

A close observation reveals that the T_g of P(3HB-*co*-3HHx) reduces to a small extent with addition of ENR. This could be initiated by a small migration of ENR chain into the intra-spherulitic region of P(3HB-*co*-3HHx). Likewise, the T_g of ENR increases slightly with increasing P(3HB-*co*-3HHx) content. Based on these observations, one could see easily that the molecular chain of P(3HB-*co*-3HHx) is influenced when ENR is present, and *vice versa*. It was reported by Wondraczek and co-workers (2004) that T_g has a good correlation to its activation energy during thermal decomposition (Wondraczek, Adams, & Fuhrmann, 2004). This point will be discussed in later analysis.

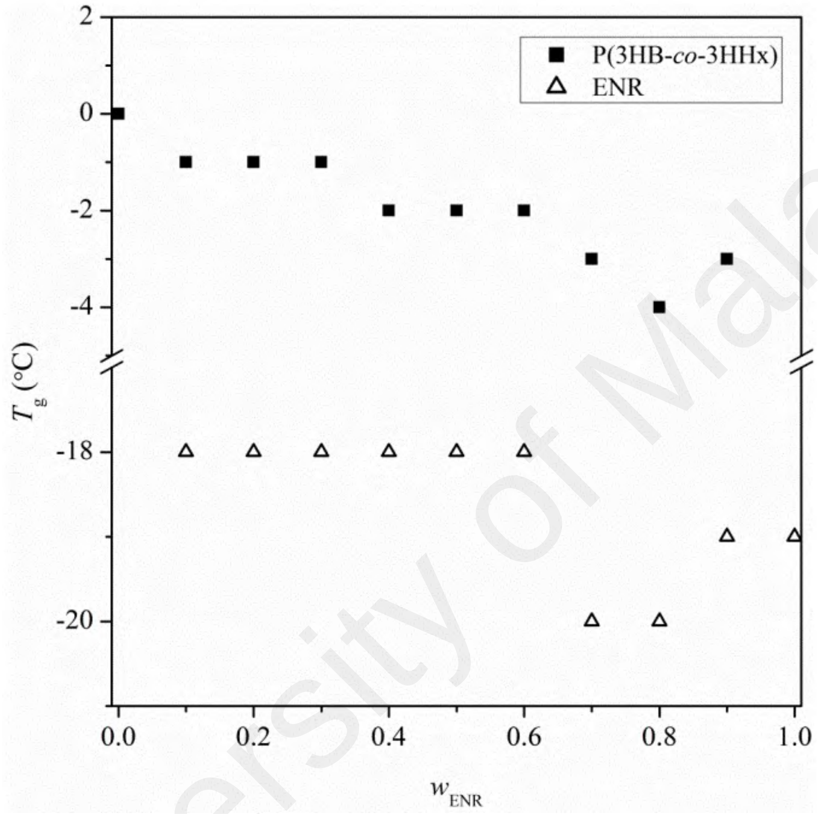

Figure 4.26 Glass transition temperature of P(3HB-*co*-3HHx)-*blend*-ENR

The ΔC_p are also evaluated after addition of ENR into P(3HB-*co*-8mol% 3HHx) (c.f. Figure 4.27). Quantity ΔC_p of P(3HB-*co*-8mol% 3HHx) decreases monotonously with increasing w_{ENR}, and *vice versa*. It can be appreciated that P(3HB-*co*-8mol% 3HHx) and ENR blends are immiscible. The ΔC_p of neat P(3HB-*co*-8mol% 3HHx) is 0.47 J (g °C)$^{-1}$ and neat ENR is 0.54 J (g °C)$^{-1}$.

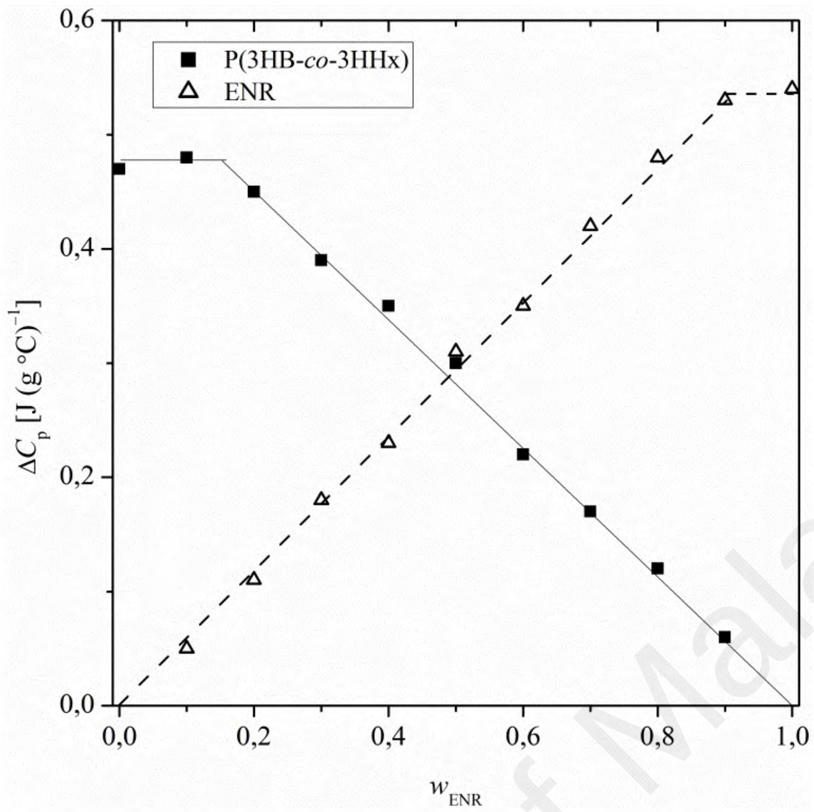

Figure 4.27 Changes in heat capacity of P(3HB-*co*-3HHx)-*blend*-ENR [solid line refers to P(3HB-*co*-8mol% 3HHx) and dashed line refers to ENR]

4.2.1.2 Melting temperature

Figure 4.28 shows the melting profiles of heat-cool-heat P(3HB-*co*-3HHx)-*blend*-ENR as a function of w_{ENR}. Pure P(3HB-*co*-3HHx) has two T_{m}s located at (I) 120 °C and (II) 138 °C. As pointed out earlier, bacterial copolymers are known to exhibit multiple melting temperatures (Ding et al., 2011; Hu et al., 2007; Ye et al., 2010). When ENR is added, there is an appearance crystallization peak right after the first melting at 125 °C (as indicated by letter '*c*' in Figure 4.28), and these crystallites melt after the second melting peak (as indicated by letter '*m*' in Figure 4.28) at T_{m} = 142 °C. The origin of new crystallization and melting peak is suggested to be a result nucleating effect of ENR in liquid P(3HB-*co*-3HHx) phase. This means that in the beginning, the molten process of P(3HB-*co*-3HHx) starts at the boundary of spherulites and part of the crystalline phase are now in free motion. The free movable P(3HB-*co*-3HHx) chains crystallize immediately when ENR chain comes close to them. This new crystalline phase may or may not have different form as compared to that of the crystalline phase of pure P(3HB-*co*-3HHx).

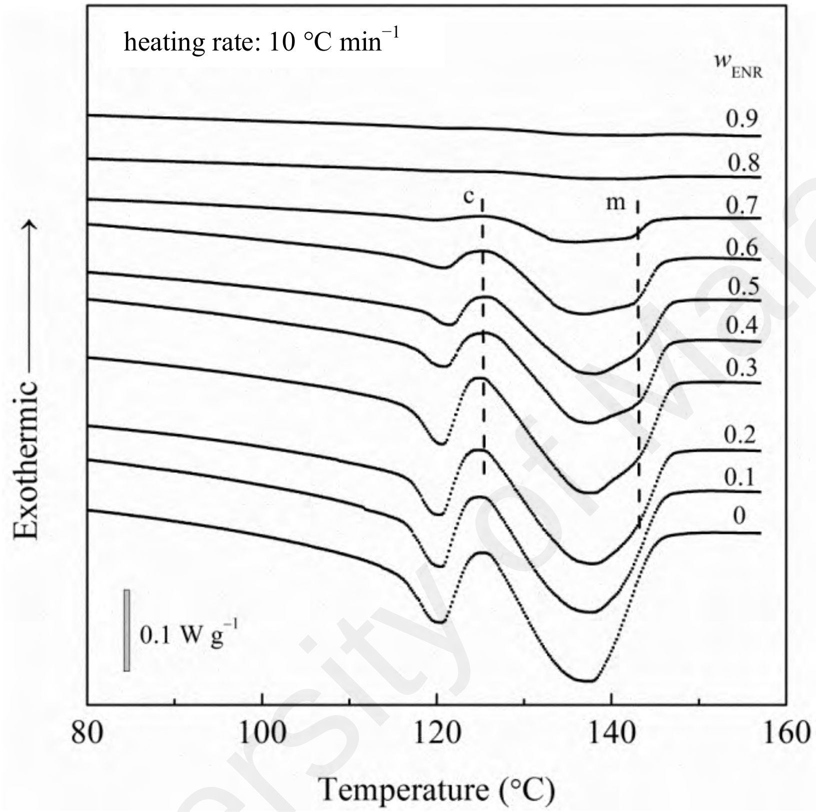

Figure 4.28 Endothermic melting peak of P(3HB-*co*-3HHx) in P(3HB-*co*-3HHx)-*blend*-ENR. From bottom to top: neat P(3HB-*co*-8mol% 3HHx), blends from 10 wt%-90wt%, and ENR.

Melting profile of P(3HB-*co*-3HHx)-*blend*-ENR after isothermal crystallization is shown in Figure 4.29. P(3HB-*co*-3HHx) exhibits four melting peaks (I, a, II, and III) after isothermal crystallization. The melting peak I at 120 °C does not shift with addition of ENR. This peak (also called as annealing peak) was reported as the melting of secondary lamellae (Xu et al., 2004). The T_{m} (a) shifts to lower temperature with increasing ENR content and conversely, T_m (II) and T_m (III) shift to higher temperature with increasing ENR. Note that T_m (II) is the primary lamellae formed during isothermal crystallization, and T_m (III) is the melting of lamellae formed through re-crystallization at ~140 °C. The magnitude of T_m (III) is larger when the re-crystallization is obvious. It is interesting to point out that when w_{ENR} increases, there is more re-crystallization in P(3HB-*co*-8mol% 3HHx). From the area integration of melting endotherms shown in Figure 4.29, the influence of ENR to the crystallinity of P(3HB-*co*-8mol% 3HHx) after isothermal crystallization (X^*_{iso}) can be determined. Two examples of area integration by horizontal baseline are shown in the same figure, e.g. w_{ENR} = 0 and 0.5. Two methods of baseline integration (flat and horizontal) have been discussed by Salim and co-workers (2014) (Salim et al., 2014). The horizontal baseline integration seems to be more accurate in reducing the error of integration by 6%. The choice of area integration includes melting peak (III) because this peak is responsible for the melting of lamella formed through re-crystallization (indicated by arrow). It should be noted that during area of integration, the recrystallization peak was deducted from the total area of melting.

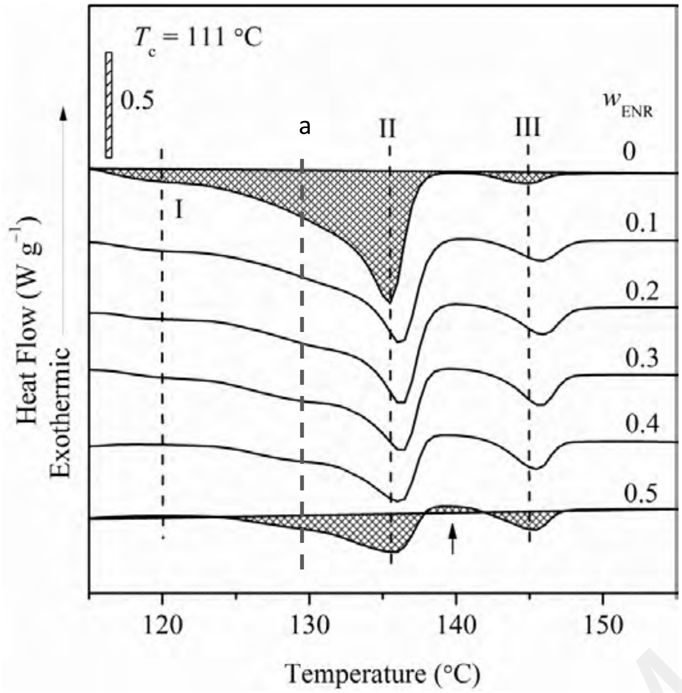

Figure 4.29 Melting profile of P(3HB-*co*-3HHx) in P(3HB-*co*-3HHx)-*blend*-ENR after isothermal crystallization (dashed curve is for visual aid) at T_c = 111 °C

Since T_m (II) corresponds to the melting of primary crystallites formed during isothermal crystallization, it is then used to determine T_m^0 (H-W approach). Table 4.10 summarizes the T_m^0 obtained with variation of w_{ENR}. The melting temperature of hypothetical perfect crystal for P(3HB-*co*-3HHx) in the blend do not change with addition of ENR. Similarly to its neat copolymer of P(3HB-*co*-3HHx), parameter $1/\gamma$ is almost constant with respect to w_{ENR}. This suggests that the entropy change in the amorphous phase of P(3HB-*co*-3HHx) caused by the crystallization is also not influenced by the ENR content.

Table 4.10 Equilibrium melting temperature of P(3HB-*co*-3HHx)-*blend*-ENR

w_{ENR}	0	0.1	0.2	0.3	0.4	0.5
T_m^0 (°C)	160 ± 44	160 ± 12	161 ± 15	159 ± 11	157 ± 12	157 ± 11
$1/\gamma$	0.50 ± 0.08	0.49 ± 0.04	0.49 ± 0.05	0.48 ± 0.04	0.46 ± 0.04	0.45 ± 0.04

4.2.2 Thermal stability

Figure 4.30 shows the TGA thermal decomposition profile of P(3HB-*co*-8mol% 3HHx)/ENR blends from 100 °C to 500 °C. Both neat polymers, P(3HB-*co*-8mol% 3HHx) and ENR, show one step decomposition process, with onset temperature at 240 °C and 360 °C and 100% weight loss at 500 °C, respectively. The decomposition of blends proceeds in two steps, which corresponds to each component. The thermal decomposition temperatures reported in this study are similar to that of other literatures (Asrar et al., 2002; Nakason, Tobprakhon, & Kaesaman, 2005).

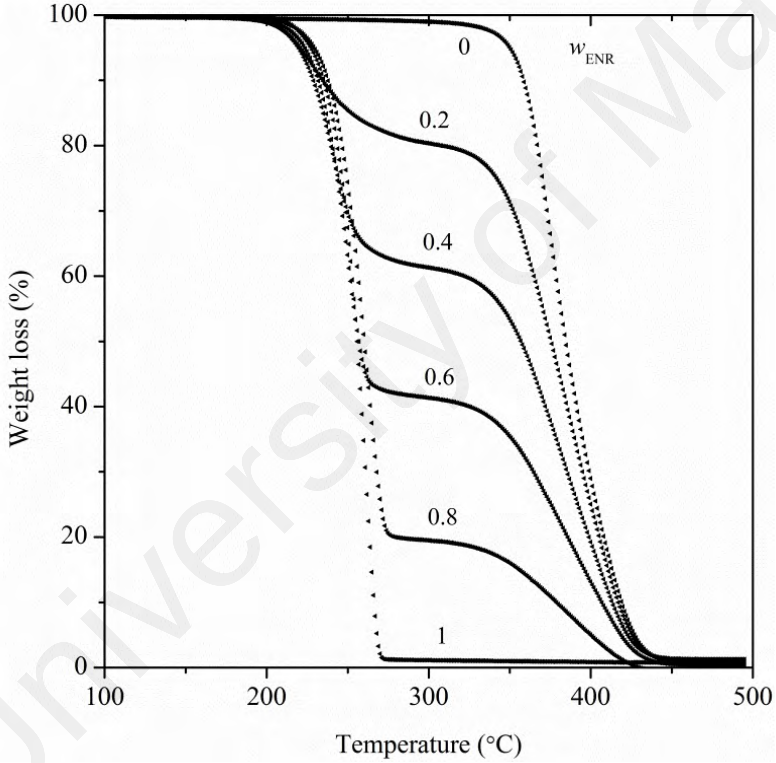

Figure 4.30 TGA profile of P(3HB-*co*-8mol% 3HHx)/ENR blends (from top to bottom: w_{ENR} = 0, 0.2, 0.4, 0.6, 0.8, and 1)

When the experimental weight loss of one component, e.g. ENR, is plotted against its nominal value, one could easily evaluate the blends distribution (c.f. Figure 4.31). Here, it shows the precision of blends distribution. That means if the nominal value of w_{ENR} is equal to 0.2, the experimental value of w_{ENR} during analyses is also 0.2. The activation energy of TGA blends will be discussed later during the discussion of melt reaction.

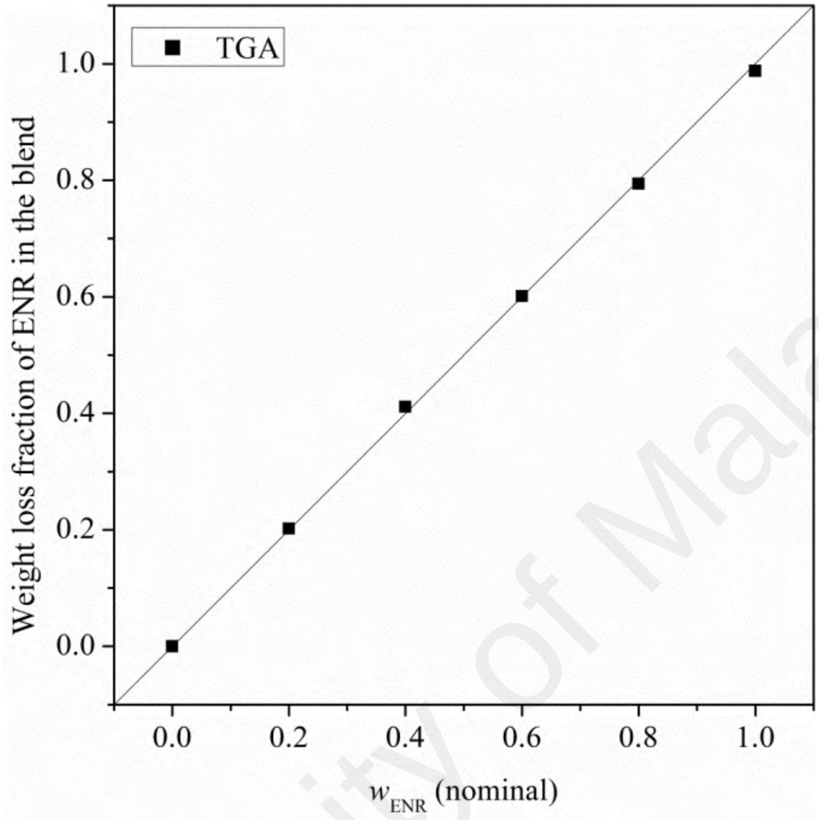

Figure 4.31 Plot of experimental weight loss fraction of ENR in the blend against nominal weight fraction of ENR

4.2.3 Crystallinity

The effect of ENR to crystallization and melting behavior of P(3HB-*co*-3HHx) was also investigated. Information related to crystallization and melting quantities are summarized in Table 4.11. The normalized crystallinity (X^*) was calculated from the Eq. 2.2. From heat-cool-heat experiment, results show that pure P(3HB-*co*-8mol% 3HHx) has a crystallinity of 7%. In the blends, the X^* of P(3HB-*co*-3HHx) is constant below 80wt% of ENR. At and above 80wt% of ENR, the blend was almost amorphous

(X^* ≈ 2%). This is due to the crystallization inhibition of ENR towards P(3HB-*co*-3HHx).

Table 4.11 Summary of crystallization and melting quantities of P(3HB-*co*-3HHx) in P(3HB-*co*-3HHx)-*blend*-ENR after heat-cool-heat; and T_g and ΔC_p of the blends

w_{ENR}	T_g^1 (ΔC_p) °C [J (g °C)$^{-1}$]	T_g^2 (ΔC_p) °C [J (g °C)$^{-1}$]	Sum of ΔC_p^3 [J (g °C)$^{-1}$]	ΔH_m^4 (J g^{-1})	ΔH_c (J g^{-1})	X^* (%)
0	-	0 (0.47)	0.5	49.9	39.3	7
0.2	−18 (0.11)	−1 (0.45)	0.6	37.9	31.2	6
0.4	−18 (0.22)	−2 (0.37)	0.6	25.4	21.8	6
0.6	−18 (0.36)	−2 (0.27)	0.6	17.2	13.3	7
0.8	−19 (0.49)	−3 (0.10)	0.6	1.2	0.7	2
1	−19 (0.58)	-	0.6	-	-	-

[1] ENR
[2] P(3HB-*co*-3HHx)
[3] Sum = $\Delta C_{p,\,T_{g1}} + \Delta C_{p,\,T_{g2}}$
[4] This quantity was extracted from area of integration from the melting peaks shown in Figure 4.28

The average values of X^*_{iso} of P(3HB-*co*-3HHx) under influence of ENR was also calculated (c.f. Figure 4.32) after isothermal crystallization at T_c = 110 – 117 °C according to Eq. (2.3). The melting enthalpies were obtained by integrating the melting endotherms shown and discussed in Figure 4.29. It is shown that the quantity X^*_{iso} decreases slightly to a small approximation when ENR weigh ratio increases up to 0.8 in the blend. This simply means that P(3HB-*co*-8mol% 3HHx) and ENR are immiscible, and the crystallinity of P(3HB-*co*-8mol% 3HHx) is somehow unaffected by the ENR content when P(3HB-*co*-3HHx) is in excess.

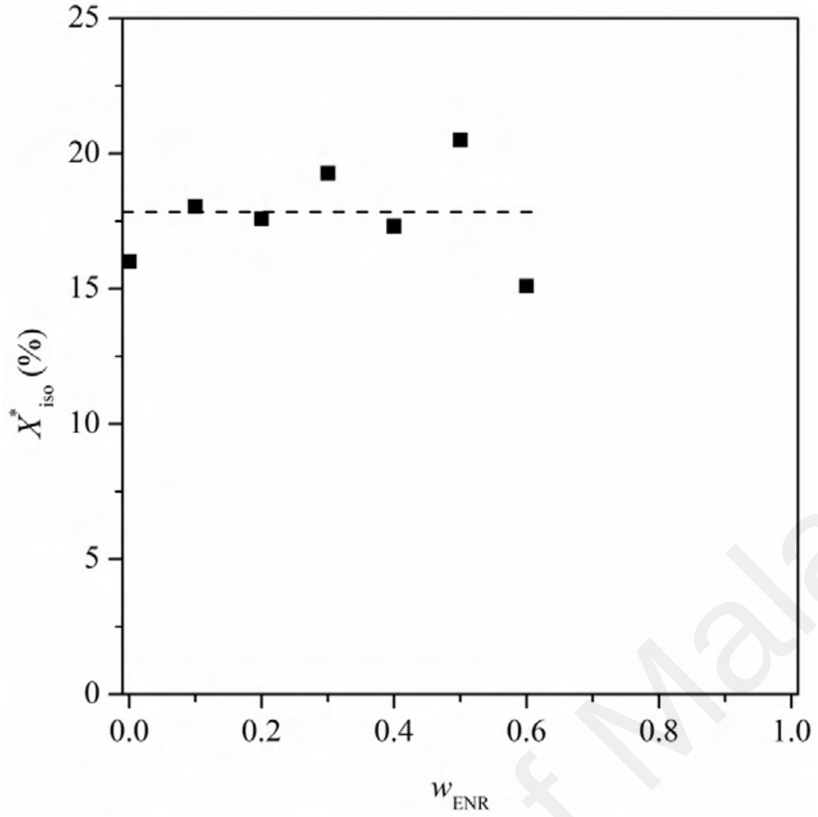

Figure 4.32 Average values of crystallinity of P(3HB-*co*-3HHx) in P(3HB-*co*-3HHx)-*blend*-ENR after isothermal crystallization at T_c = 110 – 117 °C

4.2.4 Kinetics of isothermal crystallization and spherulitic growth rate

The kinetics of isothermal crystallization of P(3HB-*co*-3HHx) after addition of ENR is investigated by means of DSC analysis. Similarly to the discussion mentioned in Section 4.1.6, $t_{0.5}$ can be calculated from the half area of exothermic peak integration. Figure 4.33 depicts the $t_{0.5}$ obtained during isothermal crystallization of P(3HB-*co*-3HHx)-*blend*-ENR. It can be seen that the time it takes to crystallize P(3HB-*co*-3HHx) becomes shorter when ENR is added. With more ENR, the reduction is more pronounced (c.f. exponential fit showed by black and blue dashed curve in Figure 4.33). Based on our previous hypothesis [that ENR chain migrates into P(3HB-*co*-3HHx) chain and causes some disturbance to its molecular mobility as shown in T_g analysis], the ENR chain could act as a nucleating site and may promote the crystallization of

P(3HB-*co*-3HHx). If so, the crystallization rate and spherulitic growth rate of P(3HB-*co*-3HHx) may be faster, and is shown later.

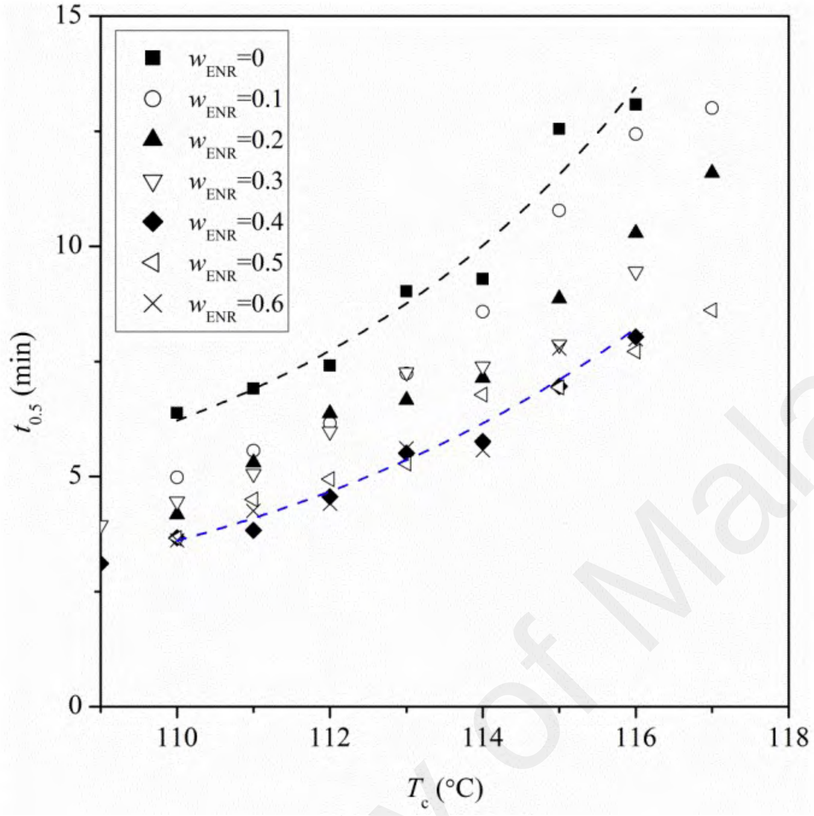

Figure 4.33 Plot of $t_{0.5}$ as a function of isothermal T_c for different compositions of P(3HB-*co*-3HHx) in P(3HB-*co*-3HHx)-*blend*-ENR (dashed curves represent exponential peak fitting obtained from OriginPro 8.1)

The rate constant and Avrami exponent of isothermal crystallization were calculated by means of using Avrami approach. The rate constant of isothermal crystallization as a function of T_c and w_{ENR} is shown in Figure 4.34. In parallel to our observation in $t_{0.5}$ analysis, the rate constant of isothermal crystallization shows an increase in the trend after addition of ENR [Figure 4.34(b)]. The rate constant of isothermal crystallization decreases when T_c is approaching T_m [Figure 4.34(a)].

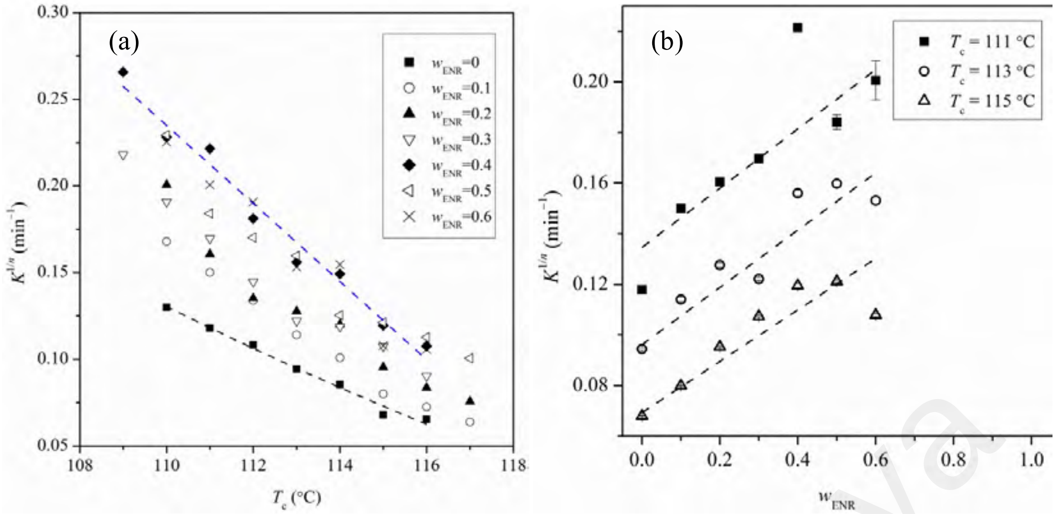

Figure 4.34 Plot of $K^{1/n}$ as a function of (a) isothermal T_c for different compositions of P(3HB-*co*-3HHx)-*blend*-ENR [dashed curves in (a) represent exponential peak fitting obtained from OriginPro 8.1], and (b) ENR weight percent [dashed curves in (b) represent linear peak fitting obtained from OriginPro 8.1]

4.2.5 Spherulitic growth rate

Figure 4.35 shows the *G* values of P(3HB-*co*-3HHx)-*blend*-ENR isothermally crystallized at 116 °C using POM. When ENR is added, the growth rate of P(3HB-*co*-3HHx) spherulites becomes faster. This observation agrees well to that observed in DSC analysis; the constant rate of isothermal crystallization increases with addition of ENR. The measurement of growth rate above 0.6 of w_{ENR} is challenging due to large void within P(3HB-*co*-3HHx) spherulites (c.f. Figure 4.37).

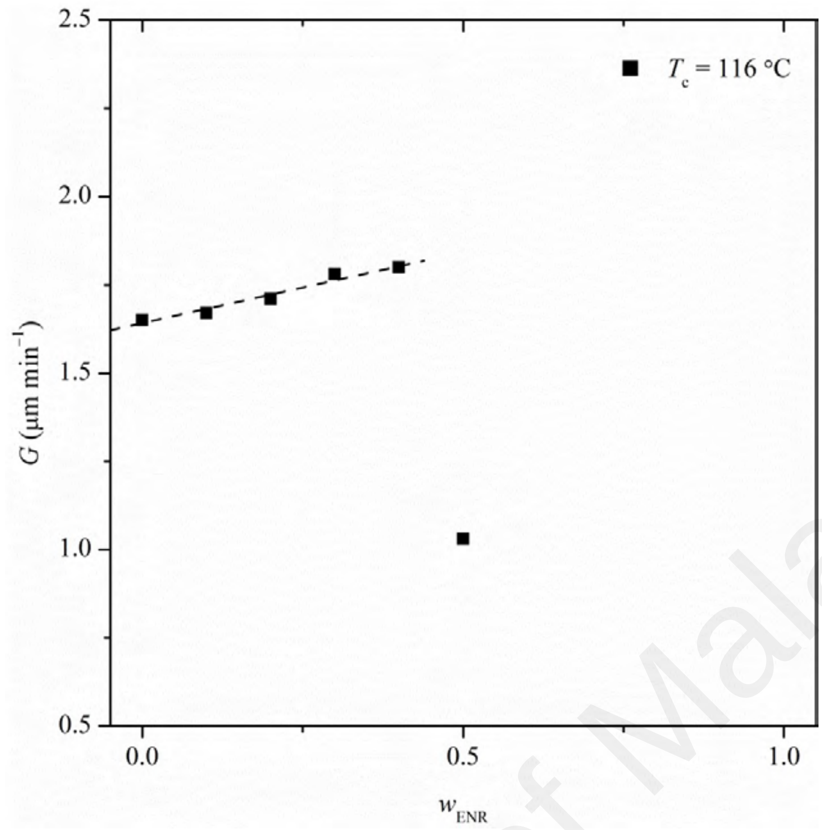

Figure 4.35 Spherulitic growth rate of P(3HB-*co*-3HHx)-*blend*-ENR isothermally crystallized at 116 °C (dashed line is the exponential fitting of the data)

4.2.6 Activation energy of isothermal crystallization

The activation energy of isothermal crystallization of P(3HB-*co*-3HHx) in the blend was calculated in the same way according to Arrhenius-like relationship shown in Section 4.1.8. The calculated activation energies in the corresponding isothermal crystallization temperature of P(3HB-*co*-3HHx)-*blend*-ENR are shown in Figure 4.36. In general, the activation energy required to crystallize P(3HB-*co*-3HHx) gradually decreases from 1.7 kJ mol^{-1} to 1.3 kJ mol^{-1} when ENR is added up to 0.5 in weight fraction. The activation energy can then be correlated to the crystallization rate of P(3HB-*co*-3HHx) in the blends. Higher constant rate of isothermal crystallization yields lower activation energy.

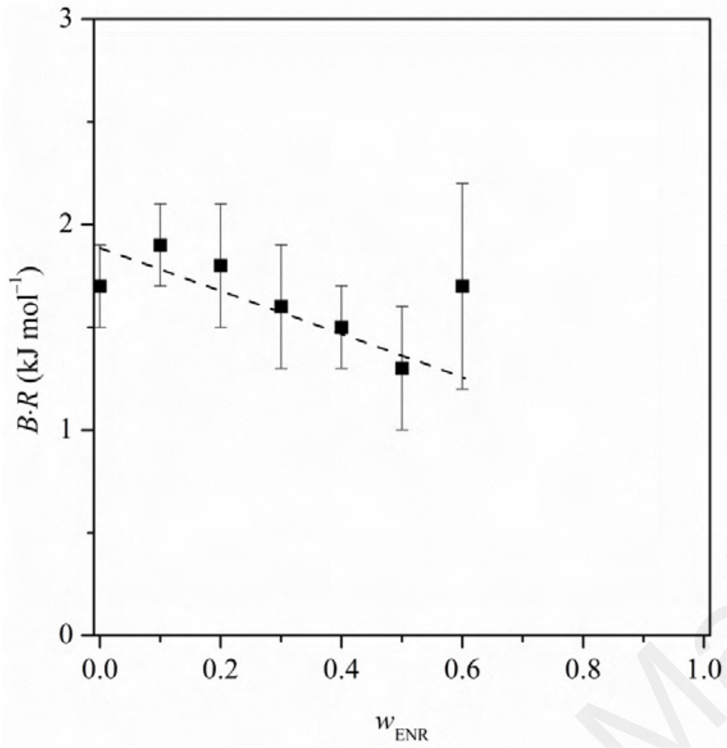

Figure 4.36 Activation energy during crystallization of P(3HB-*co*-3HHx) in ENR blends (dashed line is for visual aid)

4.2.7 Blend morphologies

Figure 4.37 shows the volume-filled P(3HB-*co*-3HHx) spherulites isothermally crystallized at 116 °C. The blend morphologies of P(3HB-*co*-3HHx) do not differ much with addition of 0.1 and 0.2 weight fraction of ENR. They exhibits maltese cross shape. However, when 0.3 weight fraction of ENR is present, one sees less appearance of crystalline band. By increasing the ENR content to 40wt% (w_{ENR} = 0.4), there is a huge dark region possibly due to the existence of ENR in inter-spherulitic region of P(3HB-*co*-3HHx). One sees immediately a drastic change in the spherulites of P(3HB-*co*-3HHx) when w_{ENR} is equal to 0.6.

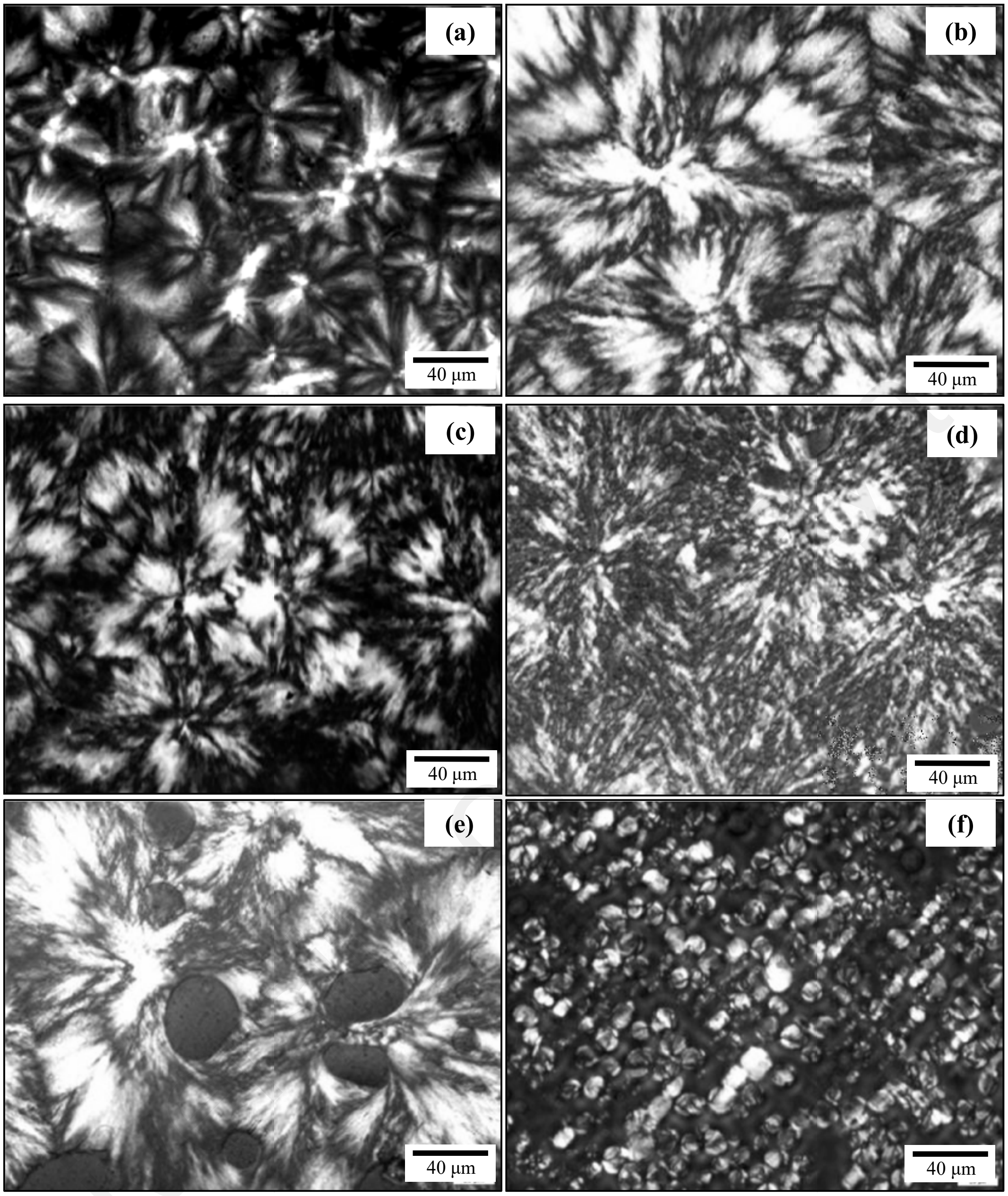

Figure 4.37 Optical micrographs of fully-impinged (a) P(3HB-*co*-8mol% 3HHx) and P(3HB-*co*-8mol% 3HHx)-*blend*-ENR, with ratio of (b) 90/10, (c) 80/20, (d) 70/30, (e) 60/40 and (f) 40/60, isothermally crystallized at T_c = 116 °C for $t_{0.5}$ (magnification 50 ×). Micrographs were taken in between 120 and 150 minutes after isothermal crystallization.

The SEM surface morphologies of etched and as-prepared bulk P(3HB-*co*-3HHx)-*blend*-ENR film samples are shown in Figures 4.38, 4.39, and 4.40. The ENR phase was removed by dissolution in tetrahydrofuran while P(3HB-*co*-3HHx) is not dissolvable in tetrahydrofuran.

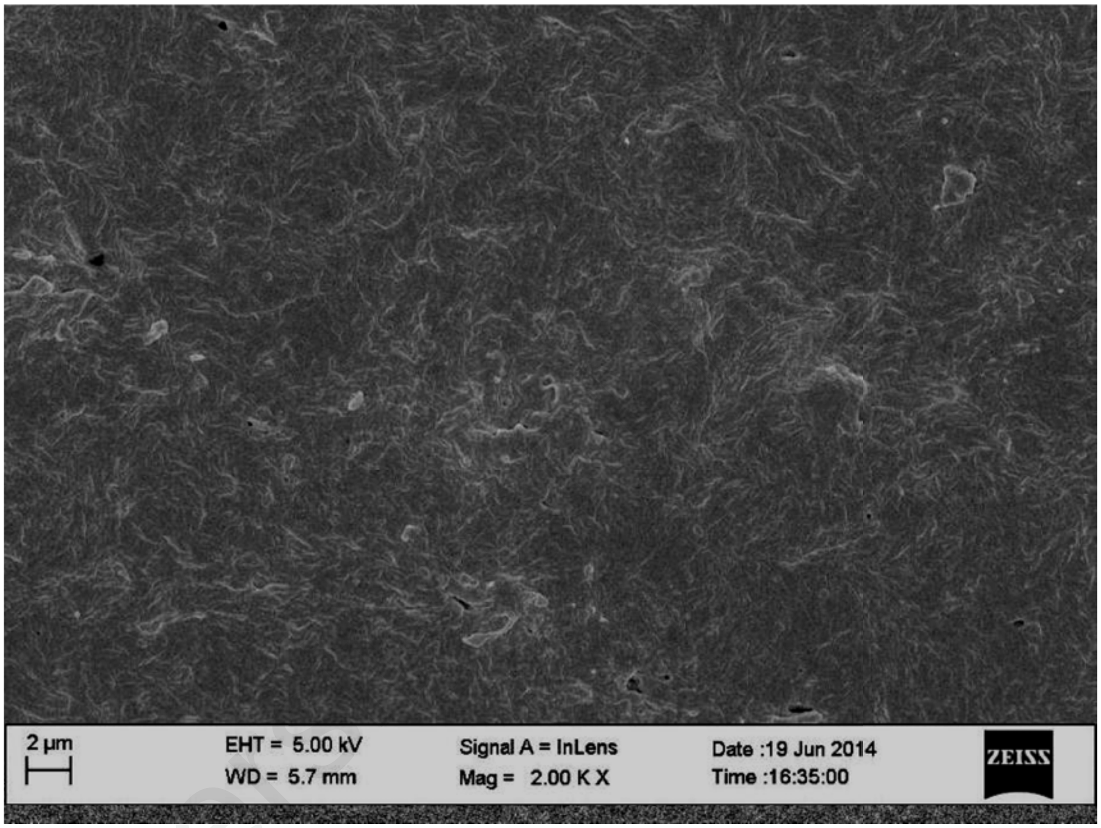

Figure 4.38 SEM image of neat P(3HB-*co*-3HHx) (or $w_{\text{ENR}} = 0$)

Figure 4.39 shows the SEM image of P(3HB-*co*-3HHx)-*blend*-ENR that contains $w_{\text{ENR}} = 0.2$. Compared to previous image, one sees in this image many empty voids as the result of dispersed ENR phase. Since P(3HB-*co*-3HHx) and ENR are immiscible from T_g and T_m^0 analyses, it is reasonable that ENR is located mainly outside the perimeter of P(3HB-*co*-3HHx) domain (c.f. solid yellow circle in Figure 4.39). Even so, there are a part of voids in which ENR is seen to exist in the inter-spherulitic phase of P(3HB-*co*-3HHx) (c.f. white arrows in dashed circle).

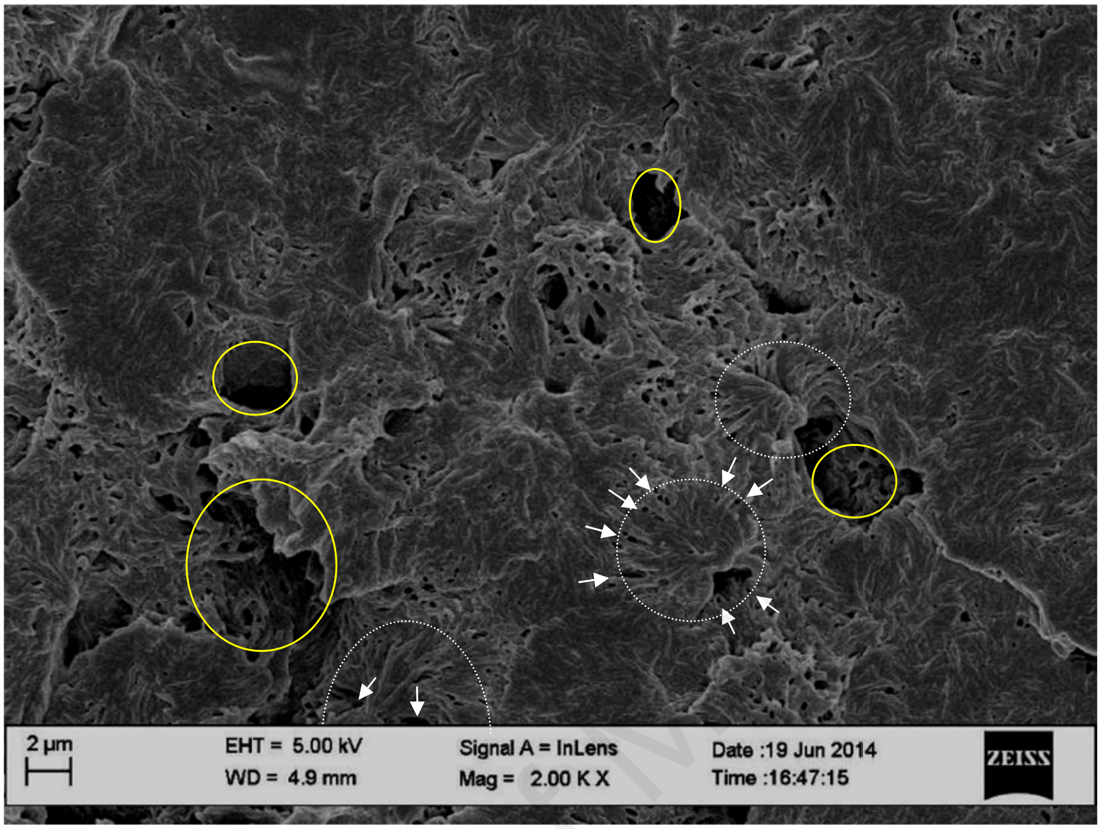

Figure 4.39 SEM image of P(3HB-*co*-3HHx)-*blend*-ENR containing w_{ENR} = 0.2 [Yellow circle indicates large voids in which ENR is rich. White circle could be P(3HB-*co*-3HHx) spherulites. White arrow indicates ENR in inter-spherulitic region of P(3HB-*co*-3HHx)]

Next SEM image shows the surface of P(3HB-*co*-3HHx)-*blend*-ENR containing w_{ENR} = 0.4 (Figure 4.40). In this micrograph, one sees easily a co-continuous void that represents co-continuous phase of ENR in P(3HB-*co*-3HHx). At the border of P(3HB-*co*-3HHx) phase, the surface is rough and small voids (ENR) are detected. It should be noted that SEM images for blends containing w_{ENR} = 0.6 and above were not successfully performed because P(3HB-*co*-3HHx) is a dispersed phase.

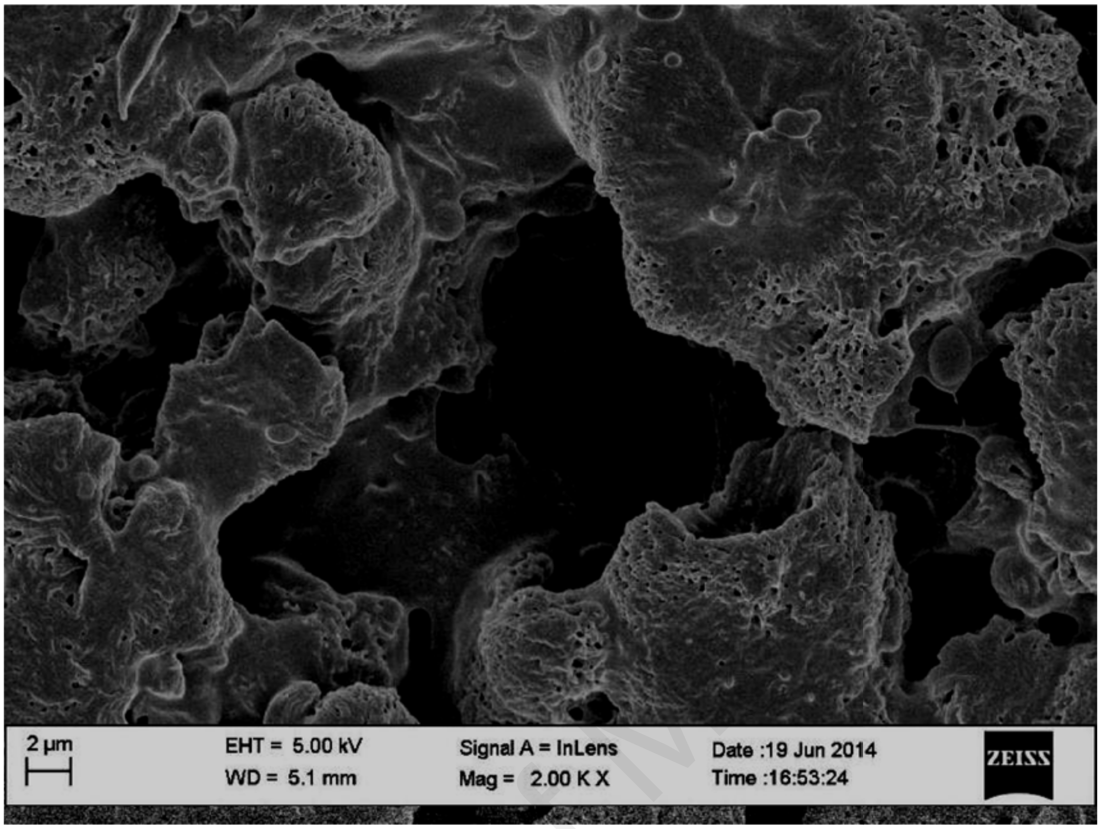

Figure 4.40 SEM image of P(3HB-*co*-3HHx)-*blend*-ENR containing $w_{\mathrm{ENR}} = 0.4$

Figure 4.41 shows the surface morphology of P(3HB-*co*-3HHx)-*blend*-ENR observed using optical microscope. The micrographs were taken on as-prepared bulk P(3HB-*co*-3HHx)-*blend*-ENR without any etching. When 0.2 wt% of ENR is added, ENR exists in droplets randomly distributed in the blend system. When more ENR is added, the surface area of droplets increases.

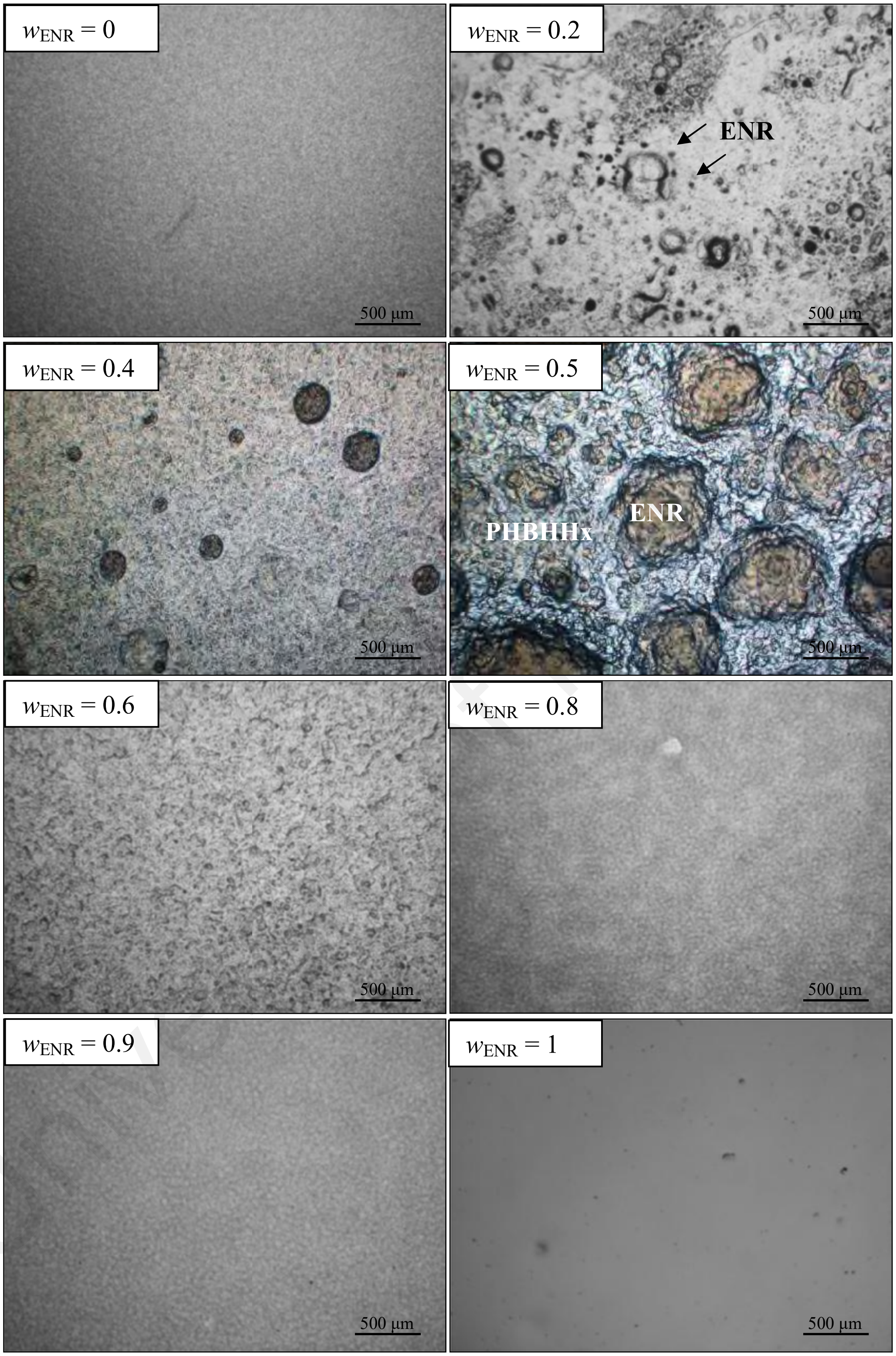

Figure 4.41 Surface morphology of as-prepared P(3HB-*co*-3HHx)-*blend*-ENR at room temperature using POM (magnification 2.5×)

4.2.8 Mechanical properties

Storage modulus (E') and loss modulus (E'') for P(3HB-*co*-3HHx) and its blends are presented in Figure 4.42. At sufficiently high frequency, which is above 300 Hz, P(3HB-*co*-3HHx) and ENR sample undergo a condition where both polymers and DMA instrument begin to resonate. This makes desired information (quantities E' and E'') above 300 Hz ambiguous. Quantity E' is around an order of magnitude larger than E'' in P(3HB-*co*-3HHx), and is almost plateau with slight increase as a function of frequency. As the content of ENR increases, the gap between E' and E'' reduces, however E' is still larger than E''. Quantity E' of P(3HB-*co*-3HHx) ($1.38 \times 10^9\ \omega^{0.02}$ Pa) is in general three order of magnitudes larger than that of ENR ($1.13 \times 10^6\ \omega^{0.23}$ Pa). The term ω is the angular frequency and is defined as $2\pi f$, where f is a frequency measured in Hertz. This indicates that the elastic energy storage is larger than the energy dissipation caused by the viscosity, in other terms it shows solid-like behavior. These observations are reasonable since ENR has very high elasticity thus less rigidity as compared to P(3HB-*co*-3HHx). Unlike the behavior of semi-crystalline in molten state, P(3HB-*co*-3HHx) and its blends do not undergo reduction of molecular weight caused by thermal degradation (Padermshoke et al., 2004; H. Sato et al., 2006). There is no irreversible breakage of polymer chains when frequency sweep is applied at 30 °C. When the content of ENR-50 increases in the blends, the gap between E' and E'' reduces, and the quantity E' increases as a function of frequency signifying elastic material and a flow-like behavior, respectively.

From the slope and intercept of double log *E*’ and *E*” *vs f*, frequency dependencies of *E* and *E*’ in the low-frequency range (0.01 – 1 Hz) is given as:

	After E vs f	*After E’ vs f*
ENR-50 = 0	E (Pa) = $1.38\cdot10^{9}\ \omega^{0.02}$	E' (Pa) = $1.38\cdot10^{9}\ \omega^{0.02}$
ENR-50 = 10	E (Pa) = $4.27\cdot10^{8}\ \omega^{0.04}$	E' (Pa) = $4.25\cdot10^{8}\ \omega^{0.04}$
ENR-50 = 20	E (Pa) = $6.76\cdot10^{7}\ \omega^{0.13}$	E' (Pa) = $6.66\cdot10^{7}\ \omega^{0.15}$
ENR-50 = 30	E (Pa) = $7.33\cdot10^{7}\ \omega^{0.13}$	E' (Pa) = $7.04\cdot10^{7}\ \omega^{0.14}$
ENR-50 = 40	E (Pa) = $7.83\cdot10^{7}\ \omega^{0.14}$	E' (Pa) = $7.54\cdot10^{7}\ \omega^{0.15}$
ENR-50 = 50	E (Pa) = $2.75\cdot10^{7}\ \omega^{0.15}$	E' (Pa) = $2.70\cdot10^{7}\ \omega^{0.16}$
ENR-50 = 60	E (Pa) = $1.39\cdot10^{7}\ \omega^{0.12}$	E' (Pa) = $1.38\cdot10^{7}\ \omega^{0.13}$
ENR-50 = 70	E (Pa) = $5.27\cdot10^{6}\ \omega^{0.15}$	E' (Pa) = $5.20\cdot10^{6}\ \omega^{0.16}$
ENR-50 = 80	E (Pa) = $1.67\cdot10^{6}\ \omega^{0.21}$	E' (Pa) = $1.64\cdot10^{6}\ \omega^{0.24}$
ENR-50 = 90	E (Pa) = $1.54\cdot10^{6}\ \omega^{0.23}$	E' (Pa) = $1.52\cdot10^{6}\ \omega^{0.25}$
ENR-50 = 100	E (Pa) = $1.14\cdot10^{6}\ \omega^{0.20}$	E' (Pa) = $1.13\cdot10^{6}\ \omega^{0.23}$

Results show that *E*’ agrees almost with complex modulus (*E*) as a function of frequency. The relaxation exponent, *n*, is quite small and is in agreement to $E'(\omega) \propto \omega^{n}$. Quantity *n* increases with increasing ENR-50 content while the exponent before ω decreases with increasing ENR-50.

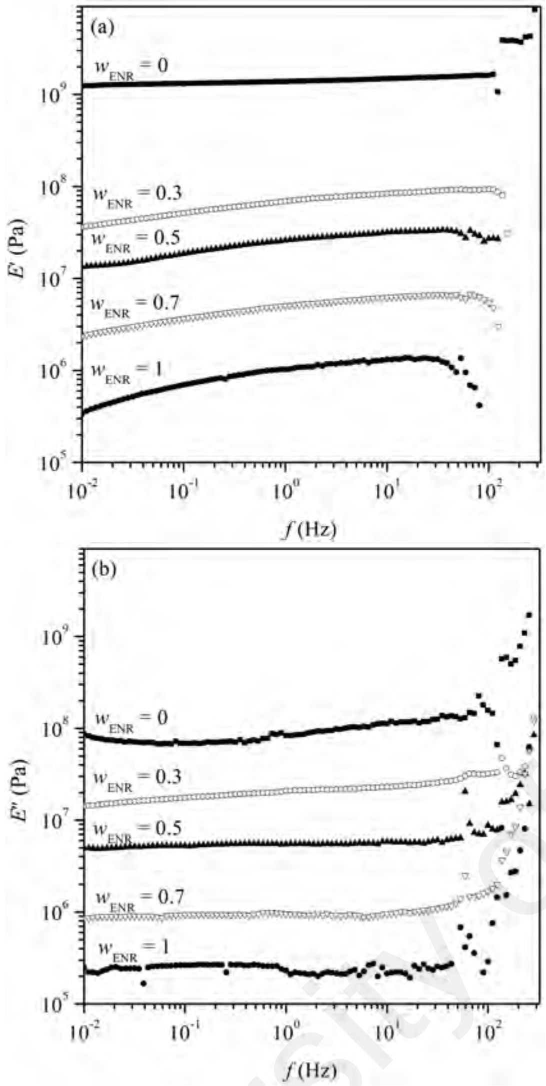

Figure 4.42 Double log plot of (a) elastic and (b) loss moduli of P(3HB-*co*-3HHx)-*blend*-ENR as a function of frequency. ■ - w_{ENR}=0; ○ - w_{ENR}=0.3; ● - w_{ENR}=0.5; ▲- w_{ENR}=0.7; □ - w_{ENR}=1

4.3 Melt reaction between P(3HB-*co*-8mol% 3HHx) and ENR

4.3.1 Glass transition temperature

Figure 4.43(a) shows T_g curves of 50:50 by weight P(3HB-*co*-3HHx)-*blend*-ENR as a function of reaction time. The T_g value is characterized by the maximum peak of derivative heat flow as depicted in Figure 4.43(b). The reaction time is given by half-time of isothermal melt reaction ($t_{0.5,\mathrm{rb}}$). This quantity is obtained from the half integration area of exothermic peak at isothermal reaction temperature (T_{rb}) of 195 °C (example shown in Figure 4.40). In the beginning ($0 \times t_{0.5,\mathrm{rb}}$), there are two T_gs at −17 °C [ΔC_p = 0.29 J (g °C)$^{-1}$] and −1 °C [ΔC_p = 0.23 J (g °C)$^{-1}$], which characterizes the vitreous-rubbery transition of ENR and P(3HB-*co*-3HHx), respectively. The fact that two T_gs were observed means that P(3HB-*co*-3HHx)-*blend*-ENR is immiscible before melt reaction. These values become closer to each another and progressively become one at $1 \times t_{0.5,\mathrm{rb}}$ [T_g = −9 °C; ΔC_p = 0.52 J (g °C)$^{-1}$], implying a chemical interaction at the interface between P(3HB-*co*-3HHx) and ENR during melt reaction. For example, the T_g of ENR and P(3HB-*co*-3HHx) shifts to −14 °C and −4 °C respectively in $0.25 \times t_{0.5,\mathrm{rb}}$, followed by −12 °C and −7 °C respectively in $0.5 \times t_{0.5,\mathrm{rb}}$. There is also a small relaxation peak during the transition in P(3HB-*co*-3HHx). There is no change in the sum values of ΔC_p [0.52 J (g °C)$^{-1}$] between P(3HB-*co*-3HHx)/ENR blend and melt reacted P(3HB-*co*-3HHx)/ENR. The T_g behavior of other compositions was not investigated.

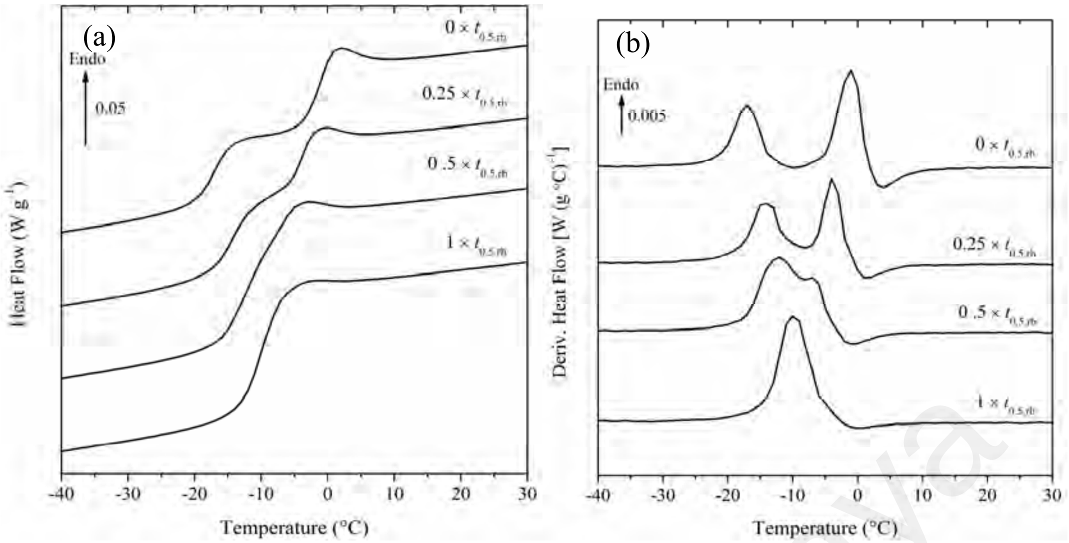

Figure 4.43 (a) Glass transition temperature and (b) its derivative in 50:50 (by weight) P(3HB-*co*-8mol% 3HHx)-*blend*-ENR at different $t_{0.5,rb}$s

4.3.2 Melt reaction heat

Figure 4.44 shows typical DSC traces of melt reaction between P(3HB-*co*-3HHx) and ENR. One observes exothermic reaction heat that depends on blend compositions. Exothermic peak for neat polymers, such as P(3HB-*co*-3HHx) and ENR, is not observed. The exothermic reaction heat is also dependant on temperature of reaction.

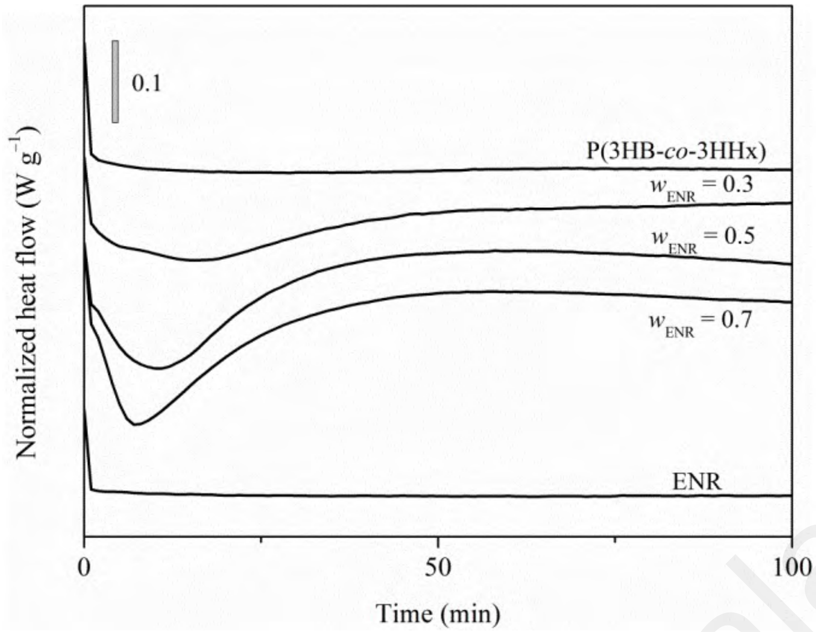

Figure 4.44 DSC traces when the samples were exposed to T_{rb} = 197 °C until complete melt reaction

Selected examples of reaction heat during melt reaction are presented in Figure 4.45. In this figure, the heat of reaction decreases with reaction temperature in blend containing 50 wt% of ENR. The heat of reaction for blend containing w_{ENR} = 0.7 however increases to 193 °C and progressively level off. For blend containing w_{ENR} = 0.3, the heat of reaction decreases with increasing reaction temperature to 193 °C and progressively increases.

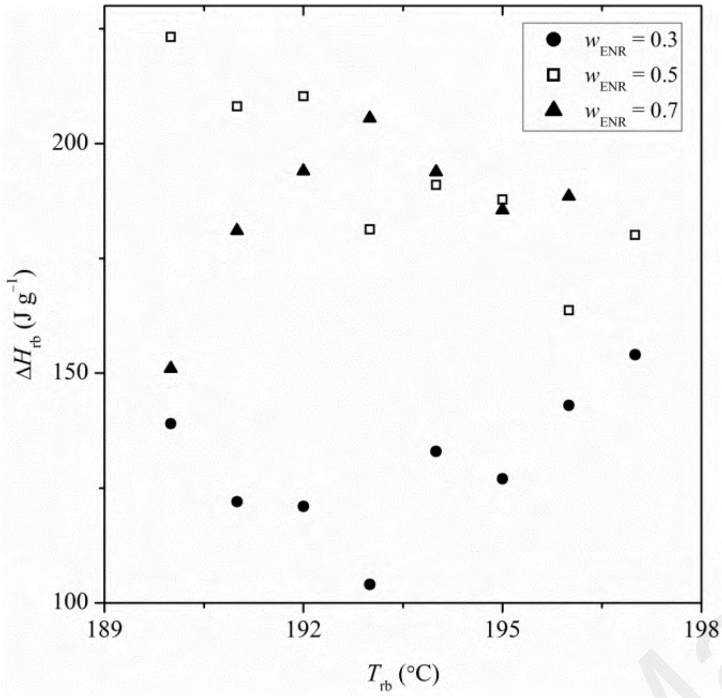

Figure 4.45 Specific heat of melt reaction as a function of reaction temperature for three blend compositions, w_{ENR} = 0.3, 0.5 and 0.7

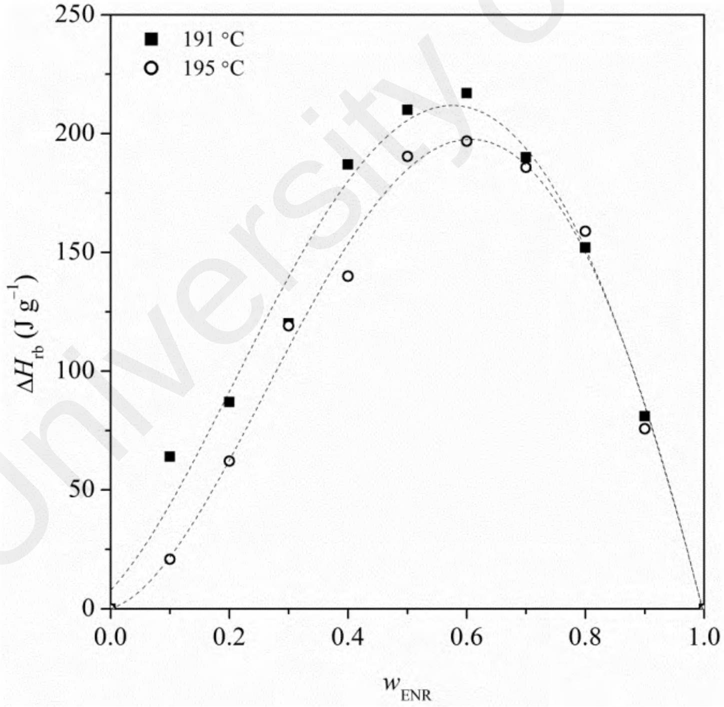

Figure 4.46 Specific heat of melt reaction versus blend composition at different T_{rb}; ■, 191 °C; ○, 195 °C (dashed curve are for visual aid)

4.3.3 Dynamics of reaction

The dynamics of reaction can be characterized by reciprocal $t_{0.5,\mathrm{rb}}$ of the reaction. Figure 4.47 shows the plot of $t_{0.5,\mathrm{rb}}^{-1}$ versus blend composition at T_{rb} = 191, 194 and 197 °C. The rate decreases with increasing P(3HB-*co*-3HHx) content to a linear approximation at $w_{\mathrm{ENR}} = 0$ to 0.5. This range obeys power law approximation, where:

$$\begin{aligned} &\text{At } T_{\mathrm{rb}} = 191\ ^{\circ}\mathrm{C},\ (t_{0.5,\mathrm{rb}})^{-1} = \mathrm{const}\ (w_{\mathrm{ENR}})^{0.67} \\ &\text{At } T_{\mathrm{rb}} = 194\ ^{\circ}\mathrm{C},\ (t_{0.5,\mathrm{rb}})^{-1} = \mathrm{const}\ (w_{\mathrm{ENR}})^{0.67} \qquad (4.3) \\ &\text{At } T_{\mathrm{rb}} = 197\ ^{\circ}\mathrm{C},\ (t_{0.5,\mathrm{rb}})^{-1} = \mathrm{const}\ (w_{\mathrm{ENR}})^{0.66} \end{aligned}$$

The constants are 0.052, 0.057 and 0.078 min^{-1}, respectively. According to Chan et al. (2004), under perfect condition i.e. formation of monodisperse spheres, the $t_{0.5,\mathrm{rb}}$ follows: $(t_{0.5,\mathrm{rb}})^{-1} = \mathrm{const}\ (w_{\mathrm{PHBV}})^{-0.33}$. The quantity $t_{0.5,\mathrm{rb}}$ must decrease with increasing size of the dispersed phase owing to increasing diffusion time of the species to the interfacial area region or the site or reaction. We note that our finding follows similar trend at certain blend compositions ($w_{\mathrm{ENR}} = 0.2 – 0.5$).

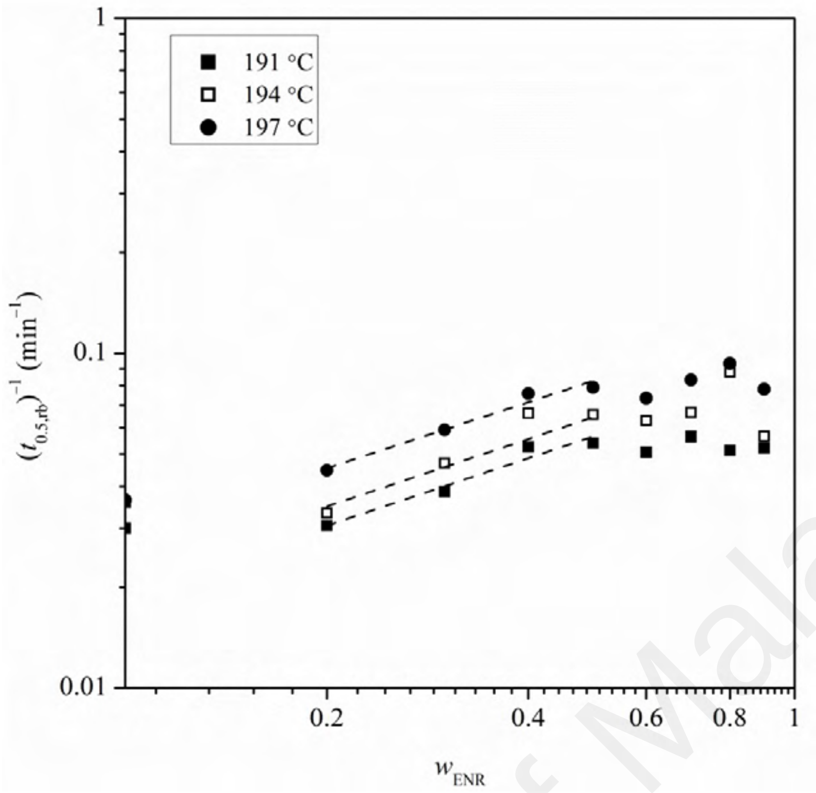

Figure 4.47 Reciprocal half time of melt reaction ($t_{0.5,rb}^{-1}$) as a function of weight fraction of ENR for different T_{rb}; ■, 191 °C; □, 194 °C; ●, 197 °C

According to Chan et al. (2004) and Lee et al. (2005), the dynamics of reaction by a serial reaction scheme can be shown by a decay of P(3HB-*co*-3HHx) (X) under the influence of heat into some reactive product (Y), which is then consumed by the epoxy-reaction to form the final product (Z):

$$X \rightarrow Y \rightarrow Z \qquad (4.4)$$

The occurrence of final product Z is monitored by DSC traces shown in Figure 4.40. We symbolize the (normalized) concentration of X, Y, and Z by x, y, and z and approximate the three stages of Eq. (4.4) as follows:

I) $\mathrm{d}x/\mathrm{d}t = -knt^{n-1}x$ with $x = 1$ at $t = 0$.

Rate constant k and exponent n are parameters.

II) $-\mathrm{d}y/\mathrm{d}t = -k'y + x'$ with $y = 0$ at $t = 0$.

Quantity k' is the rate constant for generation of reactive product Y. The first term represents the consumption of Y by the epoxy-reaction (rate constant k') where as the second term ($x' \equiv \mathrm{d}x/\mathrm{d}t$) gives the production of Y by step I).

III) $\mathrm{d}z/\mathrm{d}t = k'y'$ with $z = 0$ at $t = 0$.

One easily sees that the solution of III) is $x + y + z = 1$. Hence, we arrive eventually at

$$-\ln(1-z) = k't - \ln(1 + k'\int_0^t \mathrm{d}t e^{k't-kt^n}) \tag{4.5}$$

The integral can be replace by the following average

$$k'\int_0^t \mathrm{d}t e^{k't-kt^n} = (e^{-k't} - 1)\overline{\exp(-kt^n)}$$

$$z(t) = (1 - e^{-k't})\left[1 - \overline{\exp(-kt^n)}\right] \tag{4.6}$$

For determination of parameters n, k and k', we introduce the approximation

$$k' = k^{1/n} \tag{4.7}$$

Eq. (4.7) turns out to be an acceptable approximation in the range of small and medium conversions (for $z < 0.5$).

In the limit of small conversions or in the limit $t \rightarrow 0$, the second factor of Eq. (4.6) reads approximately $1 - \overline{\exp(-kt^n)} = kt^n/(n+1)$. It follows for Eq. (4.6)

$$z = \frac{kk'}{n+1} t^{n+1} \quad (t \rightarrow 0) \tag{4.8}$$

Eqs. (4.7) and (4.8) allow determination of the parameters occurring in Eq. (4.6). Figure 4.48 represents experimental results and theoretical curve after Eq. (4.8). It can be seen that Eq. (4.8) is in agreement with experimental results over a wide range of conversions. Marked deviations occur above $z \approx 0.5$.

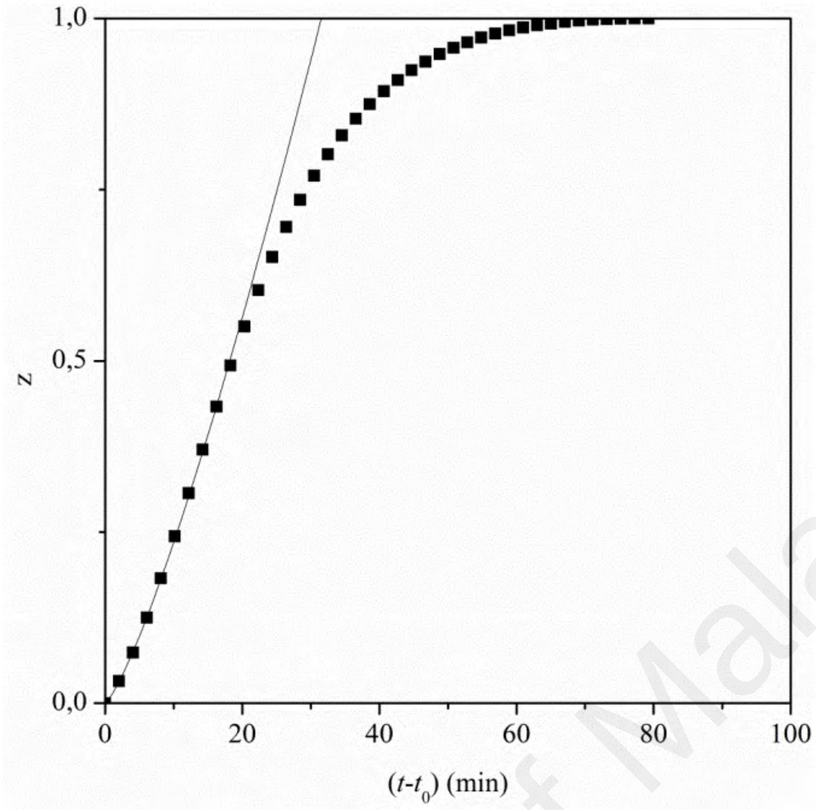

Figure 4.48 Normalized concentration *z* versus time for P(3HB-*co*-3HHx)/ENR 50/50 blends at T_{rb} = 191 °C. The dashed curve is calculated after Eq. (4.8)

Selected results for parameters k' and n are listed in Table 4.12. One recognizes that parameters k' shows qualitatively the same composition dependence as $t_{0.5,\mathrm{rb}}^{-1}$ in Figure 4.47. The quantity k' increases with increasing ENR content at same reaction temperature.

Table 4.12 Parameters *k′* and *n* for selected temperatures and blend compositions: *k′* (*n*)

T_{rb} (°C)	w_{ENR}		
	0.3	0.5	0.7
190	0.0184 (0.13)	0.0362 (0.29)	0.0529 (0.83*)
191	0.0222 (0.12)	0.0384 (0.26)	0.0410 (0.43)
192	0.0234 (0.21)	0.0390 (0.24)	0.0459 (0.44)
193	0.0246 (0.24)	0.0462 (0.35)	0.0474 (0.42)
194	0.0266 (0.17)	0.0463 (0.29)	0.0498 (0.38)
195	0.0268 (0.14)	0.0519 (0.31)	0.0552 (0.44)
196	0.0285 (0.11)	0.0520 (0.29)	0.0609 (0.46)

Parameter *k′* is given in min^{-1}. *not included in graph fitting in Figure 4.49.

The temperature dependence of *k′* follows Arrhenius equation to a good approximation. An example of three blend compositions is shown in Figure 4.49. The corresponding activation energies are 89 ± 2 kJ mol^{-1} ($w_{ENR} = 0.3$), 111 ± 2 kJ mol^{-1} ($w_{ENR} = 0.5$), and 134 ± 2 kJ mol^{-1} ($w_{ENR} = 0.7$). Similarly to P(3HB-*co*-3HV) system reported by Chan and co-workers (2004), the activation energy of P(3HB-*co*-3HHx) is also not symmetrical (c.f. Figure 4.49) with respect to blend compositions. It was reported that the activation energies for P(3HB-*co*-3HV) melt reaction are 49 kJ mol^{-1} ($w_{ENR} = 0.3$), 81 kJ mol^{-1} ($w_{ENR} = 0.5$), and 112 kJ mol^{-1} ($w_{ENR} = 0.7$). By comparison, the activation energies of P(3HB-*co*-3HHx) during melt reaction are approximately higher than that of P(3HB-*co*-3HV).

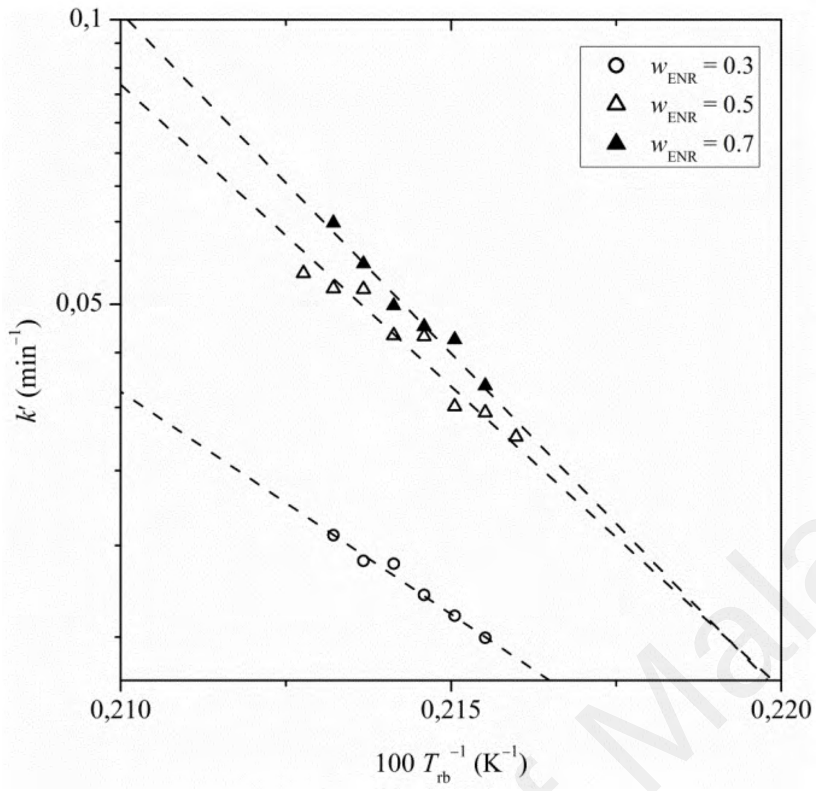

Figure 4.49 Temperature dependence of parameter k' for P(3HB-*co*-3HHx)-*blend*-ENR of different compositions. w_{ENR} (○) 0.3, (Δ) 0.5, (▲) 0.7

4.3.4 Heat-cool-heat

Crystallization-melting behavior of P(3HB-*co*-3HHx) during the course of melt reaction was investigated. Figure 4.50 shows the DSC curves of 50:50 by weight P(3HB-*co*-3HHx)-*blend*-ENR for different $t_{0.5,rb}$ at T_{rb} = 195 °C. Before melt reaction, P(3HB-*co*-3HHx) can crystallize and melt. The cold crystallization of P(3HB-*co*-3HHx) in the blend occurs at 83 °C (ΔH_{cc} = 6 J g^{-1}) and this crystalline phase melts at 137 °C (ΔH_m = 10 J g^{-1}). There are two melting peaks corresponding to melt-recrystallization-melt phenomenon. After melt reaction, the cold crystallization and melting temperatures shift to lower values with the evolution of melt reaction and gradually diminishes. This shows that there is a structural change attributed to melt reaction and that the crystallization of P(3HB-co-3HHx) is inhibited after melt reaction. Quantity X^*

decreases from 5% in 0 × $t_{0.5,rb}$ to 2% in 1 × $t_{0.5,rb}$. Thus, it can be deduced that the blend of 50:50 is almost entirely amorphous after melt reaction. The crystallizability of P(3HB-*co*-3HHx) after melt reaction is shown later. Table 4.13 summarizes all physical quantities of thermal event in P(3HB-*co*-3HHx) and ENR after melt reaction.

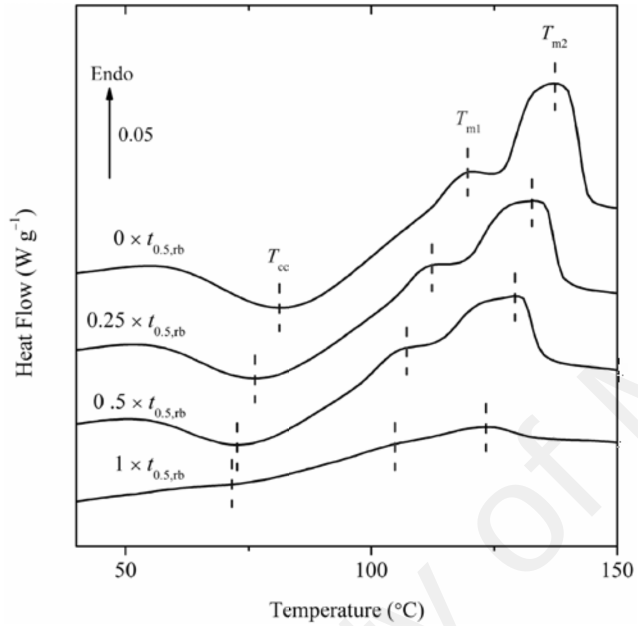

Figure 4.50 Crystallization and melting temperatures in 50:50 (by weight) P(3HB-*co*-8mol% 3HHx)-*blend*-ENR at different $t_{0.5,rb}$ at T_{rb} = 195 °C

Table 4.13 Physical quantities of thermal event in P(3HB-*co*-3HHx) and ENR during melt reaction at T_{rb} = 195 °C

Reaction time (min)	T_{g1} (°C)	T_{g2} (°C)	ΔT_g (°C)	T_{cc} (°C)	ΔH_{cc} (J g^{-1})	T_{m1} (°C)	T_{m2} (°C)	ΔH_m (J g^{-1})	X^* (%)[a]
0	−17	−1	44	83	6	119	137	10	5
¼	−14	−4	42	78	5	111	131	8	4
½	−12	−7	40	74	4	106	129	7	4
1[*]	−9		41	78	0.4	104	121	2	2

[*] $t_{0.5,rb}$ = 13.3 min based on half integration peak area in DSC during reaction

[a] calculated after Eq. (2.2)

4.3.5 Isothermal crystallization and spherulitic growth rate

Isothermal crystallization of melt reacted product was attempted. After melt reaction at 197 °C for 2 × $t_{0.5,rb}$, the sample was cooled to preselected isothermal crystallization temperature ranging from 30 to 110 °C. However, there was no sight of exothermic peaks in DSC after 1 h for all studied temperatures. At this point, the growing spherulites could be too slow that it is practically not possible to study of isothermal crystallization kinetics after melt reaction.

4.3.6 Thermal decomposition

Figure 4.51 shows the weight loss profile during melt reaction of P(3HB-*co*-3HHx)-*blend*-ENR at T_{rb}=195 °C. There are two variations in terms of reaction time, $t_{0.5,rb}$ and 5 × $t_{0.5,rb}$. During melt reaction of P(3HB-*co*-3HHx)-*blend*-ENR, one observes mass loss. At one half-time of melt reaction, there is a slight variation of weight loss as a function of ENR mass fraction. Even so, these changes are negligible (≤ 2%). It should be noted that there is a mass loss of less than 1% in neat P(3HB-*co*-3HHx) and ENR during isothermal temperature at 195 °C (data not shown), which is within the instrumental error (2%). By comparing the weight loss profile of P(3HB-*co*-3HHx)-*blend*-ENR to that of neat P(3HB-*co*-3HHx) and ENR, it is certain that there is a formation of secondary volatile product(s) aside from the main reaction between carboxyl end group of P(3HB-*co*-3HHx) and epoxide group of ENR (Figure 4.52). According to reaction mechanism proposed by Lee et al (2005) and Chan et al (2004), water as secondary product is most likely to form during melt reaction. However at this point, there is no experimental evidence on the analysis of volatile product(s) formed during melt reaction. We then investigated the mass loss of P(3HB-*co*-3HHx)-*blend*-ENR at prolong reaction time such as 5 × $t_{0.5,\mathrm{rb}}$. At a glance, the mass loss that takes place during melt reaction increases from ~8% in w_{ENR}=0.1 to ~16% in w_{ENR}=0.3, and gradually decreases to ~4% in w_{ENR}=0.9. Here, there are two behaviors of decomposition. The former is attributed to P(3HB-*co*-3HHx)-rich phase (w_{ENR}=0.1-0.3) having wider distribution of mass losses, and the latter is attributed to ENR-rich phase (w_{ENR}=0.7-0.9) having lower distribution of mass losses (c.f dashed lines in Figure 4.51). The kinetic of weight loss in blend containing 10% P(3HB-*co*-3HHx) as a dispersed phase is different to that when 10% ENR is present as the dispersed phase. Although one may argue that the mass loss of blend containing w_{ENR}=0.4 is lower than that of blend containing w_{ENR}=0.3 and 0.5, the origin of lower mass loss in this particular blend is unknown as yet. It could be due to a wide data distributions in P(3HB-*co*-3HHx)-rich phase or could be due to morphological differences. At w_{ENR}=0.4, a co-continuous percolation network is formed.

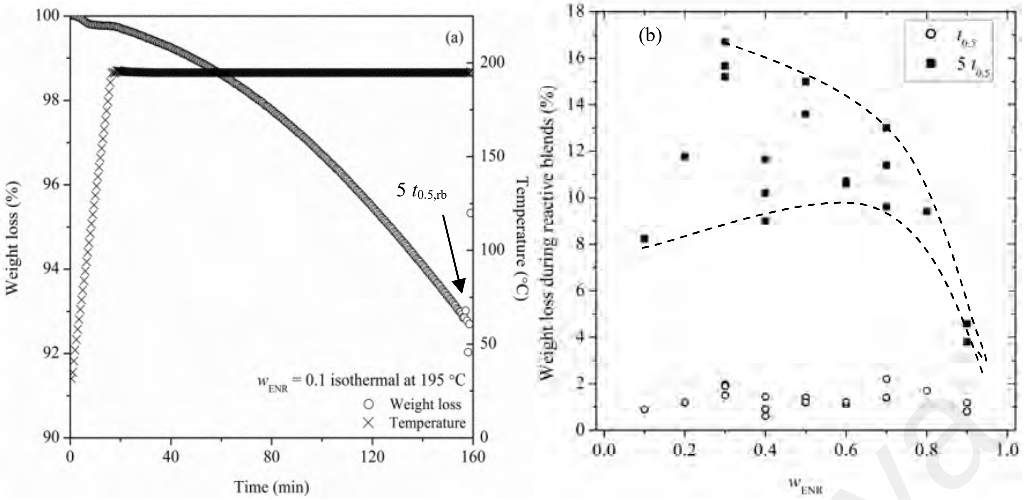

Figure 4.51 (a) Weight loss as a function of time during the melt reaction of P(3HB-*co*-8mol% 3HHx)-*blend*-ENR containing 10 wt% of ENR at T_{rb} = 195 °C. (b) Changes of mass as a function of ENR weight fraction for different reaction times at T_{rb} = 195 °C. Each marker in (b) represents one experimental run (dashed lines are drawn for visual aid).

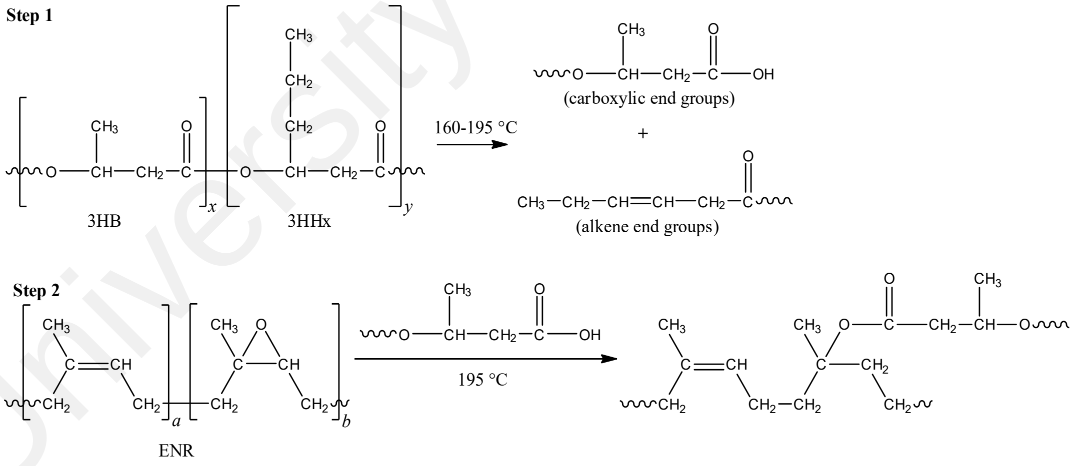

Figure 4.52 Melt reaction between P(3HB-*co*-3HHx) and ENR (x = 92 mol%, y = 8 mol%, a = 50 mol%, b = 50 mol%)

Further investigation of the thermal stability of melt reacted P(3HB-*co*-3HHx)-*blend*-ENR was carried by means of conventional heating run in TGA at 10 K min^{-1}. Figure

4.53(a) shows the TGA profile of P(3HB-*co*-3HHx)-*blend*-ENR after melt reaction. The decomposition of P(3HB-*co*-3HHx)-*graft*-ENR exhibits two-step decompositions corresponding to P(3HB-*co*-3HHx) at lower temperature and ENR at higher temperature. Although similar data extraction of T_g (based on maximum derivative peak) was intended to extract the decomposition temperature values, it is difficult to obtain reliable values due to complicated nature of melt reaction. The effect of complicated nature of melt reaction followed by possible 'aging' of ENR [c.f. small figure in Figure 4.53(a)] can be observed at the final mass at 500 °C. There is a remaining of 10% mass or less in almost all blend compositions after melt reaction. Thus, a kinetic approach is an ideal way to probe the influence of melt reaction to thermal decomposition of P(3HB-*co*-3HHx)-*graft*-ENR. By considering the fact that it is a complicated system, we use the simplest method to study the kinetic of decomposition. The activation energy during decomposition is calculated using Eq. (2.15). Figure 4.53(b) shows the plot of *ln*|deriv. weight loss| against 1/*T* for P(3HB-*co*-3HHx)-*blend*-ENR after melt reaction. In the beginning and at the end of decomposition shown in Figure 4.53(b), there are large data dispersions. It is tricky to make an exact evaluation of the activation energy, thus was not used for calculation. The domain of analysis for the activation energy of some blend compositions is shown in Appendix I by the red portion. These figures are inter-connected to the linear dashed line in Figure 4.53(b). On the basis of validation, the corresponding decomposition before and after was constructed in a way that the activation energy falls in the same domain of analysis.

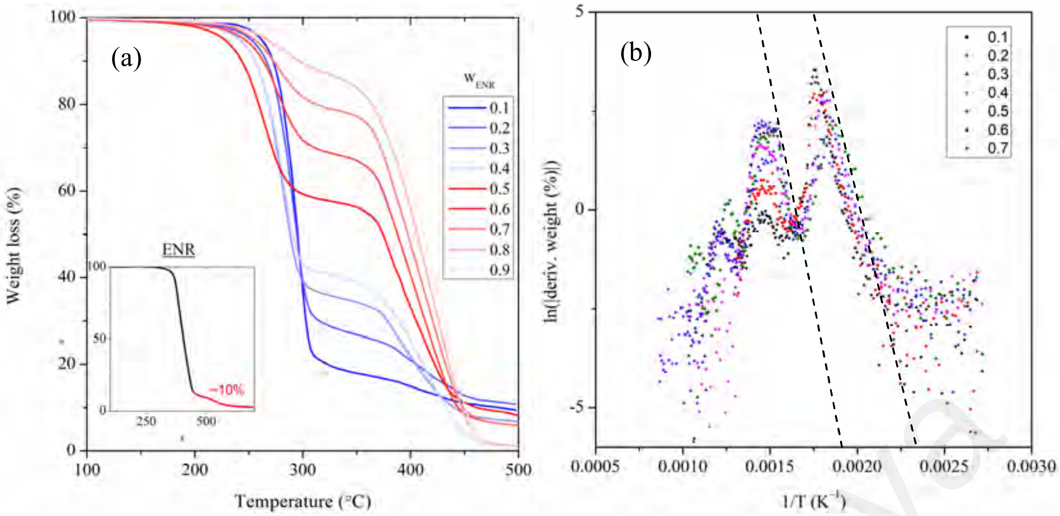

Figure 4.53 (a) TGA and (b) its derivative profile of P(3HB-*co*-8mol% 3HHx)-*blend*-ENR after melt reaction (dashed lines are for visual aid)

The activation energy of P(3HB-*co*-3HHx)-*graft*-ENR is shown in Figure 4.54. The present values (after melt reaction) were used as a comparison to the activation energy before melt reaction. On analyzing this curve, it can be appreciated that the activation energy for P(3HB-*co*-3HHx) before melt reaction is almost constant at 17 kJ with slight shift to lower activation energy at 19 kJ in between w_{ENR} = 0.4-0.6 [c.f. Figure 4.54(a)]. The activation energy of ENR in the blend is also constant in the beginning (w_{ENR} = 0.8-1) at ~19 kJ. With increasing 3HHx content in the blend, the activation energy of ENR decreases by approximately 5 kJ [c.f. Figure 4.54(b)]. The lowest activation energy of ENR (15 kJ) occurs at w_{ENR}=0.1. In both cases even though P(3HB-*co*-3HHx) and ENR are immiscible, there is a diffusion of ENR in P(3HB-*co*-3HHx) domain and vice versa. As the result, there is less stabilization effect and the activation energy decreases. The same trend of activation energy is also observed in P(3HB-*co*-3HHx)-*blend*-ENR after melt reaction. However, these activation energies are far lower (50-80% depending on the blend compositions) than that before melt reaction.

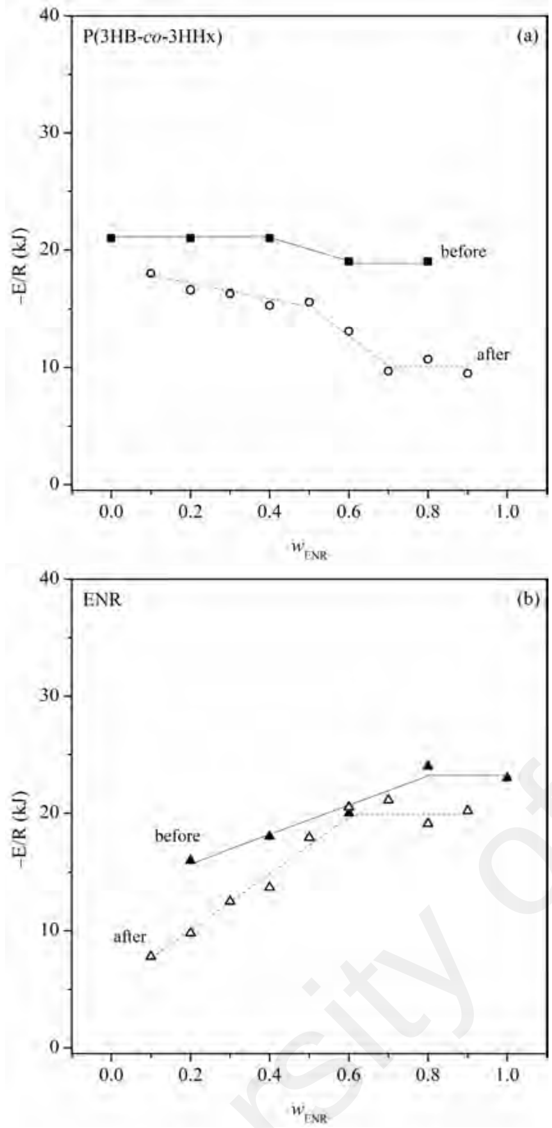

Figure 4.54 Activation energy of P(3HB-*co*-8mol% 3HHx)-*graft*-ENR [(a) P(3HB-*co*-3HHx) and (b) ENR] (straight and dashed lines are for visual aid)

4.3.7 FTIR investigation

Changes in the molecular structure of P(3HB-*co*-3HHx)-*blend*-ENR was investigated during reactive blends. Figure 4.55 shows the FTIR spectra of P(3HB-*co*-3HHx)-*blend*-ENR after different $t_{0.5,rb}$s. A summary of all absorption bands is summarized in Appendix J. In general, all absorption bands of P(3HB-*co*-3HHx) and ENR are similar to that reported in the known literature (Hallensleben, Schmidt, & Schuster, 1995; Padermshoke et al., 2004; H. Sato et al., 2006; Van Zyl, Graef, Sanderson, Klumperman, & Pasch, 2003). During melt reaction, all crystalline sensitive bands of P(3HB-*co*-3HHx) decreases with increasing reaction time. The most prominent changes can be clearly seen at wave number 1722 cm^{-1} which corresponds to the stretching vibration of unsaturated carbonyl group. This wave numbers which is crystalline sensitive band decreases from $t_{0.5,rb}$ to 5 × $t_{0.5,rb}$, leaving more visibility for its shoulder peak. The absorption band at 1734 cm^{-1} corresponds to the absorption band of amorphous phase in P(3HB-*co*-3HHx). All other crystalline sensitive bands [1275 and 1227 cm^{-1} (sp^3 stretching vibration of acyl C-O), 978 and 923 cm^{-1} (sp^2 CH bend of monosubstituted alkene)] are also significantly influenced during the melt reaction. Conversely, it can be observed that the sp^3 stretching vibration of acyl C-O that is not crystalline sensitive at wavenumber 1182 cm^{-1} do not change during the course of melt reaction. The IR analysis agrees well to the result of DSC aforementioned, that the product of melt reaction is almost entirely amorphous. Meanwhile, the main absorption band that characterizes the melt reaction is located at 876 cm^{-1}, which corresponds to the oxirane group of ENR. This absorption band diminishes after 5 × $t_{0.5,rb}$. This behavior strongly suggests that the melt reaction takes place by ring opening at the tricyclic group with high constrain energy, and not at the unsaturated bond of NR at 835 cm^{-1}. It is however interesting to note that the sp^2 CH bends of germinal disubstituted alkene (possibly of 3HB monomeric unit) and trisubstituted alkene (possibly of 3HHx monomeric unit) decrease during melt reaction and finally disappear. It is proposed that there could be a reaction between the end group of sp^2 carbon of P(3HB-*co*-3HHx) as the chain-scission product and ENR. According to a mechanism proposed by Lee et al (2005), there is only one reaction between the carbonyl end group of short chain poly(3-hydroxybutyrate) with the oxirane group of ENR. However at this point, there is no experimental evidence to support this proposal. Further experiment is required for a complete understanding of the molecular structure of P(3HB-*co*-3HHx) and ENR during melt reaction.

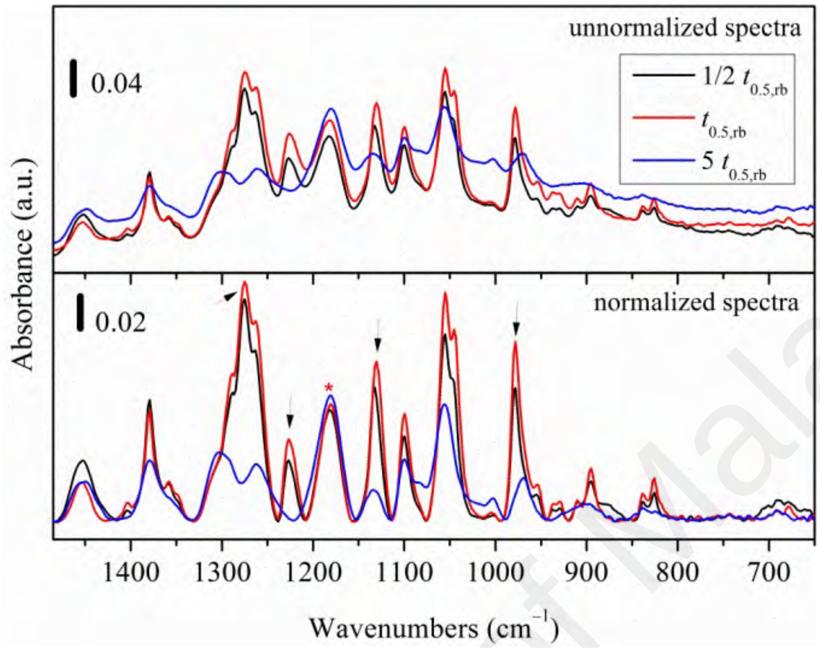

Figure 4.55 FTIR spectra of P(3HB-*co*-8mol% 3HHx)-*blend*-ENR at different $t_{0.5,rb}$ (top: unnormalized spectra; bottom: normalized spectra)

Figure 4.56 describes quantitatively changes in the intensity of absorption bands from 600 to 1500 cm^{-1}. This value was obtained after normalization against baseline and reference (unchanging) absorption band at 1180 cm^{-1} (indicated by star in Figure 4.55). Normalization was performed by selecting the lowest points of the each absorption spectra. The band at 1180 cm^{-1} is the adsorption band of C-O-C (amorphous) in P(3HB-*co*-3HHx) (c.f. Table 4.3 for FTIR peaks assignment). From DSC study after melt reaction (Table 4.12), it was shown that the crystallizability of P(3HB-*co*-3HHx) in the blend after melt reaction is inhibited. Thus, it is reasonable that the wavenumbers at 1180 cm^{-1} do not change during the course of melt reaction. Since the spectrum between ½ $t_{0.5,rb}$ and $t_{0.5,rb}$ are equivalent, we compare only $t_{0.5,rb}$ and 5 $t_{0.5,rb}$. In general, all intensities related to absorption bands of crystalline phase decrease (indicated by arrow in Figure 4.55). This confirms quantitatively the aforementioned analysis. Major changes in intensities ($\Delta I \geq 0.5$ was set to be significantly difference from one to another) are found at wavenumbers 978, 1055, 1130, 1263, and 1275 cm^{-1}.

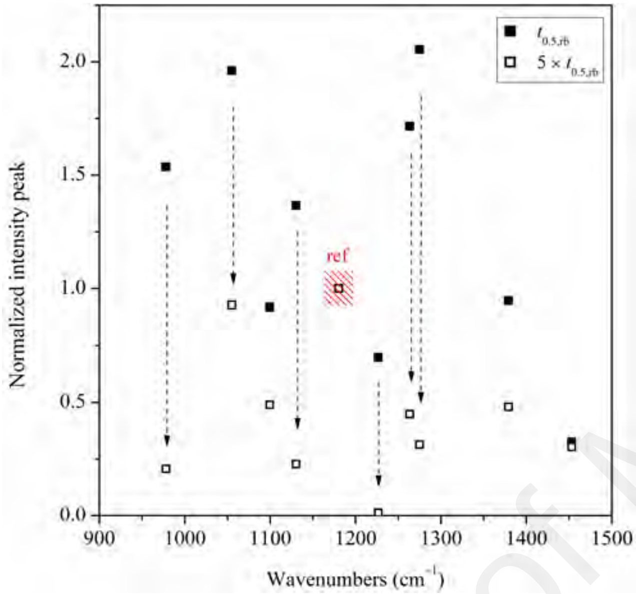

Figure 4.56 Normalized intensity peak of P(3HB-*co*-3HHx)-*blend*-ENR as a function of $t_{0.5,rb}$

CHAPTER V – CONCLUSIONS & RECOMMENDATIONS

Investigation on the thermal properties (isothermal crystallization and melt reaction), morphology and mechanical properties of P(3HB-*co*-3HHx) and its blend with ENR is reported in this study. Some of our research highlights are:

- From isothermal heat treatment, the molar mass of P(3HB-*co*-3HHx) reduces to a great extent (exponential decrease) with increasing temperature (temperature above its melting point). This is particularly useful for reaction with ENR.
- The constant rate of isothermal crystallization is slower in P(3HB-*co*-3HHx) containing higher 3HHx content. There are multiple melting peaks after isothermal crystallization of P(3HB-*co*-3HHx), which are due to the melting of primary crystallites formed during isothermal crystallization, followed by recrystallization and re-melting of the crystallites formed. This is confirmed by DSC (Avrami and Arrhenius-like relationship) and POM (spherulitic growth rate) analyses.
- Based on T_g and T_m^0 analyses, the blends of P(3HB-*co*-3HHx) and ENR are immiscible.
- With ENR present in the blends, the constant rate of isothermal crystallization increases. This means that ENR could act as a nucleating agent that promotes the crystallization of P(3HB-*co*-3HHx) during isothermal crystallization.
- For the study of melt reaction between P(3HB-*co*-3HHx) and ENR, the enthalpy of melt reaction exhibits a bell shape curve as a function of ENR mass fraction. The kinetics of melt reaction is similar to that of reported by other systems such as P(3HB)/ENR and P(3HB-*co*-3HV)/ENR.
- There is a formation of volatile compound(s) during melt reaction between P(3HB-*co*-3HHx) and ENR.

- Single T_g is detected after melt reaction, and the crystallization of P(3HB-*co*-3HHx) is inhibited.

Future research can be made possible on the study of viscoelastic properties before and after melt reaction. The morphology at the interface between P(3HB-*co*-3HHx) and ENR during melt reaction shall provide an interesting piece of information that aids our findings.

REFERENCES

Alenius, H., Turjanmaa, K., & Palosuo, T. (2002). Natural rubber latex allergy. *Occupational and Environment Medicine, 59*, 419-424.

Aoyagi, Y., Yamashita, K., & Doi, Y. (2002). Thermal degradation of poly[(*R*)-3-hydroxybutyrate], poly(*ε*-caprolactone), and poly[(*S*)-lactide]. *Polymer Degradation and Stability, 76*, 53-59.

Ariffin, H., Nishida, H., Shirai, Y., & Hassan, M. A. (2008). Determination of multiple thermal degradation mechanisms of poly(3-hydroxybutyrate). *Polymer Degradation and Stability, 93*, 1433-1439.

Asrar, J., Valentin, H. E., Berger, P. A., Tran, M., Padgetted, S. R., & Garbow, J. R. (2002). Biosynthesis and properties of poly(3-hydroxybutyrate-*co*-3-hydroxyhexanoate) polymers. *Biomacromolecules, 3*, 1006-1012.

Avérous, L., & Pollet, E. (2012). Biodegradable Polymers. In L. Avérous & E. Pollet (Eds.), *Environmental silicate nano-biocomposites, Series: Green energy and Technology* (pp. 13-39). London: Springer-Verlag.

Avrami, M. (1939). Kinetics of phase change. I General theory. *The Journal of Chemical Physics, 7*, 1103-1112.

Avrami, M. (1940). Kinetics of phase change. II transformation ‑ time relations for random distribution of nuclei. *The Journal of Chemical Physics, 8*, 212-224.

Avrami, M. (1941). Granulation, Phase Change, and Microstructure Kinetics of Phase Change. III *The Journal of Chemical Physics, 9*, 177-184.

Baker, C. S. L., Gelling, I. R., & Newell, R. (1985). Epoxidized natural rubber. *Rubber Chemistry and Technology, 58*, 67-85.

Barham, P. J., Keller, A., Otun, E. L., & Holmes, P. A. (1984). Crystallization and morphology of a bacterial thermoplastic: poly-3-hydroxybutyrate. *Journal of Materials Science, 19*, 2781-2794.

Bhubalan, K., Rathi, D. N., Abe, H., Iwata, T., & Sudesh, K. (2010). Improved synthesis of P(3HB-*co*-3HV-*co*-3HHx) terpolymers by mutant *Cupriavidus necator* using the PHA synthase gene of *Chromobacterium* sp. USM2 with high affinity towards 3HV. *Polymer Degradation and Stability, 95*, 1436-1442.

Bloembergen, S., Holden, D. A., Hamer, G. K., Bluhm, T. L., & Marchessault, R. H. (1986). Studies of composition and crystallinity of bacterial poly(*β*-hydroxybutyrate-*co*-*β*-hydroxyvalerate). *Macromolecules, 19*, 2865-2871.

Bluhm, T. L., Hamer, G. K., Marchessault, R. H., Fyfe, C. A., & Veregin, R. P. (1986). Isodimorphism in bacterial poly(*β*-hydroxybutyrate-*co*-*β*-hydroxyvalerate). *Macromolecules, 19*, 2871-2876.

Braunegg, G., Sonnleitner, B., & Lafferty, R. M. (1978). A rapid gas chromatographic method for the determination of poly-*β*-hydroxybutyric acid in microbial biomass. *European Journal of Applied Microbiology and Biotechnology, 6*, 29-37.

Briese, B. H., Jendrossek, D., & Schlegel, H. G. (1994). Degradation of poly(3-hydroxybutyrate-*co*-3-hydroxyvalerate) by aerobic sewage sludge. *FEMS Microbiology Letters, 117*, 107-111.

Buzarovska, A., Bogoeva-Gaceva, G., Grozdanov, A., Avella, M., Gentile, G., & Errico, M. (2007). Crystallization behavior of poly(hydroxybytyrate-*co*-valerate) in model and bulk PHBV/kenaf fiber composites. *Journal of Materials Science, 42*, 6501-6509.

Cai, H., & Qiu, Z. (2009). Effect of comonomer content on the crystallization kinetics and morphology of biodegradable poly(3-hydroxybutyrate-*co*-3-hydroxyhexanoate). *Physical Chemistry Chemical Physics, 11*, 9569-9577.

Calahorra, M. E., Cortazar, M., Eguiazabal, J. I., & Guzman, G. M. (1989). Thermogravimtric analysis of cellulose: Effect of the molecular weight on thermal decomposition. *Journal of Applied Polymer Science, 37*, 3305-3314.

Capaccio, G., Crompton, T. A., & Ward, I. M. (1976). The drawing behavior of linear polyethylene. I. Rate of drawing as a function of polymer molecular weight and initial thermal treatment. *Journal of Polymer Science: Polymer Physics Edition, 14*, 1641-1658.

Chan, C. H., Ismail, J., & Kammer, H. W. (2004). Melt reaction in blends of poly(3-hydroxybutyrate-*co*-3-hydroxyvalerate) and epoxidized natural rubber. *Polymer Degradation and Stability, 85*, 947-955.

Chan, C. H., & Kammer, H. W. (2009). Thermal properties of blends comprising poly(3-hydroxybutyrate-*co*-3-hydroxyvalerate) and epoxidized natural rubber. *Polymer Bulletin, 63*, 673-686.

Chan, C. H., Kammer, H. W., Sim, L. H., & Winie, T. (2011). Morphologies and kinetics of isothermal crystallization for green polymer blends comprising PHBV and ENR: Influence of rubbery phase. *International Journal of Pharmacy and Pharmaceutical Sciences, 3*, 1-6.

Chang, Y. W., Eom, J. P., Kim, J. G., Kim, H. T., & Kim, D. K. (2010). Preparation and characterization of shape memory polymer networks based on carboxylated telechelic poly(ε-caprolactone)/epoxidized natural rubber blends. *Journal of Industrial and Engineering Chemistry, 16*, 256-260.

Chee, M. J. K., Kummerlöwe, C., Lechner, M. D., & Kammer, H. W. (2004). Light scattering studies on ternary polymer blend solutions comprising poly(hydroxybutyrate). *Macromolecular Chemistry and Physics, 205*(8), 1108-1115.

Chen, C., Cheung, M. K., & Yu, P. H. F. (2005). Crystallization kinetics and melting behaviour of microbial poly(3-hydroxybutyrate-*co*-3-hydroxyhexanoate). *Polymer International, 54*, 1055-1064.

Cheng, M. L., Lin, C. C., Su, H. L., Chen, P. Y., & Sun, Y. M. (2008). Processing and characterization of electrospun poly(3-hydroxybutyrate-*co*-3-hydroxyhexanoate) nanofibrous membranes. *Polymer, 49*, 546-553.

Conti, D. S., Yoshida, M. I., Pezzin, S. H., & Coelho, L. A. F. (2007). Phase behavior of poly(3-hydroxybutyrate)/poly(3-hydroxybutyrate-*co*-3-hydroxyvalerate) blends. *Fluid Phase Equilibria, 261*, 79-84.

de Koning, G. J. M., & Lemstra, P. J. (1993). Crystallization phenomena in bacterial poly[(*R*)-3-hydroxybutyrate]: 2. Embrittlement and rejuvenation. *Polymer, 34*, 4089-4094.

Ding, C., Cheng, B., & Wu, Q. (2011). DSC analysis of isothermally melt-crystallized bacterial poly(3-hydroxybutyrate-*co*-3-hydroxyhexanoate) films. *Journal of Thermal Analysis and Calorimetry, 103*, 1001-1006.

Doi, Y., & Abe, C. (1990). Biosynthesis and characterization of a new bacterial copolyester of 3-hydroxyalkanoates and 3-hydroxy-.omega.-chloroalkanoates. *Macromolecules, 23*(15), 3705-3707.

Doi, Y., Kitamura, S., & Abe, H. (1995). Microbial synthesis and characterization of poly(3-hydroxybutyrate-*co*-3-hydroxyhexanoate). *Macromolecules, 28*, 4822-4828.

Doi, Y., Kunioka, M., Nakamura, Y., & Soga, K. (1986). Nuclear magnetic resonance studies on poly(β-hydroxybutyrate) and a copolyester of β-hydroxybutyrate and β-hydroxyvalerate isolated from *Alcaligenes eutrophus* H16. *Macromolecules, 19*, 169-173.

Doi, Y., Kunioka, M., Nakamura, Y., & Soga, K. (1988). Nuclear magnetic resonance studies on unusual bacterial copolyesters of 3-hydroxybutyrate and 4-hydroxybutyrate. *Macromolecules, 21*, 2722-2727.

Doi, Y., Tamaki, A., Kunioka, M., & Soga, K. (1988). Production of copolyesters of 3-hydroxybutyrate and 3-hydroxyvalerate by *Alcaligenes eutrophus* from butyric acid and pentanoic acid. *Applied Microbiology and Biotechnology, 28*, 330-334.

Dong, T., Mori, T., Aoyama, T., & Inoue, Y. (2010). Rapid crystallization of poly(3-hydroxybutyrate-*co*-3-hydroxyhexanoate) copolymer accelerated by cyclodextrin-complex as nucleating agent. *Carbohydrate Polymers, 80*, 387-393.

Feng, L., Watanabe, T., Wang, Y., Kichise, T., Fukuchi, T., Chen, G. Q., . . . Inoue, Y. (2008). Studies on comonomer compositional distribution of bacterial poly(3-hydroxybutyrate-*co*-3-hydroxyhexanoate)s and thermal characteristics of their factions. *Biomacromolecules, 3*, 1071-1077.

Fernández-Dacosta, C., Posada, J. A., Kleerebezem, R., Cuellar, M. C., & Ramirez, A. (2015). Microbial community-based polyhydroxyalkanoates (PHAs) production from wastewater: Techno-economic analysis and ex-ante environmental assessment. *Bioresource Technology, 185*, 368-377.

Fischer, J. J., Aoyagi, Y., Enoki, M., Doi, Y., & Iwata, T. (2004). Mechanical properties and enzymatic degradation of poly([*R*]-3-hydroxybutyrate-*co*-[*R*]-3-hydroxyhexanoate) uniaxially cold-drawn films. *Polymer Degradation and Stability, 83*, 453-460.

Fox, T. G., & Flory, P. J. (1950). Second ‐ order transition temperatures and related properties of polystyrene. I. Influence of molecular weight. *Journal of Applied Physics, 21*, 581.

Fukui, T., & Doi, Y. (1998). Efficient production of polyhydroxyalkanoates from plant oils by *Alcaligenes eutrophus* and its recombinant strain. *Applied Microbiology and Biotechnology, 49*, 333-336.

Furuhashi, Y., Imamura, Y., Jikihara, Y., & Yamane, H. (2004). Higher order structures and mechanical properties of bacterial homo poly(3-hydroxybutyrate) fibers prepared by cold-drawing and annealing processes. *Polymer, 45*, 5703-5712.

Galego, N., Rozsa, C., Sánchez, R., Fung, J., Vázquez, A., & Tomás, J. S. (2000). Characterization and application of poly(*β*-hydroxyalkanoates) family as composite biomaterials. *Polymer Testing, 19*, 485-492.

Gelling, I. R. (1991). Epoxidized natural rubber. *Journal of Natural Rubber Research, 6*, 184-205.

Gonda, K. E., Jendrossek, D., & Molitoris, H. P. (2000). Fungal degradation of the thermoplastic polymer poly-*β*-hydroxybutyric acid (PHB) under simulated deep sea pressure. *Hydrobiologia, 426*, 173-183.

Gunaratne, L. M. W. K., & Shanks, R. A. (2005). Multiple melting behaviour of poly(3-hydroxybutyrate-*co*-hydroxyvalerate) using step-scan DSC. *European Polymer Journal, 41*, 2980-2988.

Gunaratne, L. M. W. K., Shanks, R. A., & Amarasinghe, G. (2004). Thermal history effects on crystallisation and melting of poly(3-hydroxybutyrate). *Thermochimica Acta, 423*, 127-135.

Hablot, E., Bordes, P., Pollet, E., & Averous, L. (2007). Thermal and thermo-mechanical degradation of poly(3-hydroxybutyrate)-based multiphase system. *Polymer Degradation and Stability, 93*, 413-421.

Hallensleben, M. L., Schmidt, H. R., & Schuster, R. H. (1995). Epoxidation of poly(*cis*-1,4-isoprene) microgels. *Die Angewandte Makromolekulare Chemie, 227*, 87-99.

Hay, I. D., Du, J., Burr, N., & Rehm, B. H. A. (2015). Bioengineering of bacteria to assemble custom-made polyester affinity resins. *Applied and Environmental Microbiology, 81*, 282-291.

Hay, J. N., & Mills, P. J. (1982). The use of differential scanning calorimetry to study polymer crystallization kinetics. *Polymer, 23*, 1380-1384.

Hoffman, J. D. (1982). Role of reptation in the rate of crystallization of polyethylene fractions from the melt. *Polymer, 23*, 656-670.

Hoffman, J. D., Davis, G. T., & Lauritzen, J. I. (1976). The rate of crystallization of linear polymers with chain folding. In N. B. Hannay (Ed.), *Treastise on Solid State Chemistry* (Vol. 3-Crystalline and Noncrystalline Solids, pp. 497). New York: Plenum Press.

Hoffman, J. D., & Weeks, J. J. (1962). Melting process and the equilibrim melting temperature of polychlorotrifluoroethylene. *Journal of Research of the National Bureau of Standards-A. Physics and Chemistry, 66A*, 13-28.

Hu, Y., Zhang, J., Sato, H., Noda, I., & Ozaki, Y. (2007). Multiple melting behavior of poly(3-hydroxybutyrate-*co*-3-hydroxyhexanoate) investigated by differential scanning calorimetry and infrared spectroscopy. *Polymer, 48*, 4777-4786.

Ishak, Z. A. M., & Bakar, A. A. (1995). An investigation on the potential of rice husk ash as fillers for epoxidized natural rubber (ENR). *European Polymer Journal, 31*, 259-269.

Iwata, T., Fujita, M., Aoyagi, Y., Doi, Y., & Fujisawa, T. (2005). Time-resolved *X*-ray diffraction study on poly[(*R*)-3-hydroxybutyrate] films during two-step-drawing: Generation mechanism of planar zigzag structure. *Biomacromolecules, 6*, 1803-1809.

Jellinek, H. H. G. (1955). *Degradation of vinyl polymers*. New York: Academic Press.

Jendrossek, D., & Handrick, R. (2002). Microbial degradation of polyhydroxyalkanoates. *Annual Review of Microbiology, 56*, 403-432.

Jendrossek, D., Schirmer, A., & Schlegel, H. G. (1996). Biodegradation of polyhydroxyalkanoic acids. *Applied Microbiology and Biotechnology, 46*, 451-463.

Kai, W., He, Y., & Inoue, Y. (2005). Fast crystallization of poly(3-hydroxybutyrate) and poly(3-hydroxybutyrate-*co*-3-hydroxyvalerate) with talc and boron nitride as nucleating agents. *Polymer International, 54*, 780-789.

Kopinke, F. D., Remmler, M., & Mackenzie, K. (1996). Thermal decomposition of biodegradable polyesters—I. Poly(β-hydroxybutyric acid). *Polymer Degradation and Stability, 52*, 25-38.

Korson, L., Drost-Hansen, W., & Millero, F. J. (1969). Viscosity of water at various temperatures. *Journal of Physical Chemistry, 73*(1), 34-39.

Kunasundari, B., & Sudesh, K. (2011). Isolation and recovery of microbial polyhydroxyalkanoates. *eXPRESS Polymer Letters, 5*, 620-634.

Kunioka, M., Tamaki, A., & Doi, Y. (1989). Crystalline and thermal properties of bacterial copolyesters: poly(3-hydroxybutyrate-*co*-3-hydroxyvalerate) and poly(3-hydroxybutyrate-*co*-4-hydroxybutyrate). *Macromolecules, 22*, 694-497.

Kusaka, S., Iwata, T., & Doi, Y. (1999). Properties and biodegradability of ultra-high-molecular-weight poly[(*R*)-3-hydroxybutyrate] produced by a recombinant *Escherichia coli*. *International Journal of Biological Macromolecules, 25*, 87-94.

Lauritzen, J. I., & Hoffman, J. D. (1973). Extension of theory of growth of chain‐folded polymer crystals to large undercoolings. *Journal of Applied Physics, 44*, 4340-4352.

Lee, H. K. (2008). *Study of poly(3-hydroxybutyrate)/epoxidized natural rubber blends. Melt reaction and thermal properties.* (Doctor of Philosophy), Universiti Sains Malaysia, Malaysia.

Lee, H. K., Ismail, J., Kammer, H. W., & Baker, M. A. (2005). Melt reaction in blends of poly(3-hydroxybutyrate) (PHB) and epoxidized natural rubber (ENR-50). *Journal of Applied Polymer Science, 95*, 113-129.

Lee, M. Y., Lee, T. S., & Park, W. H. (2001). Effect of side chains on the thermal degradation of poly(3-hydroxyalkanoates). *Macromolecular Chemistry and Physics, 202*, 1257-1261.

Lee, W. H., Loo, C. Y., Nomura, C. T., & Sudesh, K. (2008). Biosynthesis of polyhydroxyalkanoate copolymers from mixtures of plant oils and 3-hydroxyvalerate precursors. *Bioresource Technology, 99*, 6844-6851.

Lemoigne, M. (1925). Etudes sur l'autolyse microbie acidification par formation d'acide β-oxybutyrique. *Annales de l'Institut Pasteur, 39*, 144.

Lemoigne, M. (1926). Produit de déshydratation et de polymérisation de l'acide β-oxybutyrique. *Bull Soc Chim Biol, 8*, 770-782.

Li, S. D., He, J. D., Yu, P. H., & Cheung, M. K. (2003). Thermal degradation of poly(3-hydroxybutyrate) and poly(3-hydroxybutyrate-*co*-3-hydroxyvalerate) as studied by TG, TG-FTIR, and Py-GC/MS. *Journal of Applied Polymer Science, 89*, 1530-1536.

Li, S. D., Yu, P. H., & Cheung, M. K. (2001). Thermogravimetric analysis of poly(3-hydroxybutyrate) and poly(3-hydroxybutyrate-*co*-3-hydroxyvalerate). *Journal of Applied Polymer Science, 80*, 2237-2244.

Loo, C. Y., Lee, W. H., Tsuge, T., Doi, Y., & Sudesh, K. (2005). Biosynthesis and characterization of poly(3-hydroxybutyrate-*co*-3-hydroxyhexanoate) from palm oil products in a *Wautersia eutropha* mutant. *Biotechnology Letters, 27*, 1405-1410.

Lorenzo, A. T., Arnal, M. L., Albuerne, J., & Müller, A. J. (2007). DSC isothermal polymer crystallization kinetics measurements and the use of the Avrami equation to fit the data: Guidelines to avoid common problems. *Polymer Testing, 26*, 222-231.

Lu, X., Wen, X., & Yang, D. (2011). Isothermal crystallization kinetics and morphology of biodegradable poly(3-hydroxybutyrate-*co*-4-hydroxybutyrate). *Journal of Materials Science, 46*, 1281-1288.

Malaysia, L. G. (2014). Natural Rubber Statistics. from Lembaga Getah Malaysia

Mandelkern, L. (2002). *Crystallization of Polymers* (Second ed. Vol. 1-Equilibrium Concepts). United Kingdom: Cambridge University Press.

Mandelkern, L. (2004). *Crystallization of Polymers* (Vol. 2 - Kinetics and Mechanisms). Cambridge: Cambridge University Press.

Martinez-Salazar, J., Sanchez-Cuesta, M., Barham, P. J., & Keller, A. (1989). Thermal expansion and spherulite cracking in 3-hydroxybutyrate/3-hydroxyvalerate copolymers. *Journal of Materials Science Letters, 8*, 490-492.

Mergaert, J., Webb, A., Anderson, C., Wouters, A., & Swings, J. (1993). Microbial degradation of poly(3-hydroxybutyrate) and poly(3-hydroxybutyrate-*co*-3-hydroxyvalerate) in soils. *Applied and Environmental Microbiology, 59*, 3233-3238.

Mitomo, H., Hsieh, W. C., Nishiwaki, K., Kasuya, K., & Doi, Y. (2001). Poly(3-hydroxybutyrate-*co*-4-hydroxybutyrate) produced by *Comamonas acidovorans*. *Polymer, 42*, 3455-3461.

Mitomo, H., Morishita, N., & Doi, Y. (1995). Structural changes of poly(3-hydroxybutyrate-*co*-3-hydroxyvalerate) fractionated with acetone-water solution. *Polymer, 36*, 2573-2578.

Mitomo, H., Takahashi, T., Ito, H., & Saito, T. (1999). Biosynthesis and characterization of poly(3-hydroxybutyrate-*co*-3-hydroxyvalerate) produced by *Burkholderia cepacia* D1. *International Journal of Biological Macromolecules, 24*, 311-318.

Mohanty, S., Mukunda, P. G., & Nando, G. B. (1995). Thermal analysis of blends of poly(ethylene *co*-acrylic acid) (PEA) and epoxidised natural rubber (ENR). *Polymer Degradation and Stability, 50*, 21-28.

Mohanty, S., & Nando, G. B. (1996). Mechanical and dynamic mechanical properties of miscible blends of epoxidized natural rubber and poly(ethylene-*co*-acrylic acid). *Polymer, 37*, 5387-5394.

Mohanty, S., Roy, S., Santra, R. N., & Nando, G. B. (1995). Miscibility of blends of epoxidized natural rubber and poly(ethylene-*co*-acrylic acid). *Journal of Applied Polymer Science, 58*, 1947-1957.

Nakamura, S., Doi, Y., & Scandola, M. (1992). Microbial synthesis and characterization of poly(3-hydroxybutyrate-*co*-4-hydroxybutyrate). *Macromolecules, 25*, 4237-4241.

Nakason, C., Kaesaman, A., Wongkul, T., & Kiatkamjornwong, S. (2001). Rheological and curing properties of reactive blending products of epoxidised natural rubber and cassava starch. *Plastic, Rubber and Composites, 30*, 154-161.

Nakason, C., Tobprakhon, A., & Kaesaman, A. (2005). Thermoplastic vulcanizates based on poly(methyl methacrylate)/epoxidized natural rubber blends: Mechanical, thermal, and morphological properties. *Journal of Applied Polymer Science, 98*, 1251-1261.

Narathichat, M., Kummerlöwe, C., Vennemann, N., Sahakaro, K., & Nakason, C. (2012). Influence of epoxide level and reactive blending on properties of epoxidized natural rubber and nylon-12 blends. *Advances in Polymer Technology, 31*, 118-129.

Natta, G., & Corradini, P. (1960). Structure and properties of isotactic polypropylene. *Il Nuovo Cimento Series 10, 15*, 40-51.

Nishi, T., & Wang, T. T. (1975). Melting point depression dan kinetics effects of cooling on crystallization in poly(vinylidene fluride)-poly(methyl methacrylate) mixtures. *Macromolecules, 8*, 990-915.

Oh, Y. H., Lee, S. H., Jang, Y. A., Choi, J. W., Hong, K. S., Yu, J. H., . . . Park, S. J. (2015). Development of rice bran treatment process and its use for the synthesis of polyhydroxyalkanoates from rice bran hydrolysate solution. *Bioresource Technology, 181*, 283-290.

Orts, W. J., Marchessault, R. H., Bluhm, T. L., & Hamer, G. K. (1990). Observation of strain-induced *β* form in poly(*β*-hydroxyalkanoates). *Macromolecules, 23*, 5368-5370.

Padermshoke, A., Katsumoto, Y., Sato, H., Ekgasit, S., Noda, I., & Ozaki, Y. (2004). Surface melting and crystallization behavior of polyhydroxyalkanoates studied by attenuated total reflection infrared spectroscopy. *Polymer, 45*, 6547-6554.

Pan, P., Liang, Z., Nakamura, N., Miyagawa, T., & Inoue, Y. (2009). Uracil as nucleating agent for bacterial poly[(3-hydroxybutyrate)-*co*-(3-hydroxyhexanoate)] copolymers. *Macromolecular Bioscience, 9*, 585-595.

Praphulla. (2012). *Studies on reactive blends of poly(hydroxybutyrate-co-valerate) and poly(butylene succinate) bioplastics.* (Master of Applied Science), The University of Guelph, Ontario, Canada.

Qu, X. H., Wu, Q., & Chen, G. Q. (2006). In vitro study on hemocompatibility and cytocompatibility of poly(3-hydroxybutyrate-*co*-3-hydroxyhexanoate). *Journal of Biomaterials Science, Polymer Edition, 17*, 1107-1121.

Rooj, S., Thakur, V., Gohs, U., Wagenknecht, U., Bhowmick, A. K., & Heinrich, G. (2011). *In situ* reactive compatibilization of polypropylene/epodixized natural rubber blends by electron induced reactive processing: novel in-line mixing tehnology. *Polymers for Advanced Technologies, 22*, 2257-2263.

Salim, Y. S., Chan, C. H., Sudesh, K., & Gan, S. N. (2014). Isothermal crystallisation kinetics of microbial poly(3-hydroxybutyrate-*co*-3-hydroxyhexanoate). *International Journal of Pharmacy and Pharmaceutical Sciences, 6*, 3-8.

Salim, Y. S., Sharon, A., Vigneswari, S., Mohamad Ibrahim, M. N., & Amirul, A. A. (2012). Environmental degradation of microbial polyhydroxyalkanoates and oil palm-based composites. *Applied Biochemistry and Biotechnology, 167*, 314-326.

Sang, B.-I., Hori, K., Tanji, Y., & Unno, H. (2002). Fungal contribution to in situ biodegradation of poly(3-hydroxybutyrate-*co*-3-hydroxyvalerate) film in soil. *Applied Microbiology and Biotechnology, 58*, 241-247.

Sato, H., Murakami, R., Zhang, J., Ozaki, Y., Mori, K., Takahashi, I., . . . Noda, I. (2006). *X*-ray diffraction and infrared spectroscopy studies on crystal and lamellar structure and cho hydrogen bonding of biodegradable poly(hydroxyalkanoate). *Macromolecular Research, 14*, 408-415.

Sato, H., Nakamura, M., Padermshoke, A., Yamaguchi, H., Terauchi, H., Ekgasit, S., . . . Ozaki, Y. (2004). Thermal behavior and molecular interaction of poly(3-hydroxybutyrate-*co*-3-hydroxyhexanoate) studied by wide-angle X-ray diffraction. *Macromolecules, 37*, 3763-3769.

Sato, S., Maruyama, H., Fujiki, T., & Matsumoto, K. (2015). Regulation of 3-hydroxyhexanoate composition in PHBH synthesized by recombinant

Cupriavidus necator H16 from plant oil by using butyrate as a co-substrate. *Journal of Bioscience and Bioengineering, In Press*.

Sheavly, S. B., & Register, K. M. (2007). Marine debris & plastics: Environmental concerns, sources, impacts and solutions. *Journal of Polymers and the Environment, 15*, 301-305.

Shimamura, E., Kasuya, K., Kobayashi, G., Shiotani, T., Shima, Y., & Doi, Y. (1994). Physical properties and biodegradability of microbial poly(3-hydroxybutyrate-*co*-3-hydroxyhexanoate). *Macromolecules, 27*, 878-880.

Sridewi, N., Bhubalan, K., & Sudesh, K. (2006). Degradation of commercially important polyhydroxyalkanoates in tropical mangrove ecosystem. *Polymer Degradation and Stability, 91*, 2931-2940.

Steinbüchel, A., & Valentin, H. (1995). Diversity of bacterial polyhydroxyalkanoic acids. *FEMS Microbiology Letters, 128*(3), 219-228.

Sun, J., Dai, Z., Zhao, Y., & Chen, G. Q. (2007). *In vitro* effect of oligo-hydroxyalkanoates on the growth of mouse fibroblast cell line L929. *Biomaterials, 28*, 3896-3903.

Tanaka, T., Fujita, M., Takeuchi, A., Suzuki, Y., Uesugi, K., Ito, K., . . . Iwata, T. (2006). Formation of highly ordered structure in poly[(*R*)-3-hydroxybutyrate-*co*-(*R*)-3-hydroxyvalerate] high-strength fibers. *Macromolecules, 39*, 2940-2946.

Tsuge, T., Saito, Y., Kikkawa, Y., Hiraishi, T., & Doi, Y. (2004). Biosynthesis and compositional regulation ofpoly[(3-hydroxybutyrate)-*co*-(3-hydroxyhexanoate)] in recombinant *Ralstonia eutropha* expressing mutated polyhydroxyalkanoate synthase genes. *Macromolecular Bioscience, 4*, 238-242.

Van Zyl, A. J. P., Graef, S. M., Sanderson, R. D., Klumperman, B., & Pasch, H. (2003). Monitoring the grafting of epoxidized natural rubber by size-exclusion chromatography coupled to FTIR spectroscopy. *Journal of Applied Polymer Science, 88*, 2539-2549.

Viswanath, D. S., Ghosh, T. K., Prasad, D. H., Dutt, N. V., & Rani, K. Y. (2007). *Viscosity of liquids (Theory, estimation, experiment, and data)*. The Netherlands: Springer.

Vo, M. T., Ko, K., & Ramsay, B. (2015). Carbon-limited fed-batch production of medium-chain-length polyhydroxyalkanoates by a *phaZ*-knockout strain of *Pseudomonas putida* KT2440. *Journal of Industrial Microbiology & Biotechnology, 42*, 637-646.

Wang, L., Wang, X., Zhu, W., Chen, Z., Pan, J., & Xu, K. (2010). Effect of nucleation agents on the crystallization of poly(3-hydroxybutyrate-*co*-4-hydroxybutyrate) (P3/4HB). *Journal of Applied Polymer Science, 116*, 1116-1123.

Watanabe, T., He, Y., Fukuchi, T., & Inoue, Y. (2001). Comonomer compositional distribution and thermal characteristics of bacterially synthesized poly(3-hydroxybutyrate-*co*-3-hydroxyhexanoate)s. *Macromolecular Bioscience, 1*, 75-83.

Wen, X., Lu, X., Peng, Q., Zhu, F., & Zheng, N. (2012). Crystallization behaviors and morphology of biodegradable poly(3-hydroxybutyrate-*co*-4-hydroxybutyrate). *Journal of Thermal Analysis and Calorimetry, 109*, 959-966.

Weng, M., & Qiu, Z. (2014). Effect of cyanuric acid on the crystallization kinetics and morphology of biodegradable poly(l-lactide) as an efficient nucleating agent. *Thermochimica Acta, 577*, 41-45.

Wondraczek, K., Adams, J., & Fuhrmann, J. (2004). Effect of thermal degradation on glass transition temperature of PMMA. *Macromolecular Chemistry and Physics, 205*, 1858-1862.

Xu, J., Guo, B. H., Yang, R., Wu, Q., Chen, G. Q., & Zhang, Z. M. (2002). In situ FTIR study on melting and crystallization of polyhydroxyalkanoates. *Polymer, 43*, 6893-6899.

Xu, J., Guo, B. H., Zhang, Z. M., Zhou, J. J., Jiang, Y., Yan, S., . . . Schultz, J. M. (2004). Direct AFM observation of crystal twisting and organization in banded spherulites of chiral poly(3-hydroxybutyrate-*co*-3-hydroxyhexanoate). *Macromolecules, 37*, 4118-4123.

Yamada, S., Wang, Y., Asakawa, N., Yoshie, N., & Inoue, Y. (2001). Crystalline structural change of bacterial poly(3-hydroxybutyrate-*co*-3-hydroxyvalerate) with narrow compositional distribution. *Macromolecules, 34*, 4659-4661.

Ye, H. M., Wang, Z., Wang, H. H., Chen, G. Q., & Xu, J. (2010). Different thermal behaviors of microbial polyesters poly(3-hydroxybutyrate-*co*-3-hydroxyvalerate-*co*-3-hydroxyhexanoate) and poly(3-hydroxybutyrate-*co*-3-hydroxyhexanoate). *Polymer, 51*, 6037-6046.

Yokoo, T., Matsumoto, K., Ooba, T., Morimoto, K., & Taguchi, S. (2015). Enhanced poly(3-hydroxybutyrate) production in transgenic tobacco BY-2 cells using engineered acetoacetyl-CoA reductase. *Bioscience, Biotechnology, and Biochemistry, ahead-of-print*, 1-3.

Yokouchi, M., Chatani, Y., Tadokoro, H., Teranishi, K., & Tani, H. (1973). Structural studies of polyesters: 5. Molecular and crystal structures of optically active and racemic poly (*β*-hydroxybutyrate). *Polymer, 14*, 267-272.

You, M., Peng, G., Li, J., Ma, P., Wang, Z., Shu, W., . . . Chen, G. Q. (2011). Chondrogenic differentiation of human bone marrow mesenchymal stem cells on polyhydroxyalkanoate (PHA) scaffolds coated with PHA granule binding protein PhaP fused with RGD peptide. *Biomaterials, 32*, 2305-2313.

Yu, F., Nakayama, T., Nakamura, N., Katsumata, K., Pan, P., & Inoue, Y. (2009). Miscibility and physical properties of poly(3-hydroxybutyrate-*co*-3-hydroxyhexanoate)/poly(ethylene oxide) binary blends. *Macromolecular Materials and Engineering, 294*, 868-876.

Zhao, Y., Zou, B., Shi, Z., Wu, Q., & Chen, G. Q. (2007). The effect of 3-hydroxybutyrate on the *in vitro* differentiation of murine osteoblast MC3T3-E1 and *in vivo* bone formation in ovariectomized rats. *Biomaterials, 28*, 3063-3073.

Zhou, J., Peng, S. W., Wang, Y. Y., Zheng, S. B., Wang, Y., & Chen, G. Q. (2010). The use of poly(3-hydroxybutyrate-*co*-3-hydroxyhexanoate) scaffolds for tarsal repair in eyelid reconstruction in the rat. *Biomaterials, 31*, 7512-7518.

Zini, E., Focarete, M. L., Noda, I., & Scandola, M. (2007). Bio-composite of bacterial poly(3-hydroxybutyrate-*co*-3-hydroxyhexanoate) reinforced with vegetable fibers. *Composites Science and Technology, 67*, 2085-2094.

LIST OF PUBLICATIONS AND PAPERS PRESENTED

Publications

1. Salim Y. S., Chan C. H., Kammer H. W., Sudesh K., & Gan S. N. (2015). Polymer blends made of poly(3-hydroxybutyrate-*co*-3-hydroxyhexanoate) and epoxidized natural rubber: Thermal and mechanical response. *AIP Conference Proceedings*, 1674, 020033.
2. Salim Y. S., Chan C. H., Sudesh K., & Gan S. N. (2014). Isothermal crystallisation kinetics of microbial poly(3-hydroxybutyrate-*co*-3-hydroxyhexanoate). *International Journal of Pharmacy and Pharmaceutical Sciences*, 6, Suppl 3, 3-8.
3. Salim Y. S., Chan C. H., Sudesh K., & Gan S. N. (2014). Chapter 16. Thermal properties of poly(hydroxyalkanoates). In: Physical Chemistry of Macromolecules: Macro to Nanoscales. Chan C. H., Chia C. H., & Thomas S. (Eds), *Apple Academic Press Inc.*, Canada, p.441-473.
4. Salim Y. S., Chan C. H., Sudesh K., & Gan S. N. (2013). Influence of thermal treatment on the molecular weights of polyhydroxyalkanoates containing 3-hydroxyhexanoate. *Advanced Materials Research*, 812, 250-253.

Papers presented

1. Salim, Y. S., Sudesh, K., Gan S. N., & Chan, C. H. (2016). Miscibility and isothermal crystallization of poly(3-hydroxybutyrate-*co*-3-hydroxyhexanoate)/epoxidized natural rubber blends. *International Symposium on Advanced Polymeric Materials*, 16 – 18 May 2016, Putra World Trade Centre, Kuala Lumpur, Malaysia.
2. Salim, Y. S., Sudesh, K., Gan S. N., Chan, C. H., & Saiter, J. M. (2015). Thermal degradation in the melt reaction between poly(3-hydroxybutyrate-*co*-3-hydroxyhexanoate) and epoxidized natural rubber. *23rd World Forum on Advanced Materials*, 11 – 15 May 2015, Lincoln, Nebraska, United States of America.
3. Salim, Y. S., Chan, C. H., Kammer, H. W., Sudesh, K., & Gan S. N. (2014). Thermal properties and morphologies of poly(3-hydroxybutyrate-*co*-3-hydroxyhexanoate)-*blend*-epoxidized natural rubber. *The IUPAC World Polymer Congress MACRO 2014*, 6 – 11 July 2014, Chiang Mai, Thailand.
4. Salim, Y. S., Chan, C. H., Sudesh, K., & Gan S. N. (2014). Influence of rubbery phase to kinetics of isothermal crystallisation of poly(3-hydroxybutyrate-*co*-3-hydroxyhexanoate). *International Symposium on Advanced Polymeric Materials*, 13 – 16 May 2014, Putra World Trade Centre, Kuala Lumpur, Malaysia.
5. Chan, C. H., Soon, T. K., Salim, Y. S., Kammer, H. W., Sudesh, K., & Gan, S. N. (2014). Influence of thermal treatment on poly(hydroxyalkanoates) and the reactive blends of poly(hydroxyalkanoates) and epoxidized natural rubber. *World Forum on Advanced Materials*, 7 – 11 April 2014, STIAS Research Centre, Stellenbosch, South Africa.

6. Chan, C. H., Kammer, H. W., Salim, Y. S., Gan, S. N., & Sudesh, K. (2013). Thermal properties of poly(hydroxyalkanoates)s and epoxidized natural rubber. *3rd FAPS Polymer Congress and MACRO 2013*, 15 – 18 May 2013, JN Tata Auditorium, Indian Institute of Science, Bangalore, India.
7. Salim, Y. S., Chan, C. H., Sudesh, K., & Gan S. N. (2012). Kinetics crystallisation of microbial poly(3-hydroxybutyrate-*co*-3 mol% 3-hydroxyhexanoate) under isothermal condition. *Seminar Hasil Penyelidikan, Kementerian Pengajian Tinggi bil.2/2012*, 8 – 9 November 2012, Bandar Enstek, Malaysia.
8. Salim, Y. S., Chan, C. H., Sudesh, K., & Gan S. N. (2012). Kinetics crystallisation of microbial polyhydroxyalkanoates containing different molar fractions of 3-hydroxyhexanoates under isothermal condition. *Cambodia Malaysian Chemical Conference*, 19 – 21 October 2012, Siem Reap, Cambodia.
9. Salim, Y. S., Chan, C. H., Sudesh, K., & Gan S. N. (2012). Effect of isothermal heat treatment on the chain scission of microbial poly(3-hydroxybutyrate-*co*-3-hydroxyhexanoate). *International Symposium on Advanced Polymeric Materials*, 10 – 11 July 2012, Sunway Resort Hotel and Spa, Selangor, Malaysia.